Fall 2014

Predicting lubrication performance between the slipper and swashplate in axial piston hydraulic machines

Andrew T. Schenk
Purdue University

Graduate School Form 30
(Revised 08/14)

PURDUE UNIVERSITY
GRADUATE SCHOOL
Thesis/Dissertation Acceptance

This is to certify that the thesis/dissertation prepared

By Andrew T. Schenk

Entitled
PREDICTING LUBRICATION PERFORMANCE BETWEEN THE SLIPPER AND SWASHPLATE IN AXIAL PISTON HYDRAULIC MACHINES

For the degree of Doctor of Philosophy

Is approved by the final examining committee:

Dr. Monika Ivantysynova

Dr. John Lumkes

Dr. Farshid Sadeghi

Dr. Andrea Vacca

To the best of my knowledge and as understood by the student in the Thesis/Dissertation Agreement, Publication Delay, and Certification/Disclaimer (Graduate School Form 32), this thesis/dissertation adheres to the provisions of Purdue University's "Policy on Integrity in Research" and the use of copyrighted material.

Dr. Monika Ivantysynova

Approved by Major Professor(s): _____

_____

Approved by: Dr. Ganesh Subbarayan 12/02/2014

Head of the Department Graduate Program Date

PREDICTING LUBRICATION PERFORMANCE BETWEEN THE SLIPPER AND SWASHPLATE IN AXIAL PISTON HYDRAULIC MACHINES

A Dissertation

Submitted to the Faculty

of

Purdue University

by

Andrew Schenk

In Partial Fulfillment of the

Requirements for the Degree

of

Doctor of Philosophy

December 2014

Purdue University

West Lafayette, Indiana

To my family and especially my wife, Désirée.

ACKNOWLEDGEMENTS

I must first thank Dr. Monika Ivantysynova for offering me the ability to conduct my doctoral research at the Maha Fluid Power Research Center. In this special opportunity, I was able to learn and develop an advanced numerical model, which was my driving ambition to pursue graduate research. Her advisement, mentorship, and generosity made this endeavor an incredible experience for which I am ever grateful. I must also thank Dr. Andrea Vacca, Dr. John Lumkes, and Dr. Farshid Sadeghi for their efforts in serving on my committee and for the advice and assistance they provided.

Thank you to all of my fellow lab mates and colleagues throughout my graduate education. I am especially thankful to Matteo and Marco for their collaboration and teaching and to Natalie for dedicating her research to the design and development of a slipper test rig. Thanks to the entire Maha team over the past five years who have helped my work and made this such an enjoyable and fun experience! Thank you Susan for being the caring and ever helpful individual you are, and Anthony for the wisdom and expertise you offer in the lab.

I must thank my family for encouraging me to seize this opportunity and providing the support they always have. Finally, thanks to my wife, Désirée, for embarking on this exciting adventure with me and for all of her love.

TABLE OF CONTENTS

Page

Page

Page

LIST OF TABLES

LIST OF FIGURES

Figure Page

Figure Page

Figure Page

Figure Page

LIST OF SYMBOLS

A	Area	$[m^2]$
a	Scalar coefficient	[-]
$\mathbf{A}$	Coefficient matrix	[-]
a_K	Piston acceleration	$[m/s^2]$
B	Balance factor	[-]
$\mathbf{b}$	Coefficient vector	[-]
$\mathbf{B}$	Strain-displacement matrix	[-]
c_p	Heat capacitance	$[J/kg{\cdot}K]$
$\mathbf{D}$	Constitutive matrix	[-]
d_{dG}	Slipper orifice diameter	$[m]$
d_{inG}	Inner pocket diameter	$[m]$
d_K	Piston diameter	$[m]$
d_{outG}	Outer pocket diameter	$[m]$
E	Elastic modulus	$[Pa]$
$\mathbf{f}$	Body force	$[N]$
F_{DK}	Displacement chamber pressure force	$[N]$
F_{fz}	Slipper fluid force	$[N]$
F_{HD}	Slipper hold down force	$[N]$

F_{SK}	Piston ball joint force	$[N]$
F_{TG}	Slipper viscous friction force	$[N]$
$F_{\omega G}$	Centrifugal force	$[N]$
g_1, g_2, g_3	Slipper control points	[-]
h	Fluid film thickness	$[m]$
h	Basis function	[-]
h_K	Piston stroke	$[m]$
I	Area moment of inertia	$[m^4]$
K	Fluid bulk modulus	$[Pa]$
K	Stiffness matrix	[-]
L_1, L_2, L_3, L_4	Natural or Barycentric coordinates	[-]
l_G	Distance between slipper socket center and gap	$[m]$
l_{SG}	Distance between slipper socket center and COG	$[m]$
m	Mass vector	$[kg]$
m_G	Slipper mass	$[kg]$
m_K	Piston / slipper assembly mass	$[kg]$
$M_{\omega G}$	Centrifugal moment	$[Nm]$
n	Normal vector	[-]
p	Fluid pressure	$[Pa]$
P	Power loss	$[W]$
p_{DC}	Displacement chamber pressure	$[Pa]$
p_G	Slipper pocket pressure	$[Pa]$
Q	Flow	$[m^3/s]$

q	Heat flux	$[W/m^2]$
Q_{SG}	Slipper leakage	$[m^3/s]$
r, θ, z_G	Slipper local cylindrical coordinate system	[-]
R_b	Cylinder block radius	$[m]$
r_G	Slipper ellipsoid radius	$[m]$
r_{inG}	Inner pocket radius	$[m]$
r_{outG}	Outer pocket radius	$[m]$
s_K	Piston displacement	$[m]$
$speed_K$	Piston relative rotational speed	[-]
t	Time	$[s]$
T	Temperature	[°C]
u	Deformation	$[m]$
$\mathbf{v}$	Fluid velocity	$[m/s]$
V	Volume	$[m^3]$
v_{xG}, v_{yG}	Slipper velocity	$[m/s]$
x_G, y_G, z_G	Slipper local Cartesian coordinate system	[-]
x_S, y_S, z_S	Swashplate global coordinate system	[-]
α	Orifice coefficient	[-]
α_T	Coefficient of linear thermal expansion	$[m/m°C]$
β	Swashplate angle	$[deg]$
$\boldsymbol{\varepsilon}$	Strain tensor	$[m/m]$
η	Convection coefficient	$[W/m^2 \cdot K]$
λ	Thermal conductivity	$[W/m \cdot K]$

μ	Dynamic fluid viscosity	[$Pa{\cdot}s$]
v	Poisson ratio	[-]
ρ	Density	[kg/m^3]
$\boldsymbol{\sigma}$	Stress tensor	[Pa]
τ	Shear stress	[Pa]
φ	Pump shaft angle	[deg]
Φ	Viscous heat generation	[W/m^3]
ϕ	Scalar quantity	[-]
ω	Shaft speed	[rad/s]

SUBSCRIPTS

b	Bottom
b	Bottom
e	East
G	Slipper
K	Piston
n	North
s	South
t	Top
w	West
Δt	Timestep

ABSTRACT

Schenk, Andrew Ph.D., Purdue University, December 2014. Predicting Lubrication Performance between the Slipper and Swashplate in Axial Piston Hydraulic Machines. Major Professor: Dr. Monika Ivantysynova, School of Mechanical Engineering.

Engineering of the sliding interfaces within swashplate type axial piston machines represents the most complex and difficult part of the design process. The sliding interfaces are subject to significant normal loads which must be supported while simultaneously preventing component wear to ensure long lasting operation. Proper lubrication design is essential to separate the solid bodies from each other, but the complexity of the physics involved makes this a difficult problem. This work focuses on lubrication and the resulting energy losses at the sliding interface between the slipper and swashplate.

To better understand the slipper lubrication performance, a numerical model has been developed to predict the behavior of a design. The numerical model considers the multi-physics, multi-scale, and transient nature of the lubrication problem by utilizing novel segmented physics solvers and numerical techniques. Partitioned solvers considering the fluid pressure and temperature distributions, structural deformation due to fluid pressure and viscous heating, as well as a solid body dynamics from transient loads have been originally developed and tightly coupled. Although the effort necessary to implement this

was significant, by avoiding a more traditional co-simulation approach, high computational efficiency and model fidelity can be achieved.

To validate the developed numerical model, a specialized test rig was designed and manufactured. Miniature high-speed inductive position sensors were mounted inside the swashplate of a commercially manufactured pump with only minimal modifications. These six sensors measured the distance between the sensor face and the slipper land as the slipper passed over the sensor, effectively measuring the direct film thickness in real time. The thickness of lubrication represents the greatest unknown predicted by the model and provides the most rigorous validation as well as experimental insight into actual slipper operation. New slippers were installed in the test rig, measured, and then following a period of operation, were measured again. A significant change in film thickness behavior was measured due to the presence of a worn slipper surface during the second period of testing, and this same behavioral change was captured with the simulation model.

The developed numerical model was used to conduct case studies demonstrating the potential of virtual pump lubrication design. Slipper sensitivity to operating conditions and materials were explored. Operational changes such as slipper tipping and liftoff at high speeds were numerically observed and would serve to aid a designer in improving the robustness of a design. A multi-modeling approach using a surrogate model based upon a design of experiment study and the full numerical model explored the inter-dependence of variables in a multi-land slipper design. In particular, a decrease in total power loss while increasing the outer stabilizing land width at a constant hydrostatic balance factor was observed for low pressure operation.

CHAPTER 1. INTRODUCTION

1.1 Background

Swashplate type axial piston pumps and motors are used in diverse types of hydraulic systems, including construction, agriculture, and aerospace market segments. The popularity of axial piston pumps stems from their compactness, relative ease in controlling the effective fluid displacement per shaft revolution, and high pressure operation. These features do come at the cost of additional design complexity when compared to other positive displacement machine designs, but nevertheless many applications demand the additional capabilities. Parts of a single axial piston machine can be partitioned into a few groups each serving a principal function: The outer pump case serves to separate the remaining components from the outside world, the pump end case contains channeling to connect flow from the displacement chambers to the suction and discharge ports, in the case of a variable displacement machine, a control system is used to vary the machine displacement per shaft revolution, and finally the main rotating kit realizes the pumping action. It is this rotating kit which forms the heart of a swashplate type axial piston pump or motor and a cross section is illustrated in Figure 1.1. Within the rotating kit, multiple pistons are arranged on a given pitch radius around the main pump shaft. The pistons are encased by a cylinder block which is connected to the main pump shaft, often through a mechanical spline. In pumps designed for only low working

pressures, the pistons can be directly supported on the swashplate without using a slipper. However, in piston/slipper designs as shown in Figure 1.1, a ball and socket joint attaches a slipper to the piston. The slipper is used to balance high piston pressure forces through a combination of hydrostatic and hydrodynamic fluid pressure which develop between the slipper and swashplate. The piston / slipper assembly press on an angled swashplate, forcing a linear reciprocating motion of each piston as the cylinder block rotates. This reciprocal motion causes an increase and decrease of the displacement chamber volume, thus suction and discharge of fluid, enabling an effective pumping action.

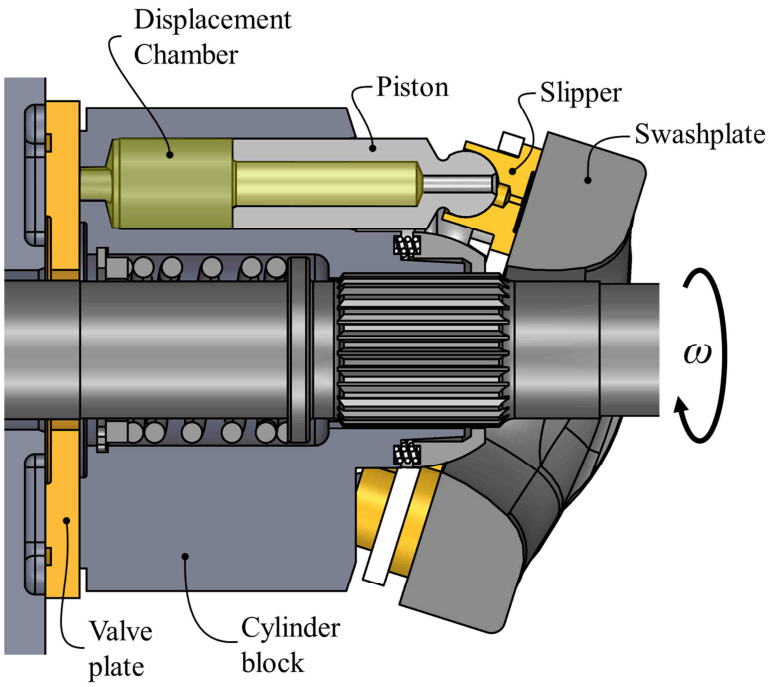

Figure 1.1. Cross-section of an axial piston hydraulic pump rotating kit.

Depending on the loading of the hydraulic system, significant pressures can develop in the working fluid. This fluid pressure, often on the magnitude of 20-40 MPa, pushes the cylinder block towards the valve plate and the piston/slipper assembly towards the swashplate with great force. These large forces must be transmitted across the relative

motion of cylinder block-valve plate and slipper-swashplate. Additionally, due to the inclination of the swashplate, the slipper reaction force pushes the piston laterally against the cylinder block. Unlike many traditional bearing designs which exhibit large ratios of rolling versus sliding motion, the relative motion between the pump rotating kit components is exclusively sliding in nature. Because of this, a full film of lubricant is required between the components to prevent persistent component wear and enable long-lasting pump operation.

In fluid film lubrication, two solid bodies are fully separated by a thin film of lubricant. This thin fluid, only micrometers thick, is sufficient to prevent the asperities of the solid bodies from contacting each other and thus prevent surface wear. In addition to preventing wear, the viscous friction during full film lubrication is significantly less than the friction present during boundary lubrication, which improves the efficiency of the sliding interface. Full fluid film lubrication requires pressure of the lubricant to be large enough such that the integrated pressure force is equal to the external forces being transmitted across the interface. The lubricant pressure generation can occur in two distinct physical manors: hydrostatic or hydrodynamic. Hydrostatic lubrication pressure generation is the more trivial case where fluid outside the thin film region is at an elevated pressure which is transmitted by normal fluid stresses into the lubrication region. Because the generation of fluid pressure occurs externally, no relative motion of the bounding bodies is actually required. In contrast, hydrodynamic pressure generation requires relative motion, and often an inclination, of the bounding bodies.

Fortunately, in the design of most axial piston pumps, the working hydraulic fluid bounds a portion of the lubrication region causing hydrostatic lubrication. The larger the

lubricating area, the stronger the equivalent lubricant force acts on the cylinder block or slipper. If the fluid film pressure force exceeds the force from the working hydraulic fluid pressure, the cylinder block or slipper will lift away from the valve plate or swashplate, respectively. Although this would seem desirable since metal-to-metal contact is now avoided, unfortunately the working hydraulic fluid will simultaneously leak through these large gaps, drastically reducing the ability of the pump to effectively discharge fluid. Therefore, an extremely careful balance is required so the slipper and cylinder block only slightly lift away from their opposing surfaces yielding full film lubrication to prevent wear while simultaneously keeping the thickness of the lubricant low enough to prevent excessive leakage of the pumping fluid. To further complicate the problem, axial piston pumps operate over a wide range of shaft speeds, fluid pressures, and swashplate angles. Because of the delicate balance needed to achieve effective lubrication, adaptive elements are included in the design of the cylinder block and slipper to enable the lubricant pressure to respond dynamically to the varying externally applied loads. This dynamic lubricant pressure response means that while a significant portion of the lubrication pressure occurs hydrostatically, hydrodynamic pressure generation is essential to effective operation.

Hydrodynamic pressure sources or sinks can originate from a number of physical effects within both the lubricant and the bounding solid bodies. First, the lubrication viscosity has a strong impact on the magnitude of the hydrodynamic pressure. Because the typical lubricating fluid, mineral oil, has a strong temperature-viscosity dependence, temperature changes of the lubricant will affect the hydrodynamic pressure. The fluid film is by definition quite thin, and since a strong conduction of heat between the fluid and

bounding solid bodies is possible, the surface temperature of the solid bodies impacts the temperature of the fluid film itself.

It is not only fluid temperature-viscosity changes which affect the hydrodynamic pressure. The pressure of the working and lubricating fluid is quite large which in turn loads the bounding solid bodies with significant normal forces. The compliance of the bounding solid bodies causes elastic deformation which changes the thickness of the fluid film. Similarly, non-uniform heating or bi-metal component construction will cause thermo-elastic deformation of the solids, and whenever the fluid film thickness is modified, hydrodynamic pressure generation is affected.

Because proper lubrication of the rotating kit is so critical to long-term efficient operation of the hydraulic pump, it is a major focus of axial piston pump and motor design. Unfortunately, because the physical phenomenon associated with lubrication is so complex and sensitive, gross analytical approximations are still necessary from a design standpoint.

This work will focus exclusively on studying the lubrication between the slipper and swashplate sliding interface inside of an axial piston machine. Previous modeling for the sliding interfaces between the piston and cylinder (Pelosi, 2012) and the cylinder block and valve plate (Zecchi, 2013) have been reported. Although there are similarities in the tribological operation between the three primary swashplate type axial piston machine sliding interfaces, significant differences in the underlying physics of the slipper as well as novel advancements in the lubrication modeling approach will be undertaken as part of this work.

1.2 State of the Art

A significant amount of research into the lubrication phenomena of axial-piston pump slippers has been conducted by numerous researchers throughout the world. Beginning in the 1960's, Shute and Turnbull (1962a, 1962b) investigated the operation of the slipper analytically, assuming it to be a purely hydrostatic bearing, and experimentally. In 1983, Hooke and Kakoullis developed a hydrodynamic slipper model using a short bearing approximation and truncated Taylor series to approximate the Reynolds equation governing pressure distribution under the slipper sealing land. Additional analytical expressions were developed to satisfy load, flow, and moment equilibrium requiring some numerical iteration to couple with the Reynolds expression. The model predicted that for hydrodynamic pressure to properly balance the net force and moments acting on the slipper, the slipper sealing lands must not be perfectly flat.

Hooke and Li (1988) expanded the complexity of the previously developed model by using a finite difference method to solve for the polar form of the Reynolds equation without a short bearing approximation. This improvement allowed analysis of complex non-flat slipper profiles and the model was used to analyze overclamped, centrally loaded slippers. Additionally, a test rig was built (Hooke and Kakoullis, 1979) to directly measure the fluid film thickness under a slipper using capacitive sensors. Measurements of minimum gap height from the test rig were compared to predicted values and a simple empirical equation was fit to the data that predicts minimum slipper gap given just a few parameters. However due to experimental limitations, the sensor implementation required significant pump modifications. Due to these modifications, inertial and centrifugal

forces which impact slipper operation were eliminated and the structural deformation of the swashplate was significantly altered.

Similar work (Hooke and Li, 1989; Koc et. at., 1992; Koc and Hooke, 1996) continued to use numerical models and experimental measurements to investigate the impact of tilting moments, orifice size, non-flatness profiles, and overclamp ratio on slipper performance. Koc and Hooke (1997) published general considerations to be made in the design of slippers and concluded: “For a successful slipper operation, slippers require a slightly convex surface on the running face.” Although these works emphasized the necessity of non-flatness in slipper operation, they did not discuss the origin.

Pang et. al. (1993) used a laser holographic photoelastic experiment to measure the pressure deformation of a slipper, however the design tested was abnormally stiff and details of experimental results are somewhat lacking. Kazama and Yamaguchi (1993) developed a mixed-friction model for a hydrostatic bearing but only considered the impact of Elastohydrodynamic Lubrication (EHL) on the asperity contacts, and neglected the compliance to pressure of the overall bearing body. Yabe et. al. (1997) considered the impact of slipper non-flatness due to run-in wear as an essential factor for successful bearing operation.

Manring et. al. (2002) studied the impact of linear deformations on stationary hydrostatic thrust bearings using analytical expressions. In particular the operational differences between concave and convex deformations were examined and a general conclusion that concave deformations tend to increase, while convex deformations decrease, the load carrying capacity of the slipper was drawn. However, this analysis applied to stationary thrust bearings and assumed the rigid position of the bearing to be parallel to the opposite

bounding surface, thus limiting the applicability of its general conclusions to slipper-swashplate interface. Manring et. al. (2004) performed analytical analysis coupled with experimental measurements of the pressure profile between a slipper and swashplate. The measured pressure and leakage data was used to fit a deformation and film thickness profile using the analytical expressions. Additionally, the impact of socket geometry on leakage and fluid thickness was investigated. However, the experiment was performed on a stationary slipper thus eliminating hydrodynamic pressure generation.

More recently, work by Bergada et. al (2010) studied multi-land slippers without venting grooves. Analytical expressions are developed for pressure profiles and leakages, although the slipper is assumed to be stationary. Full Navier-Stokes models (Kumar et. al., 2009) are able to calculate fluid film pressure and leakage with tangential velocity, however this model assumed the slipper to be parallel to the swashplate. These numerical models were compared to experimental measurements capable of measuring an average fluid film thickness and pressure profile distribution for both stationary and dynamic operating conditions. A number of design parameters and operating conditions were perturbed and the impacts of leakage and slipper performance were evaluated, however non-flatness was not studied in particular. Further work in Bergada et. al. (2011) formulates a complete, although somewhat simplified, analysis of axial piston pump leakages. Experimentally, Bergada et. al. (2012) measured the transient micro motion of the cylinder block using inductive position transducers. Three sensors were installed into the endcase of a pump and measured the distance between the sensor face and the cylinder block face. Note that the sensors were positioned such that they measured a

portion of the cylinder block radially outward of the actual sealing land surfaces and thus the sensors themselves were not subjected to large pressures.

Complementing the experimental work of Bergada, Canbulut et. al. (2009) measured viscous/mixed fiction on the swashplate coming from the slippers for a number of slipper designs and operating conditions. This work also measured and varied the surface roughness of the slipper and swashplate. Considering surface roughness was particularly important in their study because many of the slipper designs tested had very high clamping-ratios where full fluid film lubrication support is not possible and the effects of asperity contact become non-negligible.

Both numerical (Kazama, 2005) and experimental (Rokala, 2008) studies of tribological lubrication between the slipper and swashplate for water hydraulic axial piston pumps have also been conducted. Mixed lubrication is considered due to the differing lubricating properties of water versus oil hydraulics. The work of Rokala and Koskinen (2010) investigated the pressure deformation profiles of composite PEEK and stainless steel slipper designs. However, their analysis only considered a hydrostatic pressure field without any other coupling. The numerical work of Kazama includes transient squeeze film effects in the pressure profile, something not considered in most of the other previously mentioned works.

Considering the squeeze film effect from transient part micro-motion had actually been considered earlier by Fang and Shirakashi (1995), however they modeled the piston-cylinder interface, not the slipper-swashplate. The work of Fang was then extended in principal to all the lubricating interfaces of an axial piston machine by Kleist (1997) in an iteration scheme that balanced external loads with pressure and contact forces. Although

Kleist's work presented a method generally applicable to all the piston machine lubricating interfaces, the piston cylinder interface was the primary focus. A conceptually similar model was developed by Deeken and Murrenhoff (2001) by coupling two external softwares, DSHplus and ADAMS.

In 2002, Wieczorek and Ivantysynova developed a non-iosthermal fluid flow model for all three interfaces of an axial piston machine and considered the transient squeeze film effect. In their model, a part micro-motion velocity is found at every point in time which develops the necessary fluid film pressure to exactly balance all the external loads. By integrating over a number of shaft revolutions, the full micro-motion of the piston, cylinder block, and slipper can be found. Huang and Ivantysynova (2003; 2006) further developed the model of Wieczorek by now considering the elastohydrodynamic pressure deformation effect coupled with part micro-motion for the cylinder block-valve plate and piston-cylinder interfaces. Pelosi and Ivantysynova (2008) extended the work of Huang to the slipper swashplate interface by calculating pressure deformation and the resulting fluid structure interaction, although the deformation model used was rather coarse and the fluid-structure coupling was weakly enforced. Further developments considering higher fidelity pressure deformation models, stronger coupled fluid structure interaction, and solid body temperature distributions / thermal deformations have been accomplished for both the piston-cylinder interface (Pelosi and Ivantysynova, 2012) and the cylinder block-valve plate interface (Zecchi and Ivantysynova, 2012). Xiong et. al. (2010) used a similar solution scheme to solve for journal bearing lubrication, but without calculating thermal effects of the solid bodies.

Similar thermal-fluid-structural analysis for the lubrication between the lateral bushings in external gear positive displacement machines has recently been published by (Dhar and Vacca, 2013). Experimental work by Dhar (2013) measured the fluid film thickness between a lateral bushing in an external gear machine and the pump housing. Although the sensor was subjected to high fluid pressures, high dynamics were not necessary as there is not sliding motion between the bushing and housing.

1.3 Research Objectives

This work aims to discover a method for understanding the fundamental relationship between the design of a slipper and the resulting lubrication performance. Because the lubricating regime between the slipper and swashplate is difficult and costly to observe experimentally, the bulk of the research focuses on the development of a numerical model to simulate the lubrication domain. Consequently, the research objects are as follows:

- Development of a multi-physics, multi-scale, transient numerical model to simulate micro-motion of the slipper and thermal-fluid-structure interactions between the domains.
- Direct experimental measurement of slipper lubrication behavior.
- Case studies of numerical experiments investigating slipper lubrication performance.

These research objectives are accomplished by:

- Discovery of the necessary numerical/modeling considerations required to achieve a realistic and robust numerical simulation.

- Simulation case studies to demonstrate the ability to numerically predict the change in slipper performance with design changes.
- The design, construction, and operation of a novel test rig for experimental measurement of fluid film thickness between the slipper and swashplate in an operational hydraulic pump with minimal modifications.

The final product of this research enables a new approach to lubrication design of the slipper / swashplate bearing. A high fidelity numerical model can drive the initial design of both traditional as well as novel pump designs, significantly reducing the time and cost of physical prototype testing. Not only does the model provide efficiency predictions in terms of leakage and torque loss, but also deep insight into the slipper behavior which before this work was at best conjecture.

CHAPTER 2. SLIPPER LUBRICATION OPERATION

In the simplest axial piston pump design, the slipper is actually completely eliminated. In this slipper-less piston pump design (Figure 2.1), a piston with a spherical end will slide directly across the swashplate. The force from the displacement chamber pressure, F_{DK}, pushing on the piston is directly reacted by the swashplate. Since the interface between the piston and swashplate will not support significant traction loads, the swashplate reaction force must be normal to the surface. Because of this, the magnitude of the swashplate reaction force must be $F_{DK}/\cos(\beta)$ so the component of the reaction force parallel to the piston axis still opposes F_{DK}.

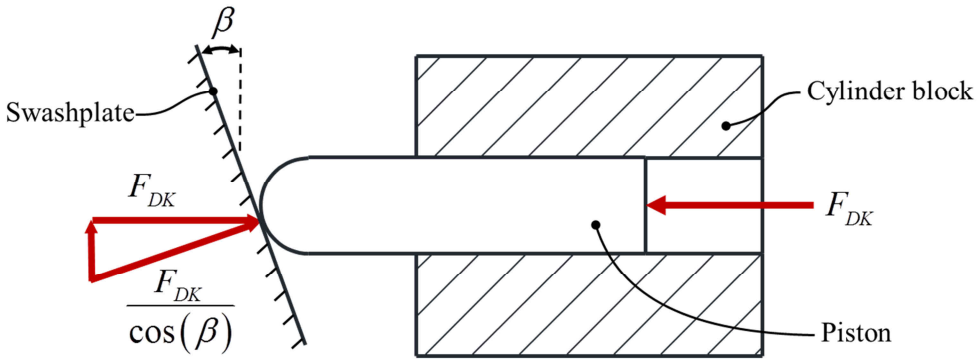

Figure 2.1. Slipper-less piston design.

Although this same swashplate reaction force is also required from slipper designs, this slipper-less design transmits the force over a small area, and without hydrostatic assistance, resulting in high contract stresses. Hard elastohydrodynamic lubrication conditions prevail in this contact regime and thus the continuous working pressure is

significantly limited. Different designs incorporating roller or thrust bearings into either the swashplate face or the piston end to increase this working pressure limit have been patented, but generally a hydrostatic slipper provides better performance and allows for higher working pressures than the alternatives.

Of slipper designs which incorporate a hydrostatic component, the single sealing land slipper design of Figure 2.2 is likely the most common today in commercially manufactured hydraulic axial piston units. In this design, the slipper is manufactured with a socket which is swaged around the piston head. Two different domains of fluid exist between the slipper and the swashplate. Fluid enters the slipper pocket volume from the displacement chamber through a hole drilled down the center of the piston. The fluid within this volume is at a nearly uniform pressure due to the relatively large height of the pocket. Pressurized fluid within the pocket leaks through the small gap between the sealing land and swashplate into the pump case. It is the fluid within this small gap that prevents metal to metal contact between the slipper and swashplate and is thus termed a thin lubricating film. The pressure distribution between the sealing land and swashplate is dependent on many parameters, but if the pressure force becomes insufficient compared to external loads, the fluid film collapses and boundary friction occurs.

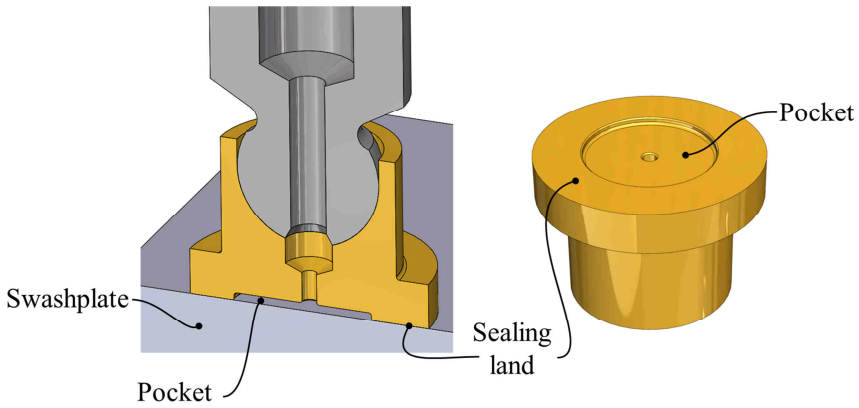

Figure 2.2. Single land slipper design.

An alternative to the slipper design of Figure 2.2 is where the ball portion of the piston-slipper joint is placed on the slipper and instead the piston end contains a socket. This 'male' slipper design is illustrated in Figure 2.3. An advantage of this design is that the overall length of the piston-slipper assembly is shortened which reduces the bending moment of the piston, allowing for larger swashplate angles.

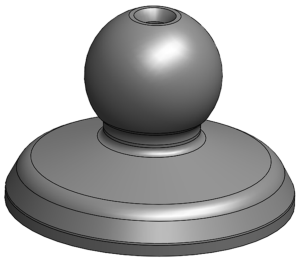

Figure 2.3. Male slipper design.

Variations to the slipper sealing land design itself are also quite common. The most popular is to reduce the width of the sealing land and add additional stabilizing lands radially in and outwards as illustrated in Figure 2.4. A radial groove in the inner stabilizing land connects pocket pressure to the first circumferential groove. From a hydrostatic pressure prospective, the inner stabling land does not cause any affect. The same is the case for the outer stabilizing land; a radial groove connects the

circumferential groove to case pressure eliminating any hydrostatic effect of the outer land.

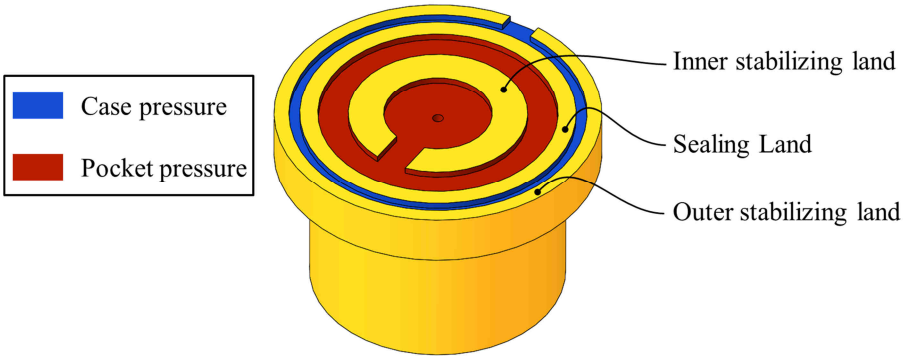

Figure 2.4. Triple land slipper design.

2.1 Fluid Film Bearings

To better understand the origins of the single landed slipper design, it is helpful to briefly review fluid film bearings in general. Many traditional fluid film bearings utilize hydrodynamic pressure generation to support externally applied loads. This type of pressure generation requires relative motion of the two bounding surfaces, and the magnitude of pressure generation is proportional to the boundary velocity. An alternative to the hydrodynamic fluid film bearing is one which operates instead on hydrostatic pressure, and this classical design is illustrated on the left of Figure 2.5. In this hydrostatic bearing, an externally pressurized pocket of fluid and associated sealing lands are able to generate sufficient fluid pressure to support large axial loads. This is particularly advantageous when the boundary velocities of the surfaces are low compared to the bearing load. In the design on the left of Figure 2.5, as the top plate moves further away from the bottom, the bearing fluid leakage will increase. Because an orifice is

introduced between the constant pressure source and the fluid pocket, the pocket pressure will drop due to an increase in flow across the orifice.

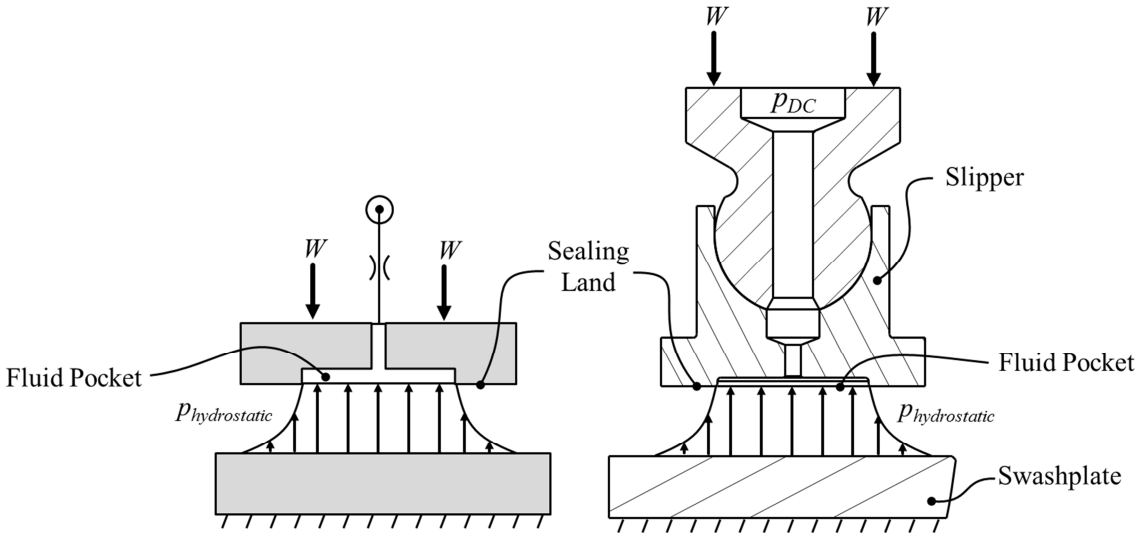

Figure 2.5. An orifice compensated hydrostatic bearing (left), slipper-swashplate hydrostatic pressure distribution (right).

The top surface will continue to lift away from the bottom portion of the bearing until the bearing pressure force exactly balances the applied load, *W*. Because of this inherent lubricating self-adjustment, provided the supply pressure is large enough to achieve bearing liftoff, a wide range of external loads can be supported. Moreover, since a hydrostatically supported bearing can have fluid film thicknesses significantly larger than their hydrodynamic counterpart, they typically are characterized by extremely low interface friction. Of course, these advantages come at the cost of the necessity for an external pressure source.

It is by no coincidence that the mechanical design of slippers inside axial piston pumps closely resembles this classical hydrostatic fluid film bearing as illustrated in the similarities between Figure 2.5 (left) and Figure 2.5 (right). During high pressure operation of the axial piston pump, the slipper must support significant axial loads often

at speeds insufficient for adequate pure hydrodynamic pressure generation. Frequently the need for an external pressure source is a major drawback to the hydrostatic bearing design, but in the case of an axial piston pump slipper, the displacement chamber pressure (p_{DC}) itself is able to serve this purpose. While it initially seems fortuneous to utilize the displacement chamber pressure for slipper lubrication, it comes at a cost of overall pump efficiency. Fluid which leaks from the displacement chamber and out of the slipper into the main pump case is fluid which no longer enters the hydraulic circuit to do useful work. An extremely careful balance is therefore required to ensure adequate lubrication while simultaneously maintaining high pump efficiency. To better understand how this lubrication performance is impacted, a more sophisticated analysis of the axial piston pump kinematics and forces is necessary.

2.2 Main Axial Piston Machine Kinematics

The shaft of an axial piston machine is connected to the cylinder block often through a mechanical spline. The spline couples the shaft and cylinder block rotational motion together while allowing the cylinder block to move slightly in an axial direction and to tip about the x and y axis. This compliance is necessary to permit the fluid film lubrication between the cylinder block and valve plate to dynamically adjust its thickness as external loads vary. As the cylinder block rotates, the piston and slipper assemblies rotate around the shaft axis as well with the slipper remaining pressed to the swashplate. The inclination of the swashplate causes the piston and slipper to reciprocate over a shaft revolution with half of the effective piston stroke illustrated in Figure 2.6 and the full stroke calculated as:

$$h_K = 2R_B \tan(\beta) \tag{2.1}$$

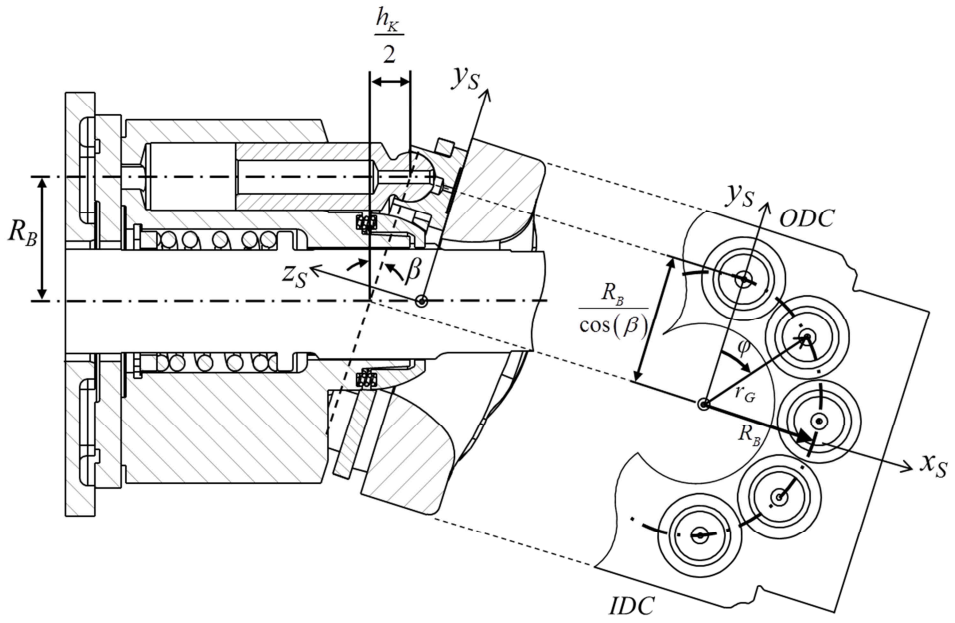

Figure 2.6. Piston stroke definition.

A global coordinate system used to describe the instantaneous position of all the slippers will be defined with respect to the swashplate, and is termed the swashplate coordinate system (x_S, y_S, z_S) as illustrated in Figure 2.6. The x-axis of this global coordinate system is parallel to the swashplate variable displacement rotation axis and the z-axis is normal to and pointing away from the swashplate surface. The coordinate system origin is defined at the center of the slipper motion path in the swashplate running face plane. The shaft rotational position angle, φ, is defined to be 0 at the positive y-axis. By convention, φ=0° corresponds to outer dead center in pumping mode and inner dead center instead during hydraulic unit motoring. Using the shaft angle, φ, defined in this global coordinate system, the instantaneous piston position displacement from outer dead center can be defined as:

$$s_K = R_B \cdot \tan\beta \cdot (1 - \cos\varphi) \tag{2.2}$$

Differentiating the piston position twice, the instantaneous linear acceleration of the piston and slipper is given by Eq. (2.3) where ω is the shaft rotational velocity.

$$a_K = \frac{d^2 s_K}{d\varphi^2}\omega^2 = \omega^2 R_B \tan(\beta)\cos(\varphi) \tag{2.3}$$

Closely inspecting Figure 2.6, the piston centerline remains at a constant radius, r_B, from the shaft centerline throughout the revolution. However, when the swashplate is non-orthogonal to the pump shaft axis, the slipper center follows an elliptical path as illustrated on the right of Figure 2.6. The major ellipse axis has a length of $2 \cdot R_B / \cos(\beta)$ and the endpoints of the major ellipse axis coincide with the shaft angle at inner dead center (IDC) and outer dead center (ODC). The minor ellipse axis does not vary with swashplate angle and has a length of $2 \cdot R_B$. The instantaneous radius of the slipper center from the swashplate center as a function of shaft angle can be expressed as:

$$r_G = \sqrt{\left(R_B \sin(\varphi)\right)^2 + \left(\frac{R_B}{\cos(\beta)}\cos(\varphi)\right)^2} \tag{2.4}$$

A large portion of this work focuses on the behavior of a single slipper at an instant in time. Because a periodic steady state operation of the pump is assumed, once the behavior of a single slipper over an entire shaft revolution is determined, those results can be duplicated, appropriately phase shifted, and combined to calculate the performance of all *n* slippers inside an axial piston unit. Therefore, to best describe the behavior of a single slipper, a coordinate system is defined using a reference slipper body. Because this coordinate system is only used over a spatial domain limited to a single slipper, it is termed local. The origin of the slipper coordinate system is located at the center of the

circular sealing land in the sealing land face plane and lies in the path defined by Eq. (2.4). The z-axis is normal to the sealing land face, pointing towards the slipper socket. The positive x-axis points in the instantaneous direction of slipper tangential motion and by the right hand rule, the y-axis points radially outwards. Because this coordinate system moves with the slipper and is constantly rotating, a cross-section of the fluid film in x-z plane will always show the slipper moving directly to the right. This local slipper Cartesian coordinate system (x_G, y_G, z_G) is illustrated in Figure 2.7.

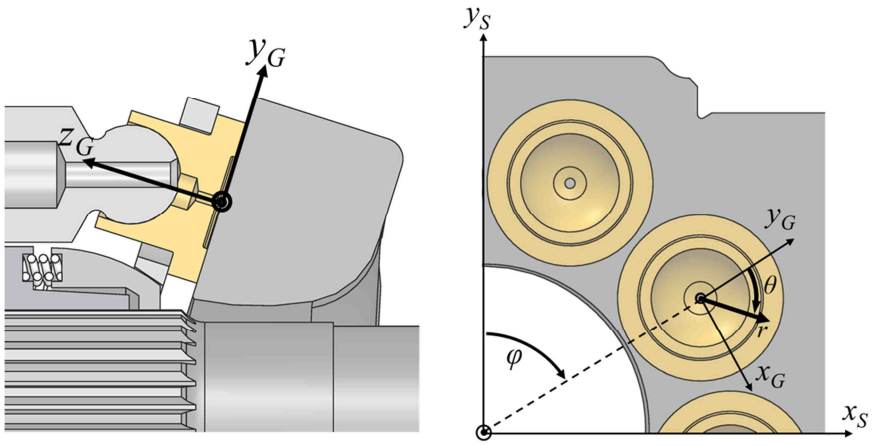

Figure 2.7. Local slipper coordinate systems.

An equivalent cylindrical coordinate system (r, θ, z_G) localized over a single slipper domain can also be defined as illustrated on the right of Figure 2.7. Both cylindrical and Cartesian coordinate systems share a common origin and z-axis, but in the cylindrical system, $\theta = 0°$ coincides with the Cartesian system y axis and revolves clockwise. The cylindrical coordinate system definition will be convenient when working with the polar discretization of the thin film fluid.

Using this coordinate system defined for a single slipper, the complete motion of the single slipper motion can be analyzed. Although the motion of the slipper around the

main pump shaft is clear, the possibility for rotation of the piston-slipper assembly about its own axis is not obvious. This secondary rotation is defined by a variable $speed_K$ which is equal to zero if no relative rotation between the piston and cylinder bore is present and $speed_K$ = 1 if the relative piston rotation equals the main pump shaft speed. Several previous researchers have investigated this phenomenon (Renius, 1974; Hooke and Kakoullis, 1981; Lasaar, 2003). Ivantysynova and Lasaar (2000) designed a special test rig designed to directly measure the presence of circumferential friction between the piston and block bushing. The outcome from these multiple works confirms the presence of a relative rotation between the cylinder bore and the piston. For piston relative rotation to be present, the slipper must be translating ellipsoidally as opposed to purely rotating about the shaft axis. Therefore, this work makes the same assumption and sets $speed_K$ = 1. Figure 2.8 contrasts the slipper rotational motion for both extremes of $speed_K$ by illustrating the location of a fixed point on the slipper body and how its position will differ for different $speed_K$ values.

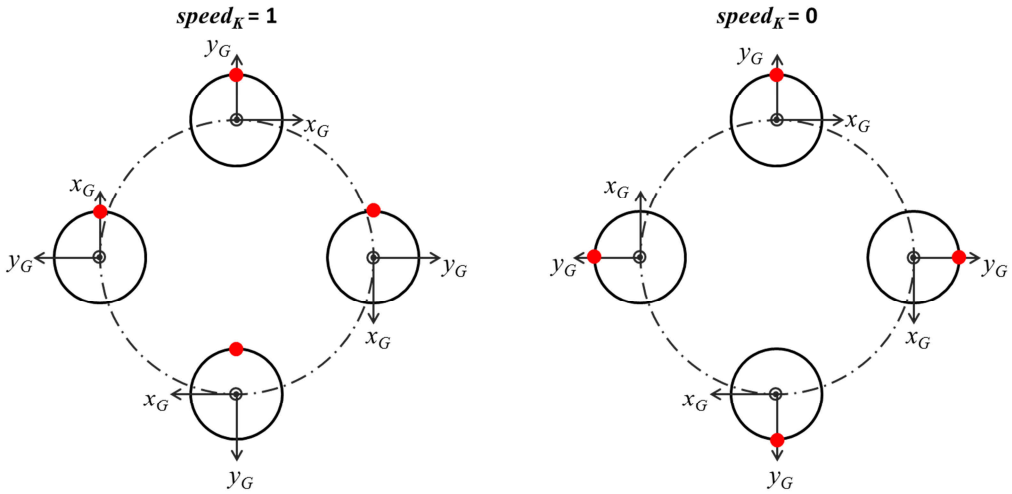

Figure 2.8. Comparison of a fixed point (red) on the slipper body over a shaft revolution for the two extreme values of $speed_K$.

Now that both the main velocity of the slipper about the pump shaft and the rotation of the slipper about the piston axis are defined, an expression for the instantaneous slipper velocity distribution in the slipper local cylindrical coordinate system can be defined for a given pump shaft speed, ω:

$$
\begin{aligned}
&v_{xG}(r,\theta) = \omega c_1 \cos(c_2) \\
&v_{yG}(r,\theta) = \omega c_1 \sin(c_2) - \omega \cdot r \cdot speed_K \\
&where: \\
&c_1 = \sqrt{r^2 + {r_G}^2 - 2 r_G r \cos(\pi - \theta)} \\
&c_2 = \frac{\pi}{2} - \cos^{-1}\left(\frac{{c_1}^2 + r^2 - {r_G}^2}{2 c_1 r} \right)
\end{aligned}
\tag{2.5}
$$

2.3 Slipper Free Body Diagram

A number of forces act on the slipper body, the largest of which comes from the displacement chamber pressure. Even during steady state machine operation, because the displacement chamber switches between suction and discharge pressure once every revolution, the instantaneous forces acting on the slipper vary greatly with time. Figure 2.9 illustrates the forces considered as part of this analysis.

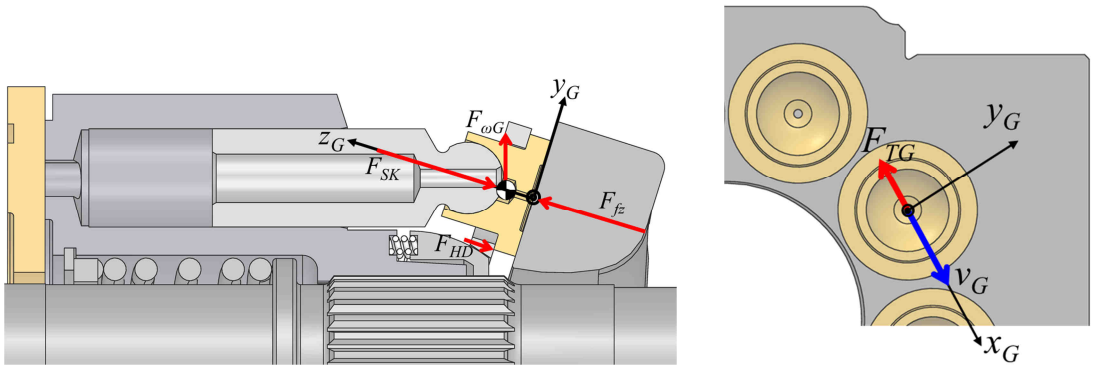

Figure 2.9. Free body diagram of slipper forces.

The primary force is the clamping force coming from the piston, F_{SK}. This single force can be decomposed into multiple components. First, the displacement chamber pressure

loads the piston face with an equivalent force F_{DK}. An inertial force, F_{aK}, stemming from the linear acceleration and deceleration of the piston-slipper assembly as it reciprocates acts at the center of mass. A third force, F_{TK}, acting in a direction parallel to the piston centerline is the viscous friction between the piston and cylinder bore opposing the direction of piston motion. These forces are illustrated in Figure 2.10.

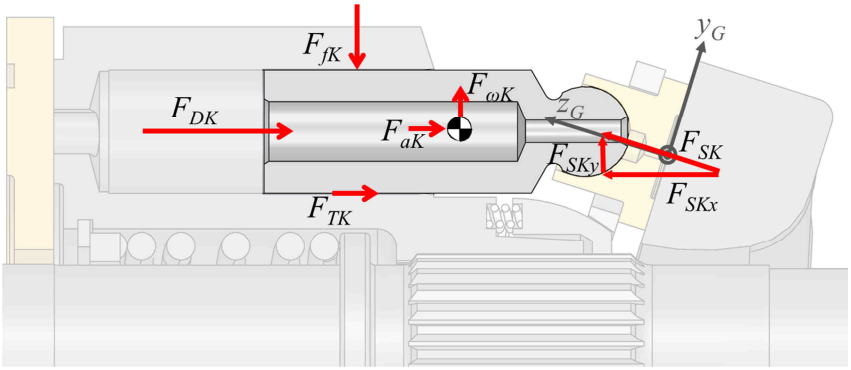

Figure 2.10. Partial free body diagram of piston forces.

The resultant of these three forces must be transmitted to the ball joint, through the slipper and lubricating film to the swashplate and pump case; this is however not directly possible. Because the swashplate is inclined with angle β, the resultant force would decompose into both a normal and a shear force at the swashplate face. This interfacial shear force would need to be frictionally carried, and the lubricant between the slipper and swashplate makes transmission of a sizeable shear force between the slipper and swashplate impossible. Therefore, the reaction force from the swashplate through the ball joint is normal to the swashplate face. This reaction force, with an equal but opposite magnitude of F_{SK} illustrated in Figure 2.9, can be decomposed into a force component parallel (F_{SKx}) and perpendicular (F_{SKy}) to the piston axis. The force component F_{SKx} opposes the sum of F_{DK}, F_{aK}, and F_{TK} as seen in Eq. (2.6). The radial force component

F_{SKy} causes a side loading of the piston which must be countered by the fluid film pressure, F_{fK}, between the piston and cylinder bore.

$$F_{SKx} = F_{DK} + F_{aK} + F_{TK} \tag{2.6}$$

The friction force between the piston and cylinder bore, F_{TK}, is impossible to determine analytically for all but the simplest case when the piston is concentric to the bore. Without a numerically simple but realistic approximation, this work neglects F_{TK}. Since the magnitude of piston friction is generally small compared to the total piston force, this approximation is reasonable. Research of Pelosi (2012) uses a multi-physics numerical model to predict the values of F_{TK}, and if these simulation results are present, they can be considered for increased completeness. The value of F_{SKx} can be calculated with Eq. (2.7) where p_{DC} is the instantaneous displacement chamber pressure (shaded area of Figure 2.11), a_K is found using Eq. (2.3), and m_K is the mass of the piston and slipper assembly.

$$F_{SKx} = \frac{\pi}{4}\left(d_K{}^2 - d_{dG}{}^2\right) \cdot p_{DC} + m_K \cdot a_K + F_{TK} \tag{2.7}$$

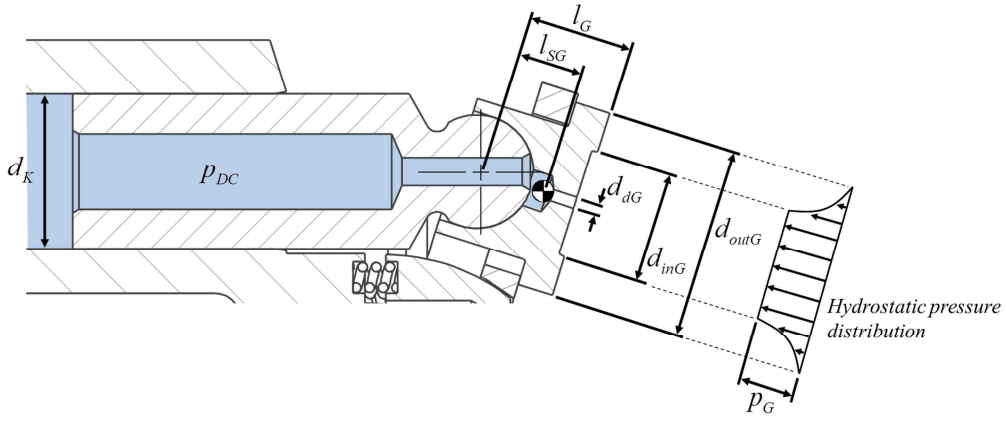

Figure 2.11. Slipper dimensions and pressure distributions.

Finally, the instantaneous value of F_{SK} can be calculated as:

$$F_{SK} = \frac{F_{SKx}}{\cos(\beta)} \tag{2.8}$$

Returning to the other forces illustrated in Figure 2.9, the centrifugal force $F_{\omega G}$ acts at the slipper center of mass with a magnitude:

$$F_{\omega G} = m_G R_B \omega^2 \tag{2.9}$$

This centrifugal force, caused by the rotation of the slipper around the pump axis, tends to tip the slipper such that the point on the slipper radially away from the pump shaft has a higher film thickness compared to the inner point. Since the centrifugal force acts at the slipper center of mass but the reaction force occurs at the center of the piston head, a tipping moment about the slipper local coordinate system x-axis is created:

$$M_{\omega G} = F_{\omega G} \cdot l_{SG} \tag{2.10}$$

were l_{SG} is the distance between the slipper center of mass and the center of the piston head as illustrated in Figure 2.11.

F_{HD} is a constant force pushing the slippers towards the swashplate coming from the springs located between the slipper retainer and the cylinder block. In the event of a pump design featuring a fixed hold down mechanism, F_{HD} would be included using a penalty contact scheme. In this scheme, when the clearance between the slipper and swashplate exceeds the nominal design clearance, F_{HD} is applied with a magnitude proportional to the amount of running clearance exceeded.

The viscous friction in the thin fluid film drags on the slipper lands with a direction opposite of the slipper motion. The viscous shear stress is integrated over the lubrication area to calculate the F_{TG} magnitude:

$$\tau = \mu \frac{\partial V}{\partial h}$$
$$F_{TG} = \int_A \tau dA \tag{2.11}$$

Similar to the slipper centrifugal force, since the viscous friction force acts at the slipper running face but is reacted at the center of the piston head, and thus a moment results. The magnitude of this moment which acts about the slipper local coordinate system y-axis can be calculated:

$$M_{TG} = F_{TG} \cdot l_G \tag{2.12}$$

The final force in the free body diagram of Figure 2.9 is the lubrication fluid force, F_{fz}. This force is calculated by integrating the pressure in the sealing lands and slipper pocket.

$$F_{fz} = \frac{\pi}{4}\left(d_{inG}{}^2 - d_{dG}{}^2\right) + \int p \, dA \tag{2.13}$$

Because the slipper land pressure field will likely not be radially symmetric, fluid moments about the x and y axis of the slipper local coordinate system are:

$$M_{fx} = \int \left(p \cdot x_G \right) dA$$
$$M_{fy} = \int \left(-p \cdot y_G \right) dA \tag{2.14}$$

where x_G and y_G are the Cartesian coordinates of the slipper local coordinate system as illustrated in Figure 2.7.

2.4 Analytical Analysis of Slipper Lubrication Performance

As previously discussed, the primary role of the slipper lubrication interface is to transmit the piston force to the swashplate while preventing long-term wearing. A good slipper design accomplishes this load transmission while simultaneously minimizing power loss due to either friction or fluid leakage. Fortunately, if the complex physical phenomena

surrounding the lubrication are simplified, analytical solutions exist to predict the carried load, friction, leakage, and fluid film thickness.

This analysis begins by simplifying the free body loads discussed in the previous section. Using the free body diagram of Figure 2.9, $F_{\omega G}$ and F_{TG} are neglected because they create moments about the ball joint instead of acting directly normal to the swashplate. Equation (2.8) can be used to determine the primary applied force, but in this case the inertial term of Eq. (2.7) is neglected as it will vary with shaft position. Therefore, a simplified value for F_{SK} is

$$\tilde{F}_{SK} = \frac{\pi\left(d_K{}^2 - d_{dG}{}^2\right)\cdot p_{DC}}{4\cos\beta} + F_{HD} \tag{2.15}$$

where F_{HD} can be neglected in the case of a fixed clearance pump hold down design. The Reynolds equation used to calculate the fluid film pressure over the slipper sealing lands will be described with detail in the next chapter. If the slipper and swashplate are assumed to be flat and parallel to each other the Reynolds equation can be simplified and an analytical expression (Hamrock, 2004) describing the lubricating film pressure as a function of radial distance, r, is:

$$p = p_G \frac{\ln\left(r / r_{outG}\right)}{\ln\left(r_{inG} / r_{outG}\right)} \tag{2.16}$$

where r_{inG} and r_{outG} are half of the diameters d_{inG} and d_{outG} as illustrated in Figure 2.11. Integrating the pressure field over the sealing land area and adding the pressure force from the slipper pocket, the resulting fluid force can be calculated as:

$$F_{fz} = \pi r_{Gin}{}^2 p_G + \int_{r_{inG}}^{r_{outG}} p_G \frac{\ln\left(r / r_{outG}\right)}{\ln\left(r_{inG} / r_{outG}\right)} 2\pi r\, dr = \frac{\pi p_G\left(r_{outG}{}^2 - r_{inG}{}^2\right)}{2\ln\left(r_{outG} / r_{inG}\right)} \tag{2.17}$$

The magnitude of force found by Eq. (2.17) represents the hydrostatic force generation available for a particular design. The most important factor in analytical analysis of a given slipper design is a ratio between the applied piston load and the hydrostatic fluid force generation, termed the balance factor (*B*):

$$B = \frac{F_{fz}}{F_{SK}} \tag{2.18}$$

Balance factor (B) values greater than 1 indicate excess hydrostatic pressure under the slipper causing it to lift away from the swashplate, while ratios less than 1 indicate the hydrostatic pressure alone is insufficient to bear the piston load. Many slipper designs have a balance factor less than 1 with the majority of values ranging from 0.85 to 1.0. In these 'underbalanced' designs, hydrodynamic pressure generation is required to prevent contact between the slipper and swashplate. During instances where the balance factor ratio is greater than 1, the orifice(s) between the displacement chamber and slipper pocket will limit the effective gap height.

Although in Eq. (2.17), the magnitude of fluid force is not directly dependent on fluid film thickness, the same will not be true for the fluid leakage and viscous friction. As the slipper lifts away from the swashplate and full fluid film lubrication is established, the volumetric flow out of the slipper pocket, as well as the viscous friction between the slipper and swashplate are:

$$Q_{SG} = \frac{\pi h_G^{\,3} \cdot p_G}{6\mu \ln\left(\frac{r_{outG}}{r_{inG}}\right)} \tag{2.19}$$

$$\tau = \mu \frac{\omega \cdot R_B}{h_G}$$
$$F_{TG} = \pi \left({r_{outG}}^2 - {r_{inG}}^2 \right) \cdot \mu \frac{\omega \cdot R_B}{h_G} \tag{2.20}$$

where h_G is the fluid film thickness between the slipper and swashplate. Moreover, both the volumetric and frictional power loss can be calculated:

$$P_{leak} = Q_{SG} \cdot p_G = \frac{\pi {h_G}^3 \cdot {p_G}^2}{6\mu \ln\left(\frac{r_{outG}}{r_{inG}} \right)} \tag{2.21}$$

$$P_{friction} = F_{TG} \cdot \omega \cdot R_B = \pi \left({r_{outG}}^2 - {r_{inG}}^2 \right) \cdot \mu \frac{\omega^2 \cdot {R_B}^2}{h_G} \tag{2.22}$$

A volumetric continuity between fluid entering the pocket through the slipper throttle and fluid leaving through the lubricating gap must be maintained. Fluid entering the pocket must flow from the displacement chamber through a narrow restriction machined into the slipper. This restriction causes a drop in fluid pressure proportional to the volumetric flow rate preventing excessive slipper liftoff if properly designed. The flow rate through the slipper orifice can be calculated assuming turbulent flow:

$$Q_{SG} = \alpha_D \frac{\pi {d_{dG}}^2}{4} \sqrt{\frac{2\left(p_{DC} - p_G \right)}{\rho}} \tag{2.23}$$

Equation (2.23) can be rewritten solving for pocket pressure:

$$p_G = p_{DC} - \frac{8\rho {Q_{SG}}^2}{\pi^2 \alpha^2 {d_{dG}}^4} \tag{2.24}$$

The p_G expression found in Eq. (2.24) can be substituted into Eq. (2.19) and then solved for Q_G to express slipper leakage as a function of displacement chamber pressure and fluid film thickness accounting for the impact of the orifice on pocket pressure. Adding

Eq. (2.21) and (2.22) together equals the total power loss due to both friction and leakage between the slipper and swashplate:

$$P_{lossG} = \frac{\pi h_G{}^3 \cdot p_G{}^2}{6\mu \ln\left(\frac{r_{outG}}{r_{inG}}\right)} + \pi\left(r_{outG}{}^2 - r_{inG}{}^2\right) \cdot \mu \frac{\omega^2 \cdot R_B{}^2}{h_G} \tag{2.25}$$

The variation of P_{lossG} with respect to fluid film thickness for a single slipper is illustrated in Figure 2.12. In this example, when the gap height is less than around 8 μm, viscous friction dominates the total power loss. As the film thickness increases, the viscous friction decreases while the leakage beings to increase. Obviously the pump working pressure and rotating speed will strongly influence the transition point location, but the trend of each line will nevertheless remain the same.

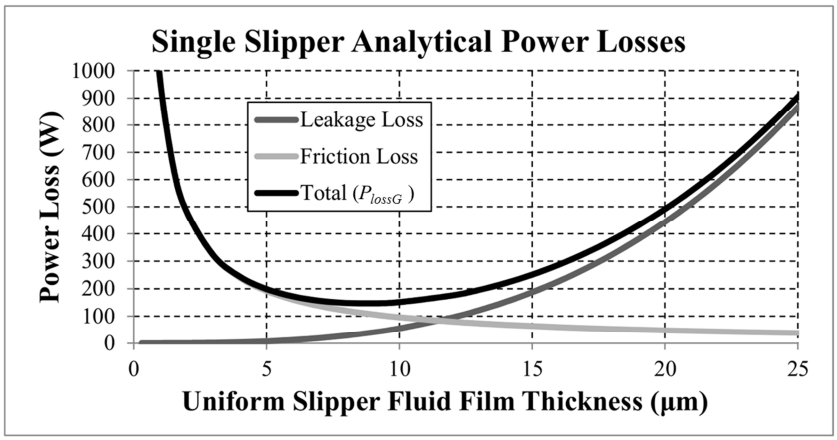

Figure 2.12. Analytical slipper power losses versus fluid film thickness.

Differentiating Eq. (2.25) with respect to gap height and solving h_G when the differential is equal to zero gives the optimal fluid film thickness for minimizing power loss:

$$h_{optG} = \frac{1}{p_G} \sqrt[4]{2 \cdot \mu^2 \cdot \omega^2 \cdot R_B{}^2 \cdot p_G{}^2 \left(r_{outG}{}^2 - r_{inG}{}^2\right) \cdot \ln\left(\frac{r_{outG}}{r_{inG}}\right)} \tag{2.26}$$

Although this film thickness will result in the minimal power loss, the magnitude of h_{optG} will very significantly with pump speed and pressure. Thus, it proves extremely difficult to design a slipper that operates at a near ideal film thickness under a wide range of pump operating conditions. Moreover, thermo-elastohydrodynamic effects are not included in this analytical analysis, which have a significant affect on slipper operation, and make this analytical analysis merely a starting point. For this reason, the development of a numerical model which can predict the non-uniform slipper lubrication film thickness at different operating conditions and component designs is necessary and is presented in the next chapter.

CHAPTER 3. FLUID-STRUCTURE-THERMAL MODEL OF SLIPPER SWASHPLATE LUBRICATION

To understand the lubrication performance between the slipper and swashplate, it is imperative to understand how separate physical phenomena interact to affect lubrication. Most of these effects individually can be modeled using partial differential equations derived from first principals. Although the previous analytical analysis attempted to describe slipper-swashplate lubrication performance, significant assumptions were made. The fluid film between the sealing lands and the swashplate was assumed to be a constant film thickness i.e., the slipper sealing land surface was parallel to the swashplate surface. This eliminates hydrodynamic pressure sources and the transient load carrying adaptability of the slipper lubricating film, both of which are essential to the underlying slipper operation. However, these assumptions were necessary to formulate closed form analytical solutions, but by introducing numerical methods, the partial differential equations can be solved directly.

The fluid-structure-thermal model of slipper swashplate lubrication developed in this chapter will use the coordinate systems, kinematical analysis and free body diagrams developed in the previous sections 2.1 through 2.3. However, analysis of the fluid film pressure will no longer use the simplified algebraic expression of Eq. (2.16). The next section expands on the phenomena which are now considered to impact the lubricating fluid film pressure and thus overall slipper lubrication performance.

3.1 Slipper-swashplate Lubrication Phenomena and Model Overview

The primary unknown in establishing slipper-swashplate lubrication performance is the fluid film thickness between the slipper and swashplate. Once the fluid film thickness is established, the Reynolds equation, a governing equation for the thin viscous fluid film regime, can solve for the non-uniform pressure distribution. From this pressure distribution, other derived quantities such as leakage, friction forces, and power losses can be calculated with a high degree of confidence. The value of fluid thickness is the sum of a number of individual sources: the micro-rigid body separation of the slipper from the swashplate, the relative deformation due to pressure of the slipper and swashplate, and the relative thermal deformation of the slipper body.

The rigid body separation of the slipper from the swashplate is a transient problem as it depends on the instantaneous load pressing the slipper to the swashplate. This separation is defined by three degrees of freedom: the normal distance (z) of the slipper body from the swashplate running face, and the two planer inclinations (Rx, Ry) of the slipper sealing land from the swashplate running face illustrated in Figure 3.1.

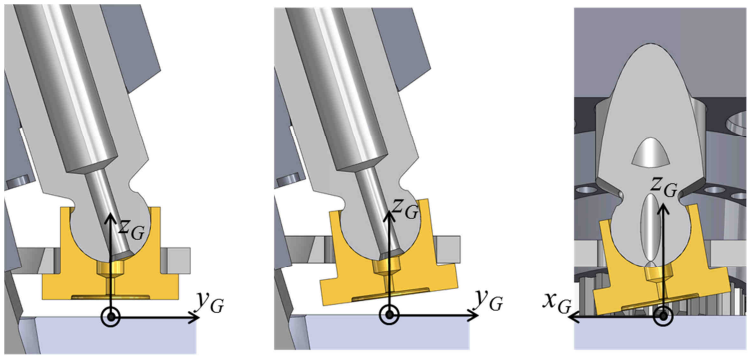

Figure 3.1. Exaggerated slipper micro-motion.

The translational and rotational velocities for these three degrees of freedom are found by satisfying Eq. (3.1) with the forces and moments defined in Section 2.3.

$$\begin{cases} F_{fz} - F_{SK} - F_{HD} = ma_z \\ M_{fx} + M_{\omega x} = I_x \alpha_x \\ M_{fy} + M_{TG} = I_y \alpha_y \end{cases} \tag{3.1}$$

Since the mass and inertial tensor of the slipper is small, the right hand side of Eq. (3.1) can be neglected simplifying the slipper force balance to:

$$\begin{cases} F_{fz} - F_{SK} - F_{HD} = 0 \\ M_{fx} + M_{\omega x} = 0 \\ M_{fy} + M_{TG} = 0 \end{cases} \tag{3.2}$$

Although slipper velocity terms do not directly appear in Eq. (3.2), the fluid pressure, and thus resulting force and moments, strongly depend on the separational velocities, termed the fluid film squeeze velocity or micro-motion. While these micro slipper dynamics are transient over a shaft revolution, the aim of this model is to solve for slipper operation during steady state machine operation. An advantage of this assumption is that at steady state the slipper micro motion is periodically repeating each revolution. Due to this periodicity, the entire rotating kit of slippers does not need to be simulated. Instead only an individual slipper is simulated for a few revolutions until it reaches steady state. These individual results can then be offset appropriately and combined to obtain equivalent results from the entire set of slippers.

The other contributions to fluid film thickness, pressure deformation of the slipper and swashplate, and thermal deformation of the slipper body, are solved using the elasticity equation for a solid body. The interaction between pressure deformation and the resulting

lubricating pressure field can be strongly coupled especially when the film thickness is below a few microns, and this interaction is termed a fluid structure interaction (FSI) problem. The partitioned approach is used to solve for the fluid structure interaction whereby the fluid and solid domain are solved separately using their respective governing equations, with natural / essential boundary conditions are being iteratively updated at the FSI interface until a converged solution is found.

In thin lubricating films, significant heat generation can result from viscous shearing of the fluid. This heat generation warms the lubricant which for many lubricating fluids can significantly alter the dynamic viscosity, affecting the hydrodynamic pressure generation ability of the fluid film. The convective-diffusive equation is used to solve for the three-dimensional heat distribution of the lubricating film, and an empirically derived exponential model compares fluid temperature to viscosity. Because the fluid film is so thin, significant heat is transferred by conduction into the slipper and swashplate. The diffusive heat transfer equation solves for the steady-state temperature distribution in the slipper and swashplate bodies. Additionally, especially with bi-metal slipper designs, the non-uniform heat distribution of the slipper body causes a thermal expansion and this thermal deformation is solved for using the elasticity equation and included into the slipper film thickness calculation.

Although the lubricating fluid film is bounded by the slipper on top and the swashplate on bottom, regions of fluid both radially inwards and outwards bound the thin film to ensure the lubricating zone remains fully flooded. Moreover, these fluid boundaries provide the hydrostatic component of the lubricating pressure. The outer boundary is the pump case or housing fluid volume, and has a constant pressure of typically 1-3 bar. The

inner radius of the thin fluid film is bounded by the slipper pocket fluid volume. This small volume of fluid has a variable pressure which is modeled using a lumped parameter approach, assuming that the same pressure is uniform throughout the pocket volume. The compressible continuity equation solves for the change in pocket pressure with respect to time, considering the balance of flow in from the displacement chamber, flow out through the lubricating gap, and the change in the pocket volume over time.

Before considering how these multi-domain segregated numerical models and their respective effects are coupled together novelly in this work, each of these separate underlying models will be described in detail.

3.2 Thin-film Fluid Pressure Model

Sufficient analytical approximations were developed in section 2.3 for all of the forces acting on the slipper except for the slipper fluid pressure force. This fluid force needs to be found instead by integrating fluid pressure over the thin fluid film domain. This domain is bounded on top by the slipper and on the bottom by the swashplate. In practically all pump designs, the slipper will never overhang the swashplate face. Thus, it is the slipper geometry which determines the bounds of the thin fluid film lubricating regime. On the underside of a typical slipper there exist two distinct regions of hydraulic fluid: a fluid pocket, and the thin lubricating fluid film. The slipper pocket is typically 0.7-1.0 mm tall and thus a constant and uniform fluid pressure is assumed in the pocket region. Fluid in the pocket is fed from the displacement chamber through a drilling in the piston and slipper. Pressure in the displacement chamber is a boundary condition to this numerical model and is solved using a lumped parameter model before lubrication simulation. The slipper sealing land is the portion of the slipper geometry which defines

the domain of the thin fluid film. The pocket and sealing lands are illustrated on the left of Figure 3.2. A more complicated slipper design introduces two vented stabilizing lands in addition to the primary sealing land. In this vented multi-land slipper design, the new inner stabilizing land is surrounded by pocket pressure while the outer stabilizing land is surrounded by case pressure as illustrated on the right of Figure 3.2.

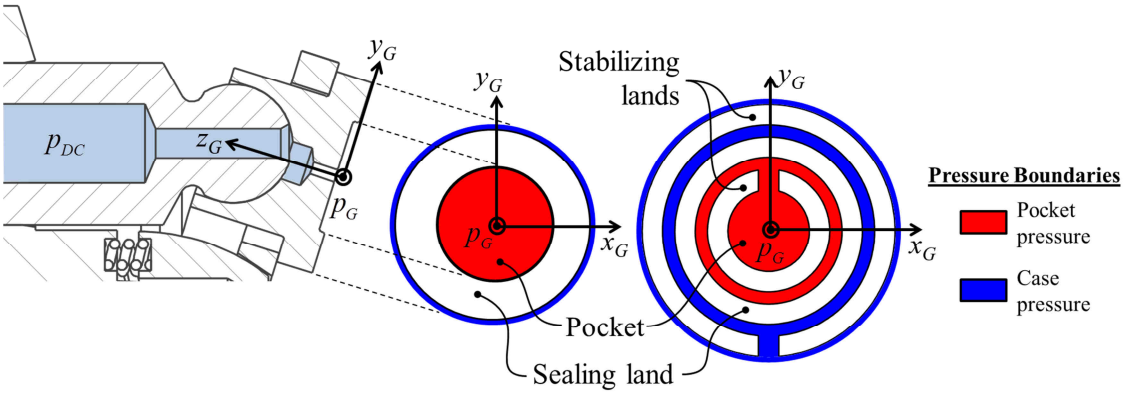

Figure 3.2. Slipper pressure boundaries for a single land (left) and vented multi-land (right) designs.

Regardless of slipper land design, within the sealing/stabilizing land region, due to the thin nature of the lubricant domain, the fluid pressure distribution can be found using the Reynolds equation. The Reynolds equation, or lubrication equation, is a fundamental equation of tribology (Reynolds, 1886). First derived by Reynolds Osborn in 1886, the Reynolds equation predicts the pressure distribution in a thin film of viscous fluid accounting for different sources of pressure generation. The pressure solution of the Reynolds equation does depend strongly on the fluid film thickness, which as described in section 3.1 is a summation of multiple sources. However, by utilizing an initial guess and then iterating, an accurate calculation of the fluid film thickness can be used.

Although the Reynolds equation is widely derived, the typical derivation incorporates a number of bounding surface height gradient or velocity assumptions limiting the applicability of the final equation. The following derivation will not impose such limitations and moreover, by maximizing use of differential operators, coordinate system independence can be maintained.

3.2.1 Analytical Derivation of the Reynolds Equation

The Reynolds equation originates from the three dimensional Navier Stokes equation for incompressible flow, written here using vector operators:

$$\rho\frac{\partial \mathbf{v}}{dt}+\rho\mathbf{v}\cdot\nabla\mathbf{v}=-\nabla p+\nabla\cdot\left(\mu\nabla\mathbf{v}\right)+\mathbf{f} \tag{3.3}$$

Lubrication theory makes assumptions regarding fluid behavior in the thin film regime:

1. Fluid inertial forces are small when compared to the viscous forces, and thus the convective acceleration term $\rho\mathbf{v}\cdot\nabla\mathbf{v}$ is neglected.
2. Fluid acceleration is small, implying near-steady state operation, thus $\rho\frac{\partial \mathbf{v}}{dt}\approx 0$.
3. Body forces of the fluid are negligible.
4. Pressure is assumed constant across the fluid film thickness, therefore $\frac{\partial p}{dz}=0$ and p is a function of x and y only. Similarly, fluid viscosity and density are assumed constant across the fluid film.

5. Spatial derivatives of fluid velocity in the fluid film plane are small when compared to the fluid velocity derivative across the fluid film such that $\frac{\partial \mathbf{v}}{\partial z} \gg \frac{\partial \mathbf{v}}{\partial x}$ and $\frac{\partial \mathbf{v}}{\partial z} \gg \frac{\partial \mathbf{v}}{\partial y}$.

The first three assumptions regarding fluid behavior in the lubricating regime allow Eq. (3.3) to be reduced to:

$$\nabla p = \nabla \cdot (\mu \nabla \mathbf{v}) \tag{3.4}$$

Because the lubrication area between the swashplate is ring-shaped, a cylindrical coordinate system is the most convenient to use for an accurate discretization of the lubrication domain. As part of the Reynolds equation derivation, an infinitely small wedge of fluid in the cylindrical coordinate system is considered with fluid film thickness and boundary velocities as illustrated in Figure 3.3.

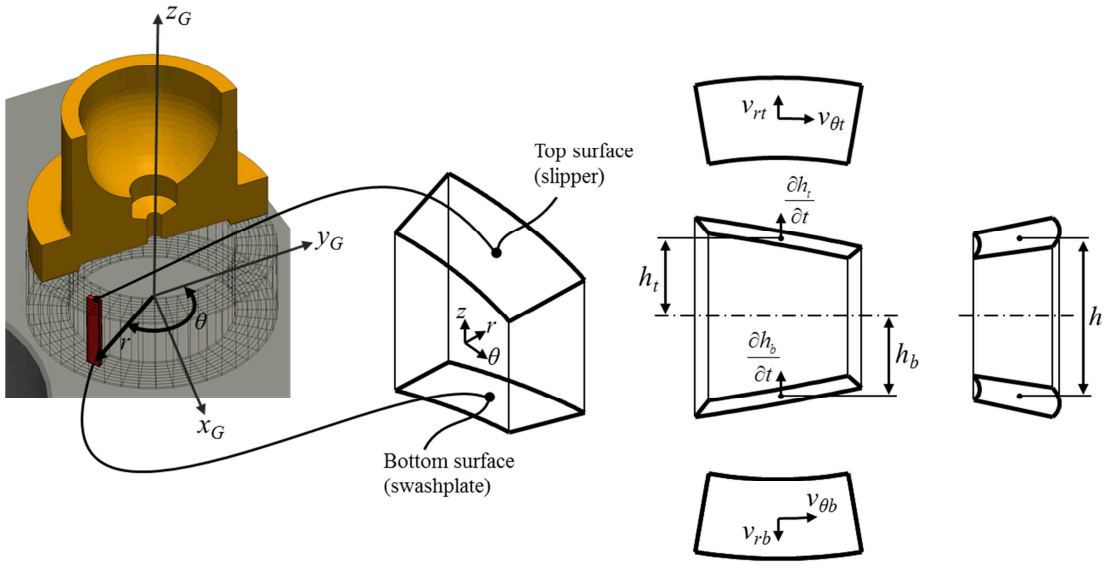

Figure 3.3. Representative parcel of lubricating fluid and cylindrical coordinate system definition.

In a cylindrical coordinate system, the ∇p term of Eq. (3.4) expands to:

$$\nabla p = \begin{cases} \dfrac{\partial p}{dr} \\ \dfrac{1}{r}\dfrac{\partial p}{d\theta} \\ 0 \end{cases} \tag{3.5}$$

where the z component of the gradient is 0 due to assumption 4 listed above. The final assumption 5 is used in the expansion of the right hand side of Eq. (3.4) which when combined with Eq. (3.5) is:

$$\begin{cases} \dfrac{\partial p}{dr} = \dfrac{\partial}{\partial z}\left(\mu \dfrac{\partial u}{\partial z}\right) \\ \dfrac{1}{r}\dfrac{\partial p}{d\theta} = \dfrac{\partial}{\partial z}\left(\mu \dfrac{\partial v}{\partial z}\right) \end{cases} \tag{3.6}$$

where u and v are fluid velocities in the r and θ components respectively.

Integrating Eq. (3.6) over the fluid film thickness and solving for the fluid velocities:

$$\iint \begin{matrix} \dfrac{\partial p}{dr} = \dfrac{\partial}{\partial z}\left(\mu \dfrac{\partial u}{\partial z}\right) \\ \dfrac{1}{r}\dfrac{\partial p}{d\theta} = \dfrac{\partial}{\partial z}\left(\mu \dfrac{\partial v}{\partial z}\right) \end{matrix} dzdz \Rightarrow \begin{cases} u = \dfrac{z^2}{2\mu}\dfrac{\partial p}{dr} + A_u \dfrac{z}{\mu} + B_u \\ v = \dfrac{z^2}{2\mu r}\dfrac{\partial p}{d\theta} + A_v \dfrac{z}{\mu} + B_v \end{cases} \tag{3.7}$$

where A and B are constants of integration. It is helpful to recast Eq. (3.7) in vector notation before continuing:

$$\mathbf{v} = \frac{z^2}{2\mu}\nabla p + \mathbf{A}\frac{z}{\mu} + \mathbf{B} \tag{3.8}$$

Referring to Figure 3.3, a given point p in the fluid is bounded by surface velocities $\mathbf{v}_t$ at $\mathrm{z} = h_t$ and $\mathbf{v}_b$ at $\mathrm{z} = h_b$. Using these boundary conditions **A** and **B** in Eq. (3.8) can be solved for their particular solution:

$$\mathbf{A} = -\frac{1}{2}\nabla p\left(h_t + h_b\right) + \mu\frac{\mathbf{v}_t - \mathbf{v}_b}{h_t - h_b}$$
$$\mathbf{B} = \frac{1}{2\mu}\nabla p\left(h_t \cdot h_b\right) + \frac{\mathbf{v}_b h_t - \mathbf{v}_t h_b}{h_t - h_b} \tag{3.9}$$

Substituting Eq. (3.9) in Eq. (3.8) and rearranging, an expression for fluid velocities in the thin film is obtained:

$$\mathbf{v} = \frac{1}{2\mu}\left(z^2 - \left(h_t + h_b\right)z + h_t h_b\right)\nabla p + z\left(\frac{\mathbf{v}_t - \mathbf{v}_b}{h_t - h_b}\right) + \frac{\mathbf{v}_b h_t - \mathbf{v}_t h_b}{h_t - h_b} \tag{3.10}$$

The fluid velocity field must satisfy a conservation of mass described by the continuity equation:

$$\frac{\partial \rho}{\partial t} + \nabla \cdot \left(\rho \mathbf{v}\right) = 0 \tag{3.11}$$

Since fluid velocity in the direction across the fluid film is neglected, Eq. (3.11) is integrated across the film thickness, in effect averaging the continuity equation over the lubricant height (Szeri, 2011):

$$\frac{\partial}{\partial t}\int_{h_b}^{h_t} \rho dz + \int_{h_b}^{h_t} \nabla \cdot \left(\rho \mathbf{v}\right) dz = 0 \tag{3.12}$$

Recalling the general form of the Leibniz integral rule:

$$\frac{d}{dx}\left(\int_{a(x)}^{b(x)} f\left(x, y\right) dy\right) = f\left(x, b(x)\right)\frac{d}{dx}\left(b(x)\right) - f\left(x, \mathrm{a}(x)\right)\frac{d}{dx}\left(\mathrm{a}(x)\right) + \int_{a(x)}^{b(x)} \frac{d}{dx}\left(f\left(x, y\right)\right) dy \tag{3.13}$$

allows Eq. (3.12) to be rewritten as:

$$\frac{\partial}{\partial t}\int_{h_b}^{h_t} \rho dz + \nabla \cdot \int_{h_b}^{h_t} \rho \mathbf{v} dz + \rho \mathbf{v}_b \cdot \nabla h_b - \rho \mathbf{v}_t \cdot \nabla h_t = 0 \tag{3.14}$$

The second integral in Eq. (3.14) becomes:

$$\int_{h_b}^{h_t} \rho \mathbf{v} dz = \frac{\rho}{2\mu}\left(\frac{1}{3}\left(h_t^{\,3} - h_b^{\,3}\right) - \frac{1}{2}\left(h_t + h_b\right)\left(h_t^{\,2} - h_b^{\,2}\right) + h_t h_b\left(h_t - h_b\right)\right)\nabla p + \frac{\rho}{2}\left(h_t^{\,2} - h_b^{\,2}\right)\left(\frac{\mathbf{v}_t - \mathbf{v}_b}{h_t - h_b}\right) + \rho\left(h_t - h_b\right)\left(\frac{\mathbf{v}_b h_t - \mathbf{v}_t h_b}{h_t - h_b}\right) \tag{3.15}$$

Recalling that $h = h_t - h_b$ and simplifying:

$$\int_{h_b}^{h_t} \rho \mathbf{v} dz = -\frac{\rho h^3}{12\mu}\nabla p + \frac{\rho h}{2}\left(\mathbf{v}_t + \mathbf{v}_b\right) \tag{3.16}$$

Evaluating the first integral in Eq. (3.14) and utilizing the integration from Eq. (3.16):

$$\nabla \cdot \left(-\frac{\rho h^3}{12\mu}\nabla p\right) + \nabla \cdot \left(\frac{\rho h}{2}\left(\mathbf{v}_t + \mathbf{v}_b\right)\right) + \rho \mathbf{v}_b \cdot \nabla h_b - \rho \mathbf{v}_t \cdot \nabla h_t + \frac{\partial}{\partial t}\left(\rho h\right) = 0 \tag{3.17}$$

Equation (3.17) is the vector form of the Reynolds equation valid for any gradient and velocity of top and bottom surfaces. The first term in the Reynolds equation represents the hydrostatic diffusion of pressure throughout the fluid film, while the remaining terms account for hydrodynamic sources of pressure generation. An advantage of the vector form of Eq. (3.17) is that it is independent of a particular coordinate system. As mentioned previously, because the cylindrical coordinate system is being used in this work to model the fluid film, the divergence and gradient operators are defined as:

$$\nabla \cdot \mathbf{A} = \frac{1}{r}\frac{\partial}{\partial r}\left(r\mathbf{A}_r\right) + \frac{1}{r}\frac{\partial}{\partial \theta}\left(\mathbf{A}_\theta\right) + \frac{\partial}{\partial z}\left(\mathbf{A}_z\right)$$
$$\nabla a = \left\langle \frac{\partial a}{\partial r}, \frac{1}{r}\frac{\partial a}{\partial \theta}, \frac{\partial a}{\partial z} \right\rangle \tag{3.18}$$

If the variation of fluid density, ρ, along the fluid film is neglected, the Reynolds equation in cylindrical coordinates becomes:

$$\frac{-1}{12r}\left(\frac{\partial}{\partial r}\left(\frac{rh^3}{\mu}\frac{\partial p}{\partial r}\right)+\frac{\partial}{\partial \theta}\left(\frac{h^3}{\mu r}\frac{\partial p}{\partial \theta}\right)\right)+\frac{h\left(v_{rt}+v_{rb}\right)}{2r}+\frac{\partial h}{\partial r}\left(\frac{v_{rt}+v_{rb}}{2}\right)$$
$$+h\frac{\partial}{\partial r}\left(\frac{v_{rt}+v_{rb}}{2}\right)+\frac{1}{r}\frac{\partial h}{\partial \theta}\left(\frac{v_{\theta t}+v_{\theta b}}{2}\right)+\frac{h}{r}\frac{\partial}{\partial \theta}\left(\frac{v_{\theta t}+v_{\theta b}}{2}\right) \tag{3.19}$$
$$-v_{rt}\frac{\partial h_t}{\partial r}-\frac{v_{\theta t}}{r}\frac{\partial h_t}{\partial \theta}+v_{rb}\frac{\partial h_b}{\partial r}+\frac{v_{\theta b}}{r}\frac{\partial h_b}{\partial \theta}+\frac{\partial h_t}{\partial t}-\frac{\partial h_b}{\partial t}=0$$

This is the form of the Reynolds equation which will be used to solve for the pressure distribution between the slipper and swashplate in the slipper land region(s). Note that spatial gradients of velocity which are often negligible in many tribological problems need to be considered in this case. The non-zero gradients arise not from surface stretching but due to describing a rectilinear velocity field on the polar slipper fluid coordinate system (Beschorner, 2009).

3.2.2 Finite Volume Discretization of the Reynolds Equation

The Reynolds equation as described by Eq. (3.19) does not possess an analytical solution and thus must be solved numerically. As with many distributed parameter numerical solutions, the domain of interest must be discretized into a finite number of points which will approximate the continuous field solution of the partial differential equation. Because of the naturally curved nature of the slipper domain, a polar coordinate system is used to describe the discretization. A structured grid is defined using inner and outer radius dimensions as well as a radial and circumferential cell count. An example of such a discretization is illustrated in Figure 3.4, along with the local slipper cylindrical coordinate system as defined in Figure 2.7. A typical polar discretization count used as part of this work would be 60 cells radially and 180 cells circumferentially.

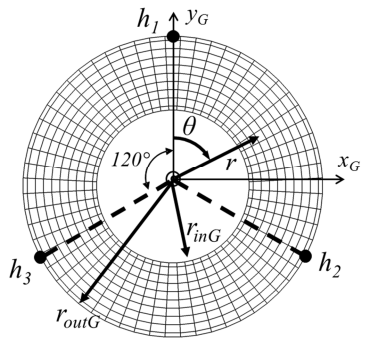

Figure 3.4. Two dimensional lubricating fluid grid.

A number of grid based finite schemes exist to solve partial differential equations like the Reynolds equation. Three popular schemes are: finite difference, finite volume, and finite element methods. The finite volume method is used due to its popularity in the computational fluid dynamics community.

The finite volume method works by creating discrete linearized equations which relate the pressure of a particular volume to its neighbor volumes. When sufficient boundary conditions are imposed a system of linear equations results with the solution yielding the discrete pressure field.

To begin, an individual cell with centroid *P* is selected as lightly shaded in the illustration of Figure 3.5. The cell has a height of Δr and an angular width of $\Delta \theta$. In the finite volume scheme, nodes are located at the centroid of each cell. Neighbor cells are located to the north, south, west, and east with centroids labeled *N*, *S*, *W*, and *E* respectively. The four faces separating the center cell from its neighbors are labeled *n*, *s*, *w* and *e* as illustrated in Figure 3.5.

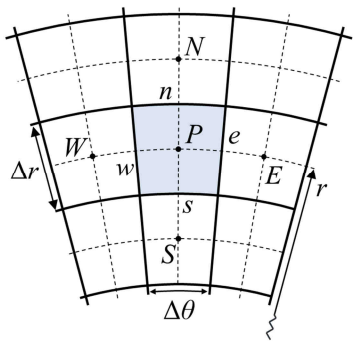

Figure 3.5. Polar two-dimensional fluid grid stencil.

A slightly modified notation of Eq. (3.19) is integrated over the two-dimensional volume of the cell:

$$\begin{aligned}\int_{\Omega}\nabla\cdot\left(\frac{h^3}{\mu}\nabla p\right)d\Omega = 12\int_{\Omega}\Bigg(&\frac{h\left(v_{rt}+v_{rb}\right)}{2r}+\frac{\partial h}{\partial r}\left(\frac{v_{rt}+v_{rb}}{2}\right)\\&+h\frac{\partial}{\partial r}\left(\frac{v_{rt}+v_{rb}}{2}\right)+\frac{1}{r}\frac{\partial h}{\partial\theta}\left(\frac{v_{\theta t}+v_{\theta b}}{2}\right)+\frac{h}{r}\frac{\partial}{\partial\theta}\left(\frac{v_{\theta t}+v_{\theta b}}{2}\right)\\&-v_{rt}\frac{\partial h_t}{\partial r}-\frac{v_{\theta t}}{r}\frac{\partial h_t}{\partial\theta}+v_{rb}\frac{\partial h_b}{\partial r}+\frac{v_{\theta b}}{r}\frac{\partial h_b}{\partial\theta}+\frac{\partial h_t}{\partial t}-\frac{\partial h_b}{\partial t}\Bigg)d\Omega\end{aligned} \tag{3.20}$$

Using the divergence theorem, the left hand side of Eq. (3.20) can be rewritten as an integral over the cell edges:

$$\int_{\Omega}\nabla\cdot\left(\frac{h^3}{\mu}\nabla p\right)d\Omega = \int_{A}\frac{h^3}{\mu}\nabla p\cdot d\mathbf{A} \tag{3.21}$$

where **A** is the cell face area normal. An important assumption is then imposed in this particular finite volume discretization: variables may vary at most linearly between each cell centroid. In other words, this restriction means a continuous variable over the whole lubricating domain is approximated in a piecewise linear fashion with cell centroids as vertices. As the limit of the finite volume size approaches zero, the piecewise linear function will exactly represent the true continuous variable. Additionally, because the

finite volume mesh is structured, the cell face area normals only have a single non-zero component simplifying the vector dot product of Eq. (3.21). Using these properties, the edge integral of Eq. (3.21) is decomposed into the four cell faces of Figure 3.5. The pressure gradient is expanded according to Eq. (3.18), and using the finite volume linear variation assumption, the edge integral is evaluated at the centroid of each edge:

$$\begin{aligned}\int_A \frac{h^3}{\mu}\nabla p \cdot d\mathbf{A} = &\frac{h_e^{\,3}}{\mu_e}\frac{\partial p_e}{r\partial\theta}\Delta r - \frac{h_w^{\,3}}{\mu_w}\frac{\partial p_w}{r\partial\theta}\Delta r \\ &+ \frac{h_n^{\,3}}{\mu_n}\frac{\partial p_n}{\partial r}\nabla p_n\left(r+\frac{\Delta r}{2}\right)\Delta\theta - \frac{h_s^{\,3}}{\mu_s}\frac{\partial p_s}{\partial r}\left(r-\frac{\Delta r}{2}\right)\Delta\theta\end{aligned} \tag{3.22}$$

Again, because the finite volume mesh is structured the cell centroids are located such that the connection between each neighbor is exactly orthogonal to the shared cell face. This means the face pressure differentials of Eq. (3.22) can easily be represented discretely as:

$$\frac{\partial p_e}{r\partial\theta} = \frac{p_E - p_P}{r\Delta\theta}, \quad \frac{\partial p_w}{r\partial\theta} = \frac{p_P - p_W}{r\Delta\theta}, \quad \frac{\partial p_n}{\partial r} = \frac{p_N - p_P}{\Delta r}, \quad \frac{\partial p_s}{\partial r} = \frac{p_P - p_S}{\Delta r} \tag{3.23}$$

Similarly, again because of the linear variable profile assumption between cell centroids, face height and viscosity values can be calculated as an average of nodal values:

$$\phi_e = \frac{\phi_E + \phi_P}{2}, \quad \phi_w = \frac{\phi_W + \phi_P}{2} \quad \phi_n = \frac{\phi_N + \phi_P}{2} \quad \phi_s = \frac{\phi_S + \phi_P}{2} \tag{3.24}$$

where ϕ represents fluid film thickness, viscosity, or any other continuous scalar variable over the fluid film domain. The two-dimensional volume integral on the right hand side of Eq. (3.20) can be evaluated numerically thanks to the linear profile assumption of the finite volume method:

$$12\int_{\Omega}\left(\begin{array}{l}\dfrac{h\left(v_{rt}+v_{rb}\right)}{2r}+\dfrac{\partial h}{\partial r}\left(\dfrac{v_{rt}+v_{rb}}{2}\right)+h\dfrac{\partial}{\partial r}\left(\dfrac{v_{rt}+v_{rb}}{2}\right)\\ +\dfrac{1}{r}\dfrac{\partial h}{\partial\theta}\left(\dfrac{v_{\theta t}+v_{\theta b}}{2}\right)+\dfrac{h}{r}\dfrac{\partial}{\partial\theta}\left(\dfrac{v_{\theta t}+v_{\theta b}}{2}\right)-v_{rt}\dfrac{\partial h_t}{\partial r}\\ -\dfrac{v_{\theta t}}{r}\dfrac{\partial h_t}{\partial\theta}+v_{rb}\dfrac{\partial h_b}{\partial r}+\dfrac{v_{\theta b}}{r}\dfrac{\partial h_b}{\partial\theta}+v_{zt}-v_{zb}\end{array}\right)d\Omega$$

$$=12\left[\begin{array}{l}\dfrac{h_P\left(v_{rt}+v_{rb}\right)_P}{2r}+\dfrac{\partial h_P}{\partial r}\left(\dfrac{v_{rt}+v_{rb}}{2}\right)_P+h_P\dfrac{\partial}{\partial r}\left(\dfrac{v_{rt}+v_{rb}}{2}\right)_P\\ +\dfrac{1}{r}\dfrac{\partial h_P}{\partial\theta}\left(\dfrac{v_{\theta t}+v_{\theta b}}{2}\right)_P+\dfrac{h_P}{r}\dfrac{\partial}{\partial\theta}\left(\dfrac{v_{\theta t}+v_{\theta b}}{2}\right)_P-v_{rt_P}\dfrac{\partial h_{t_P}}{\partial r}\\ -\dfrac{v_{\theta t_P}}{r}\dfrac{\partial h_{t_P}}{\partial\theta}+v_{rb_P}\dfrac{\partial h_{b_P}}{\partial r}+\dfrac{v_{\theta b_P}}{r}\dfrac{\partial h_{b_P}}{\partial\theta}+\dfrac{\partial h_{t_P}}{\partial t}-\dfrac{\partial h_{b_P}}{\partial t}\end{array}\right]r\Delta\theta\Delta r \tag{3.25}$$

where all variables are evaluated at the cell centroid, and a simple differencing of the cell scalar face values are used to evaluate the cell centroid velocity and height gradients:

$$\frac{\partial\phi_P}{\partial\theta}=\frac{\phi_e-\phi_w}{\Delta\theta},\quad \frac{\partial\phi_P}{\partial r}=\frac{\phi_n-\phi_s}{\Delta r} \tag{3.26}$$

where face values are found using Eq. (3.24). Note this is effectively using a central difference method to find cell centroid derivatives.

The fully discretized form of Eqs. (3.22) and (3.25) are combined and the centroid pressures are factored from the left hand side resulting in a linear equation which describes the individual cell centroid pressure, p_P, as a function of the neighboring cell pressures and a constant source term:

$$a_P p_P - a_E p_E - a_W p_W - a_N p_N - a_S p_S = b \tag{3.27}$$

This discretization scheme as presented is undefined at the domain boundaries where a neighbor cell outside of the domain does not exist. To remedy this, cells located on a fluid domain boundary have an imposed pressure value. Because the neighbor cell

pressure is now fixed, the associated term on the left side of Eq. (3.27) can be numerically evaluated and added to the *b* term. An example of this for an individual cell with a north boundary would result in:

$$a_P p_P - a_E p_E - a_W p_W - a_S p_S = b + a_N p_N \tag{3.28}$$

The single land slipper design only has a radially inner and outer boundary of pocket and case pressure respectively as illustrated on the left of Figure 3.2. The more complicated vented multi-land slipper design with boundary conditions shown on the right of Figure 3.2 is handled in a similar fashion. The circumferential grooves are defined using geometric dimensions allowing the finite volume mesh to exactly match the groove boundaries. The radial venting grooves instead are automatically defined using the slipper solid body definition used in section 3.6. Because this automatic method uses simple cell deactivation, the geometric discretization is less precise as illustrated in Figure 3.6.

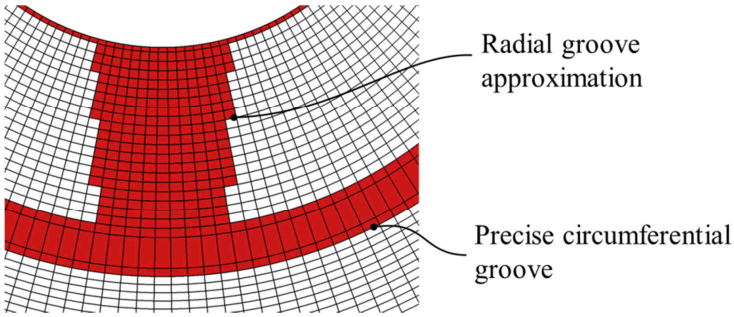

Figure 3.6. Multi-land slipper groove definitions.

The individual discrete Reynolds equations for each cell in the fluid domain are combined using matrix notation to form a linear system of equations:

$$\mathbf{Ap} = \mathbf{b} \tag{3.29}$$

The resulting system of linear equations from Eq. (3.29) is solved using an incomplete Cholesky preconditioned iterative bi-conjugant gradient stabilized solver as implemented in the GMM++ library (Renard, 2011).

3.2.3 Elastohydrodynamic Squeeze Pressure Generation

In the discretized Reynolds equation source term, Eq. (3.25), specific attention should be paid to the last two terms, $\frac{\partial h_{t_P}}{dt} - \frac{\partial h_{b_P}}{dt}$, which represent the normal, or squeeze velocity of the slipper and swashplate surfaces. As described in section 3.1, the total fluid film thickness is a summation of three sources: slipper rigid body micro-motion, pressure deformation of the slipper and swashplate, and thermal deformation of the slipper. Slipper rigid body micro-motion is traditionally considered as the only source of temporal change in fluid film thickness. The slipper micro velocity is varied by the solid body micro-motion model to achieve a fluid force balancing the external loads. Because the slipper thermal deformation is assumed constant over a shaft revolution, there is no thermal $\frac{\partial h_{t_P}}{dt}$ contribution.

The pressure deformation of the slipper and swashplate however does change during a shaft revolution in response to the varying pressure loads. The varying pressure deformation is in part from hydrodynamic sources, but especially large changes occur due to hydrostatic boundary pressure fluctuations. As the displacement chamber transitions from high to low pressure, the hydrostatic pressure within the slipper pocket changes by the same magnitude as well. These deformation magnitudes are non-negligible, often on the order of a few micrometers. Moreover, the time period over

which the changing deformation occurs is very short, only a few degrees of shaft rotation. To correctly account for the deformation squeeze pressure effect (Li and Kahraman, 2010), a backwards difference method is used:

$$\frac{\partial u_{slipper}}{dt} = \frac{u_t^{slipper} - u_{t-\Delta t}^{slipper}}{\Delta t}$$
$$\frac{\partial u_{swashplate}}{dt} = \frac{u_t^{swashplate} - u_{t-\Delta t}^{swashplate}}{\Delta t} \tag{3.30}$$

Using these finite difference approximations to the elastohydrodynamic contribution of squeeze pressure generation, the boundary velocities can be defined as:

$$\frac{\partial h_t}{\partial t} = \frac{\partial h_{rigid}}{\partial t} + \frac{\partial u_{slipper}}{dt}$$
$$\frac{\partial h_b}{\partial t} = \frac{\partial u_{swashplate}}{dt} \tag{3.31}$$

When calculating the finite difference approximations in Eq. (3.30), it is important that the same spatial location is used at both *t* and *t-Δt* as also emphasized by Chang (2000). Due to the moving lubricating fluid domain with respect to the stationary swashplate, a careful interpolation is required to maintain this consistency.

3.3 Slipper Pocket Pressure Model

The Reynolds equation solved for the pressure distribution within the lubricating film between the slipper and swashplate. The second fluid domain significantly contributing to the fluid force which acts on the slipper is the slipper pocket. This pocket is a small volume of fluid which is connected to the displacement chamber through a small orifice(s), and at the outer radius is nearly sealed by the slipper sealing land. Because the slipper pocket is typically 0.7-1.0 mm tall, it is reasonable to approximate the pressure in the slipper pocket as constant throughout the volume. The so called “pressure build-up

equation", which derives from the compressible continuity equation and the definition of bulk modulus, relates the time derivative of fluid pressure in a control volume to the net control volume flow as:

$$\frac{dp}{dt} = -\frac{K}{V}\left(\sum Q + \frac{dV}{dt}\right) \tag{3.32}$$

where K is the fluid bulk modulus, Q are the in/outlet flows, and V is the volume of the control volume. The control volume of the slipper pocket is illustrated in Figure 3.7. Inlet flow from the displacement chamber must pass through a restriction in the piston head, and then a second restriction in the slipper body itself. Since a lumped parameter approach is being used to model the pocket pressure, it is necessary to develop an equation which represents the pressure drop across these two restrictions as a function of the volumetric flow rate into the slipper.

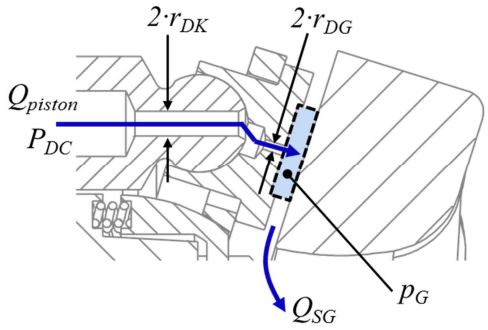

Figure 3.7. Slipper pocket control volume.

In a simple sense, the restrictions can either be considered as an orifice or a throttle depending on the laminar versus turbulent nature of the flow regime. In practice, especially for the slipper restriction, although the flow may often be laminar at low flow rates, due to the short length of the restrictions it does not achieve a fully developed flow field which is an assumption of the laminar throttle pressure drop model. Moreover,

because the restrictions become most important at higher volumetric flows, a turbulent model of pressure drop is assumed for both restrictions. The orifice equation which considers the pressure drop across the two restrictions relates pocket inlet flow to the differential pressure between the displacement chamber and pocket:

$$Q_{piston}(p_G) = \sqrt{\frac{2{\alpha_D}^2 \pi^4 r_{DG}^4 r_{DK}^4}{\rho\left(\pi^2 r_{DG}^4 + \pi^2 r_{DK}^4\right)}\left|p_{DC} - p_G\right|} \cdot sgn\left(p_{DC} - p_G\right) \tag{3.33}$$

Flow through the gap can be calculated by analytically integrating Eq. (3.10) over the film thickness dimension, z, from h_b to h_t and then numerically integrating around the slipper circumference at the inner sealing land radius:

$$Q_{SG} = \int_0^{2\pi}\left(-\frac{1}{12\mu}\frac{\partial p}{\partial r}h^3 - \frac{h}{2}v_{rt}\right) r d\theta \tag{3.34}$$

The time derivative of pocket pressure can now be written as:

$$\frac{dp_G}{dt} = \frac{K}{V_{pocket}}\left(Q_{piston} - Q_{SG} - \frac{dV_{pocket}}{dt}\right) \tag{3.35}$$

A simple first order Euler method can solve the ordinary differential equation of Eq. (3.35) for p_G at the present time given a p_G value at a previous time, Δt ago:

$$p_G = p_{G,t-1} + \Delta t \cdot \frac{dp_G}{dt} \tag{3.36}$$

Numerically, because the bulk modulus of fluid is quite high and the slipper pocket volume is quite small, Eq. (3.35) is exceptionally stiff. Formally, Eq. (3.36) is an implicit formulation because the differential is evaluated at the present timestep, but because this is accomplished explicitly in an iterative loop and due to the high equation stiffness, this method diverges. If the pressure differential Eq. (3.36) is expanded:

$$p_G = p_{G,t-1} + \Delta t \cdot \frac{K}{V_{pocket}} \begin{pmatrix} \sqrt{\frac{2\alpha_D{}^2 \pi^4 r_{DG}^4 r_{DK}^4}{\rho\left(\pi^2 r_{DG}^4 + \pi^2 r_{DK}^4\right)} \left| p_{DC} - p_G \right|} \cdot sgn\left(p_{DC} - p_G \right) \\ -Q_{SG} - \frac{dV_{pocket}}{dt} \end{pmatrix} \tag{3.37}$$

Although Q_{SG} and dV/dt must still be updated iteratively due to their numerical formulation, the p_G term from Q_{piston} would not need to be iterated if Eq. (3.37) is algebraically solved for p_G. Due to the presence of the absolute value and sgn function, a piecewise solution is obtained:

$$\begin{aligned} p_G &= \begin{cases} c_1 + \frac{1}{2} c_2 \left(-c_2 + \sqrt{c_2{}^2 + 4 p_{DC} - 4 c_1} \right) & c_1 \le p_{DC} \\ c_1 - \frac{1}{2} c_2 \left(-c_2 + \sqrt{c_2{}^2 - 4 p_{DC} + 4 c_1} \right) & c_1 > p_{DC} \end{cases} \\ &where: \\ c_1 &= p_{G,t-1} - \Delta t \cdot \frac{K}{V_{pocket}} \left(Q_{SG} + \frac{dV}{dt} \right) \\ c_2 &= \Delta t \cdot \frac{K}{V_{pocket}} \cdot \alpha_D \pi^2 r_{DG}^2 r_{DK}^2 \sqrt{\frac{2}{\rho\left(\pi^2 r_{DG}^4 + \pi^2 r_{DK}^4\right)}} \end{aligned} \tag{3.38}$$

This improved method achieves good stability although the pocket pressure is typically underrelaxed by ~0.5 to prevent oscillations due to the Q_{SG} coupling in the fluid-structure interaction and slipper micro-motion loops.

3.4 Slipper Rigid Body Micro-motion Model

By using the Reynolds equation to solve for the lubricating pressure distribution and the slipper pocket model to calculate the uniform pocket pressure, the net fluid force acting on the slipper is calculated using Eq. (2.13). However, the pressures predicted by both of these models depend strongly on fluid film thickness. As described in section 3.1, the

lubricating fluid film thickness is the summation of multiple sources, the first of which originates from the slipper micro-motion.

The macro motion of the slipper is governed by the main axial piston machine kinematics as defined in section 2.2. However, each individual slipper is able to self-adjust its own micro-motion in response to the varying external loads. There are three micro degrees of freedom for each slipper with respect to the local slipper coordinate system: a translation in the z-axis and a rotation about the x and y axes. These three micro degrees of freedom are illustrated in Figure 3.1.

Although possible to express the slipper micro-motion using the z-translation and x and y rotations, it is perhaps easier to define an equivalent motion using z-translation of three points affixed to the undeformed slipper running surface. One advantage of this definition is that like units are shared between each degree of freedom, instead of mixing displacement with rotation. These three control points, as illustrated in Figure 3.8, remain affixed to the local slipper coordinate system. They are defined at the outer slipper radius with point g_1 lying radially outwards on the y_g axis and the other two points being defined in a clockwise manner spaced 120° apart.

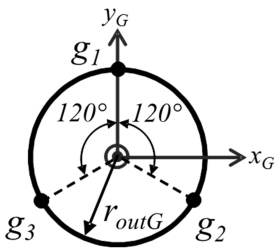

Figure 3.8. Slipper control points definition.

The fluid film height distribution resulting from a rigid body separation of the slipper from the swashplate in the local slipper cylindrical coordinate system (Figure 2.7) can be described using the height of the three control points at the outer diameter of the slipper:

$$h(r,\theta)=\frac{r}{r_{outG}}\cdot\sin(\theta)\sqrt{\frac{1}{3}}(h_2-h_3)+\frac{r\cdot\cos(\theta)}{3r_{outG}}(2h_1-h_2-h_3)+\frac{1}{3}(h_1+h_2+h_3) \quad (3.39)$$

Similarly, the normal velocity distribution over the slipper lands resulting from a rigid body motion of the slipper can be described using the normal velocity of the three control points:

$$\begin{aligned}\frac{\partial h_{rigid}}{\partial t}(r,\theta)=&\frac{r}{r_{outG}}\cdot\sin(\theta)\sqrt{\frac{1}{3}}\left(\frac{dh_2}{dt}-\frac{dh_3}{dt}\right)\\&+\frac{r\cdot\cos(\theta)}{3r_{outG}}\left(2\frac{dh_1}{dt}-\frac{dh_2}{dt}-\frac{dh_3}{dt}\right)+\frac{1}{3}\left(\frac{dh_1}{dt}+\frac{dh_2}{dt}+\frac{dh_3}{dt}\right)\end{aligned} \quad (3.40)$$

The micro-motion of the slipper is governed by Eq. (3.2) which represents the system of forces acting on the slipper body about the three micro-motion degrees of freedom. Although part velocity does not appear directly in Eq. (3.2), the normal squeeze term of the Reynolds equation, Eq. (3.19), contains a term, $\frac{\partial h_t}{\partial t}$, which is partially composed of the slipper rigid body micro-velocity as expressed in Eq. (3.31). When the slipper moves with micro-motion, this velocity has a significant impact on the hydrodynamic pressure generation of the lubricating film. As the pressure within the fluid film changes, the force balance of Eq. (3.2) quickly changes and in response the slipper will adjust its micro position to again achieve a force balance.

A root finding method, in this work Newton's method, is used to find a slipper micro-velocity which causes a fluid pressure force to balance external loads. Because a

numerical method is being used, it is helpful if all three degrees of freedom are similar in magnitude, and thus Eq. (3.2) is transformed from a net force and two net moments about the local coordinate system origin, into three net forces acting at the three control points by solving the simple linear system:

$$\begin{pmatrix} 1 & 1 & 1 \\ r_{outG} & \frac{-r_{outG}}{2} & \frac{-r_{outG}}{2} \\ 0 & \frac{-r_{outG}\sqrt{3}}{2} & \frac{r_{outG}\sqrt{3}}{2} \end{pmatrix} \begin{pmatrix} dF_{G1} \\ dF_{G2} \\ dF_{G3} \end{pmatrix} = \begin{pmatrix} F_{fz} - F_{SK} - F_{HD} \\ M_{fx} + M_{\omega x} \\ M_{fy} + M_{TG} \end{pmatrix} \tag{3.41}$$

To evaluate the convergence of Newton's method a single objective function consisting of the norm of the three control point new forces is formulated:

$$df = \sqrt{dF_{G1}{}^2 + dF_{G2}{}^2 + dF_{G3}{}^2} \tag{3.42}$$

and thus by definition, when $df = 0$, Eq. (3.2) will be satisfied.

A central difference method of slightly varying the $\frac{dh}{dt}$ of each control point is used to calculate the Jacobian matrix needed by Newton's method:

$$J = \begin{bmatrix} \frac{ddF_{G1}}{d\frac{dh_1}{dt}} & \frac{ddF_{G1}}{d\frac{dh_2}{dt}} & \frac{ddF_{G1}}{d\frac{dh_3}{dt}} \\ \frac{ddF_{G2}}{d\frac{dh_1}{dt}} & \frac{ddF_{G2}}{d\frac{dh_2}{dt}} & \frac{ddF_{G2}}{d\frac{dh_3}{dt}} \\ \frac{ddF_{G3}}{d\frac{dh_1}{dt}} & \frac{ddF_{G3}}{d\frac{dh_2}{dt}} & \frac{ddF_{G3}}{d\frac{dh_3}{dt}} \end{bmatrix} \tag{3.43}$$

For the current vector of control point velocities, Newton's method states that a new set of control point velocities which should bring the Eq. (3.2) closer to zero is:

$$\begin{pmatrix} \frac{dh_1}{dt} \\ \frac{dh_2}{dt} \\ \frac{dh_3}{dt} \end{pmatrix} = \begin{pmatrix} \frac{dh_1}{dt} \\ \frac{dh_2}{dt} \\ \frac{dh_3}{dt} \end{pmatrix} - \mathbf{J}^{-1} \begin{pmatrix} dF_{G1} \\ dF_{G2} \\ dF_{G3} \end{pmatrix} \tag{3.44}$$

This numerical loop iterates until the net force norm defined in Eq. (3.42) is within a few Newtons of zero.

Every time a new set of control point micro velocities is found, the control point heights are integrated using a second order Adams Moulton method:

$$\begin{aligned} h_{G1} &= h_{G1,t-\Delta t} + \frac{1}{2}\left(\frac{dh_{G1,t-\Delta t}}{dt} + \frac{dh_{G1,t}}{dt} \right)\Delta t \\ h_{G2} &= h_{G2,t-\Delta t} + \frac{1}{2}\left(\frac{dh_{G2,t-\Delta t}}{dt} + \frac{dh_{G2,t}}{dt} \right)\Delta t \\ h_{G3} &= h_{G3,t-\Delta t} + \frac{1}{2}\left(\frac{dh_{G3,t-\Delta t}}{dt} + \frac{dh_{G3,t}}{dt} \right)\Delta t \end{aligned} \tag{3.45}$$

As described in section 3.1, once a force balance between the external loads and the fluid film pressure has been found, the shaft angle and time are incremented until a periodic solution of fluid film thickness between each shaft revolution has been reached.

3.5 Lubricating Fluid Temperature and Viscosity Model

Although the pressure distribution within the slipper lubricating film depends strongly on the fluid film thickness, the ability of the interface to generate hydrodynamic pressure also strongly depends on the fluid viscosity. The viscosity of a typical mineral oil lubricant present between the slipper and swashplate will change with multiple orders of magnitude as fluid temperature changes. Thus to correctly estimate the value of dynamic viscosity in the lubrication fluid, the temperature distribution in the fluid film must be

modeled. A convection-diffusive heat transfer through the lubricating fluid is assumed and thus the convection-diffusion, or energy, equation is suitable to capture the temperature distribution. Heat capacitance, or transient effects, are neglected. The general form of the energy equation used as part of this work is:

$$\nabla \cdot \left(\rho c_p \mathbf{v} T \right) = \nabla \cdot \left(\lambda \nabla T \right) + \Phi_d \tag{3.46}$$

where the left hand term represents convective heat transfer, the first right hand term thermal conduction, and Φ_d represents heat generation due to viscous shearing of the thin fluid film. In polar coordinates Φ_d is:

$$\Phi_d = \left(\frac{\partial v_r}{\partial z} \right)^2 + \left(\frac{\partial v_\theta}{\partial z} \right)^2 + \frac{4}{3} \left(\frac{v_r}{r} \right)^2 + \left(\frac{v_\theta}{r} \right)^2 \tag{3.47}$$

Unlike the Reynolds equation which was reduced to a two-dimensional finite domain with a scalar height property, the energy equation is solved on a full three-dimensional domain. The fluid mesh of Figure 3.4 is simply extruded along the fluid film thickness. However, because the fluid film is by definition thin, thermal conduction between the fluid and bounding solid bodies is the primary mechanism of heat transfer. Thus when solving for a temperature distribution of the fluid film, the boundary constraint temperatures imposed strongly affect the temperature solution. To improve model accuracy, the diffusive heat transfer of the bounding solid bodies will also be solved for in a separate step. To couple the fluid temperature model to the solid body thermal model, the heat flux from the lubricating fluid to the solid body is time averaged over a shaft revolution. This heat flux is calculated as:

$$q_{swashplate} = -\lambda\left(\frac{\partial T}{dz}\right)_{z=0}$$
$$q_{slipper} = -\lambda\left(\frac{\partial T}{dz}\right)_{z=h} \tag{3.48}$$

Although the Reynolds equation as derived in section 3.2 assumes a constant viscosity across the film, a variation of fluid viscosity along the film may easily be considered using the solution of the temperature distribution from Eq. (3.46) and fluid pressure from Eq. (3.19). An empirically derived exponential model, such as that published by Roelands (1966), which accounts for variation of fluid viscosity as a function of pressure and temperature is used:

$$\mu = 10\wedge\left(G_0\frac{\left(1+{}^{p}\!/_{2000}\right)^{C2\cdot\log\left(1+{}^{t}\!/_{135}\right)+D_2}}{\left(1+{}^{t}\!/_{135}\right)^{S_0}}-1.2\right) \tag{3.49}$$

where G_0, C_2, D_2, and S_0 are empirically derived coefficients.

3.5.1 Finite Volume Discretization of the Energy Equation

Similar to the Reynolds equation, the energy equation is discretized using the finite volume method. Due to the additional third dimension, a single volume now has six neighbor cells located to the north, south, west, east, top, and bottom with centroids aptly named *N*, *S*, *W*, *E*, *T*, and *B* respectively. Equation (3.46) is integrated over the cell volume, and the divergence theorem is then applied to rewrite the volume integral of divergence as an area integral:

$$\int_{\Omega}\nabla\cdot\left(\rho c_p\mathbf{v}T\right)d\Omega = \int_{\Omega}\nabla\cdot\left(\lambda\nabla T\right)d\Omega + \int_{\Omega}\Phi_d d\Omega$$
$$\int_{A}\left(\rho c_p\mathbf{v}T\right)\cdot d\mathbf{A} = \int_{A}\left(\lambda\nabla T\right)\cdot d\mathbf{A} + \int_{\Omega}\Phi_d d\Omega \tag{3.50}$$

The discretization proceeds in a straight forward fashion assuming a linear variation of temperature between cell centroids for the right hand side of Eq. (3.50). Because the left hand side of Eq. (3.50) contains a fluid velocity term, it is improper to consider exclusively a diffusive variation of fluid temperature. Instead the power law scheme (Patankar, 1980) is used to account for the convective component of this term. Fluid velocities in the *z* direction (normal to the film thickness) are negligible compared to the velocities parallel to the film thickness, and thus the convective term for the cell top and bottom faces is assumed to be zero. Similar to the Reynolds equation, a single sparse linear system can be formed and the iterative successive over-relaxation method is used to solve the linear system for fluid film temperature.

3.6 Solid Body Elastic Deformation Model

It is not only the slipper rigid body micro-motion which impacts the fluid film thickness. Instead, elastic deformation of the slipper and swashplate themselves will occur due to both pressure and thermal loading. Although the magnitudes of these deformations may be on the micrometer scale, the thin nature of the lubricating film demands these deformations to be considered. The impact of these deformations on the fluid film thickness can significantly alter the hydrodynamic pressure generation and therefore the overall fluid force. A finite element implementation of the solid body elasticity equation (Zienkiewicz, 2005) will be used to solve for pressure and thermal displacements of the slipper and swashplate domains.

3.6.1 Varational Formulation of the Elasticity Equation

The strong form of the governing elasticity equation is commonly written as:

$$\nabla \cdot \boldsymbol{\sigma} + \mathbf{b} = 0 \tag{3.51}$$

where $\boldsymbol{\sigma}$ represents the infinitesimal stress tensor and $\mathbf{b}$ are body forces. Instead of attempting to solve the strong form of Eq. (3.51) directly, the elasticity equation is recast using the method of residuals into a weak form. The residual function for Eq. (3.51) is defined as:

$$G\left(\mathbf{u},\bar{\mathbf{u}}\right) = -\int_{\Omega} \bar{\mathbf{u}}\left(\nabla\cdot\left(\boldsymbol{\sigma}\right)+\mathbf{b}\right) d\Omega = 0 \tag{3.52}$$

where $\bar{\mathbf{u}}$ represents a weighting function. The fundamental lemma of calculus of variations states that if over the entire domain, Eq. (3.52) is satisfied for all second-order differentiable functions $\bar{\mathbf{u}}$, then $\nabla\cdot\left(\boldsymbol{\sigma}\right)+\mathbf{b}=0$ must be true.

Recalling the vector product rule and divergence theorem respectively:

$$\begin{aligned} \bar{\mathbf{u}}\nabla\cdot\boldsymbol{\sigma} &= -\boldsymbol{\sigma}\cdot\nabla\bar{\mathbf{u}} + \nabla\cdot\left(\boldsymbol{\sigma}\bar{\mathbf{u}}\right) \\ \int_{\Omega}\nabla\cdot\left(\boldsymbol{\sigma}\bar{\mathbf{u}}\right) d\Omega &= \int_{\Gamma}\boldsymbol{\sigma}\bar{\mathbf{u}}\cdot\mathbf{n}\, d\Gamma \end{aligned} \tag{3.53}$$

Equation (3.52) can be rewritten as:

$$\begin{aligned} G\left(\mathbf{u},\bar{\mathbf{u}}\right) &= -\int_{\Omega}\bar{\mathbf{u}}\nabla\cdot\boldsymbol{\sigma}\, d\Omega - \int_{\Omega}\bar{\mathbf{u}}^{\mathrm{T}}\mathbf{b}\, d\Omega = 0 \\ G\left(\mathbf{u},\bar{\mathbf{u}}\right) &= \int_{\Omega}\boldsymbol{\sigma}\cdot\nabla\bar{\mathbf{u}}\, d\Omega - \int_{\Omega}\nabla\cdot\left(\boldsymbol{\sigma}\bar{\mathbf{u}}\right) d\Omega - \int_{\Omega}\bar{\mathbf{u}}^{\mathrm{T}}\mathbf{b}\, d\Omega = 0 \\ G\left(\mathbf{u},\bar{\mathbf{u}}\right) &= \int_{\Omega}\boldsymbol{\sigma}\cdot\nabla\bar{\mathbf{u}}\, d\Omega - \int_{\Gamma}\bar{\mathbf{u}}^{\mathrm{T}}\boldsymbol{\sigma}\cdot\mathbf{n}\, d\Gamma - \int_{\Omega}\bar{\mathbf{u}}^{\mathrm{T}}\mathbf{b}\, d\Omega = 0 \end{aligned} \tag{3.54}$$

To continue towards a solution, some assumptions must be made regarding the underlying mechanics. First, if small displacements in the final solution are assumed, the Lagrangian-strain tensor can be linearized as:

$$\boldsymbol{\varepsilon} = \frac{1}{2}\left(\nabla\mathbf{u}+\nabla\mathbf{u}^{\mathrm{T}}\right) \tag{3.55}$$

where **u** is the solid body local deformation vector. Second, assuming the magnitude of solid body deformation will remain in the linear-elastic range, Hooke's law can be used to relate stress and strain as:

$$\boldsymbol{\sigma} = \frac{E\nu}{(1+\nu)(1-2\nu)}\,\mathrm{tr}(\boldsymbol{\varepsilon})\mathbf{I} + \frac{E}{1+\nu}\boldsymbol{\varepsilon}$$

$$\boldsymbol{\sigma} = \frac{E}{(1+\nu)(1-2\nu)}\begin{bmatrix} 1-\nu & \nu & \nu & 0 & 0 & 0 \\ \nu & 1-\nu & \nu & 0 & 0 & 0 \\ \nu & \nu & 1-\nu & 0 & 0 & 0 \\ 0 & 0 & 0 & \frac{1-2\nu}{2} & 0 & 0 \\ 0 & 0 & 0 & 0 & \frac{1-2\nu}{2} & 0 \\ 0 & 0 & 0 & 0 & 0 & \frac{1-2\nu}{2} \end{bmatrix} \begin{Bmatrix} \varepsilon_{xx} \\ \varepsilon_{yy} \\ \varepsilon_{zz} \\ 2\varepsilon_{xy} \\ 2\varepsilon_{yz} \\ 2\varepsilon_{zx} \end{Bmatrix} \tag{3.56}$$

$$\boldsymbol{\sigma} = \mathbf{D}\boldsymbol{\varepsilon}$$

where E and ν are the material elastic modulus and Poisson's ratio respectively. Making use of these two mechanical identities, Eq. (3.54) can become:

$$\begin{aligned} G(\mathbf{u},\bar{\mathbf{u}}) &= \int_{\Omega} \bar{\boldsymbol{\varepsilon}}^{\mathrm{T}}\boldsymbol{\sigma}\, d\Omega - \int_{\Gamma} \bar{\mathbf{u}}^{\mathrm{T}}\boldsymbol{\sigma}\cdot\mathbf{n}\, d\Gamma - \int_{\Omega} \bar{\mathbf{u}}^{\mathrm{T}}\mathbf{b}\, d\Omega = 0 \\ G(\mathbf{u},\bar{\mathbf{u}}) &= \int_{\Omega} \bar{\boldsymbol{\varepsilon}}^{\mathrm{T}}\mathbf{D}\boldsymbol{\varepsilon}\, d\Omega - \int_{\Gamma} \bar{\mathbf{u}}^{\mathrm{T}}\mathbf{t}\, d\Gamma - \int_{\Omega} \bar{\mathbf{u}}^{\mathrm{T}}\mathbf{b}\, d\Omega = 0 \end{aligned} \tag{3.57}$$

where $\mathbf{t} = \boldsymbol{\sigma}\cdot\mathbf{n}$ and **t** represents surface boundary tractions.

3.6.2 Galerkin Method of Weighted Residuals

The varational formulation of the elasticity equation makes no assumptions as to how the functions **u** and $\bar{\mathbf{u}}$ are defined and thus the problem is still infinite dimensional. The method of weighted residuals takes the varational formulation and approximates **u** as a weighted linear combination of pre-defined shapes often call shape or basis functions:

$$\mathbf{u} \cong \mathbf{a}^{\mathrm{T}}\mathbf{h} \tag{3.58}$$

where **h** are the basis functions and **a** are the weights. These basis functions need to satisfy essential boundary conditions (displacement constraints). The Bubnov-Galerkin method further assumes the set of basis functions used to approximate **u** should be the same basis functions to approximate $\bar{\mathbf{u}}$:

$$\bar{\mathbf{u}} \cong \bar{\mathbf{a}}^{\mathrm{T}}\mathbf{h} \tag{3.59}$$

The infinite dimensional problem of the varational formulation has now been reduced to a finite dimensional problem of size equal to the number of basis functions.

3.6.3 Finite Element Discretization of the Elasticity Equation

The Rayleigh–Ritz method can be used from here provided the basis functions, **h**, are defined over the entire volume domain, Ω. However, because of the complex solid domain of the slipper and swashplate, the finite element approximation is used instead. With this approximation, the solid domain is discretized into many individual finite elements and Eq. (3.54) with the approximation of Eqs. (3.58) and (3.59) are applied to each element volume individually. The summation of the weighted residual approximation over all the elements leads to a global solution approximation.

There are many different types of individual element shapes which can be used to discretize a solid domain. This work utilizes arguably the simplest 3-d element type, the four node linear tetrahedron. Figure 3.9 illustrates how the slipper domain is discretized into the sum of many individual tetrahedral shaped volumes.

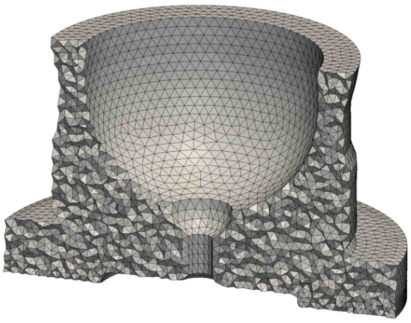

Figure 3.9. Slipper discretization with the linear tetrahedron.

Examining a single element with closer detail reveals four nodes, each with a coordinate in (*x*,*y*,*z*). These four nodes with a specified connectivity in turn define the four faces which comprise the tetrahedron as illustrated on the left of Figure 3.10. The four nodes are assumed not to be coplanar.

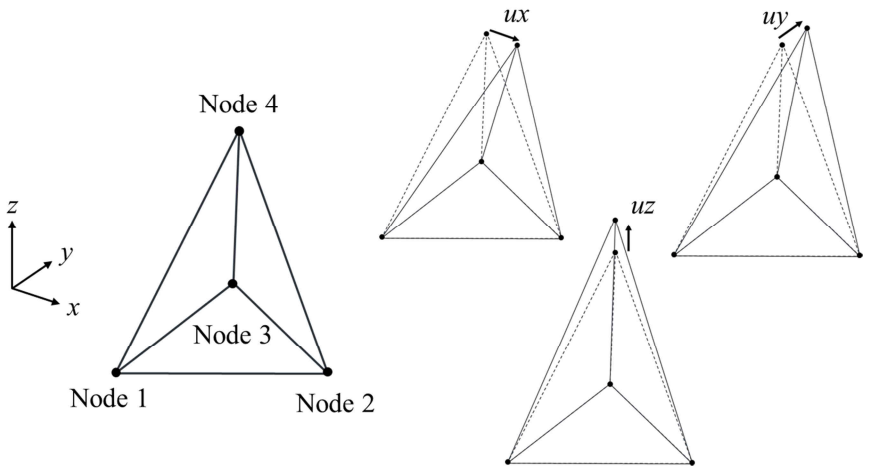

Figure 3.10. Four noded tetrahedron element and degrees of freedom for Node 4.

This four node element exhibits a total of twelve degrees of freedom in an elasticity analysis, three degrees of freedom corresponding to the (*x*,*y*,*z*) coordinates for each of the four nodes. These three degrees of freedom for Node 4 are illustrated on the right side of Figure 3.10.

Points within the volume of the tetrahedron can be defined using a linear interpolation of the four corner nodes. To facilitate this, it is helpful to describe the query point not in terms of its Cartesian coordinates, but rather in terms of the "natural" coordinates of the tetrahedron as partially illustrated in Figure 3.11. Four natural coordinates are defined for the tetrahedron, (*L1, L2, L3, L4*) with the coordinate value of (1, 0, 0, 0) when a point is coincident with Node 1, a coordinate value of (0, 1, 0, 0) when a point is coincident with Node 2, and so forth. A point would have a coordinate value of (0, L2, L3, L4) when the point lines in the plane of the face defined by Nodes 2-4.

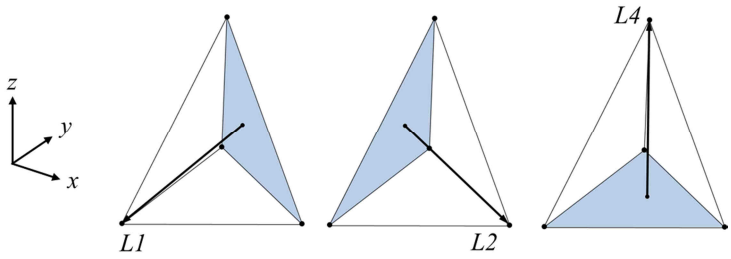

Figure 3.11. Tetrahedron natural coordinates.

Because the natural coordinate system is redundant in that four coordinates are used to describe a three dimensional space, a constraint is imposed whereby:

$$L1 + L2 + L3 + L4 = 1 \tag{3.60}$$

A point with natural coordinates (*L1, L2, L3, L4*) can be converted into Cartesian coordinates (x_p, y_p, z_p) with the following expression:

$$\begin{Bmatrix} 1 \\ x_p \\ y_p \\ z_p \end{Bmatrix} = \begin{bmatrix} 1 & 1 & 1 & 1 \\ x_1 & x_2 & x_3 & x_4 \\ y_1 & y_2 & y_3 & y_4 \\ z_1 & z_2 & z_3 & z_4 \end{bmatrix} \begin{Bmatrix} L1 \\ L2 \\ L3 \\ L4 \end{Bmatrix} \tag{3.61}$$

With this definition, the Cartesian space can now be expressed in terms of the local elemental nodal coordinates:

$$\begin{Bmatrix} N_1 \\ N_2 \\ N_3 \\ N_4 \end{Bmatrix} = \begin{bmatrix} 1 & 1 & 1 & 1 \\ x_1 & x_2 & x_3 & x_4 \\ y_1 & y_2 & y_3 & y_4 \\ z_1 & z_2 & z_3 & z_4 \end{bmatrix}^{-1} \begin{Bmatrix} 1 \\ x \\ y \\ z \end{Bmatrix} \tag{3.62}$$

These four functions N_1-N_4 are special and are termed the element shape functions. Because variations within the tetrahedral element are assumed to be linear, the displacement of a point with natural coordinates (*L1, L2, L3, L4*) can be expressed as a weighted summation of the displacement of the four nodes:

$$\mathbf{u}_p = \begin{bmatrix} u_{x1} & u_{x2} & u_{x3} & u_{x4} \\ u_{y1} & u_{y2} & u_{y3} & u_{y4} \\ u_{z1} & u_{z2} & u_{z3} & u_{z4} \end{bmatrix} \begin{Bmatrix} L1 \\ L2 \\ L3 \\ L4 \end{Bmatrix} \tag{3.63}$$

Or instead of writing the displacement of a specific point, the deformation field can be expressed in terms of the shape functions and a vector of nodal displacements:

$$\mathbf{u}(x,y,z) = \begin{bmatrix} N_1 & 0 & 0 & N_2 & 0 & 0 & N_3 & 0 & 0 & N_4 & 0 & 0 \\ 0 & N_1 & 0 & 0 & N_2 & 0 & 0 & N_3 & 0 & 0 & N_4 & 0 \\ 0 & 0 & N_1 & 0 & 0 & N_2 & 0 & 0 & N_3 & 0 & 0 & N_4 \end{bmatrix} \begin{Bmatrix} u_{x1} \\ u_{y1} \\ u_{z1} \\ u_{x2} \\ u_{y2} \\ u_{z2} \\ u_{x3} \\ u_{y3} \\ u_{z3} \\ u_{x4} \\ u_{y4} \\ u_{z4} \end{Bmatrix} \tag{3.64}$$

$$\mathbf{u}(x,y,z) = \mathbf{N}\mathbf{u}_\mathbf{e}$$

The deformation of the tetrahedral volume has now been written in terms of four orthogonal shape functions, N_1-N_4, and twelve scalar values of nodal component displacements. Recalling the Galerkin method of weighted residuals and Eq. (3.58), the deformation field was expressed as a discrete sum of basis functions and weights. This is exactly the same form in which Eq. (3.64) describes the deformation field in that the basis functions are the shape functions and the weights are the nodal displacements.

The strain field over the tetrahedral volume can be expressed discretely as the appropriate partial derivatives of the shape functions multiplied by the nodal displacement:

$$\boldsymbol{\varepsilon} = \mathbf{B}\mathbf{u}_e \tag{3.65}$$

where **B** is defined as:

$$\mathbf{B} = \begin{bmatrix} \frac{\partial N_1}{\partial x} & 0 & 0 & \frac{\partial N_2}{\partial x} & 0 & 0 & \frac{\partial N_3}{\partial x} & 0 & 0 & \frac{\partial N_4}{\partial x} & 0 & 0 \\ 0 & \frac{\partial N_1}{\partial y} & 0 & 0 & \frac{\partial N_2}{\partial y} & 0 & 0 & \frac{\partial N_3}{\partial y} & 0 & 0 & \frac{\partial N_4}{\partial y} & 0 \\ 0 & 0 & \frac{\partial N_1}{\partial z} & 0 & 0 & \frac{\partial N_2}{\partial z} & 0 & 0 & \frac{\partial N_3}{\partial z} & 0 & 0 & \frac{\partial N_4}{\partial z} \\ \frac{\partial N_1}{\partial y} & \frac{\partial N_1}{\partial x} & 0 & \frac{\partial N_2}{\partial y} & \frac{\partial N_2}{\partial x} & 0 & \frac{\partial N_3}{\partial y} & \frac{\partial N_3}{\partial x} & 0 & \frac{\partial N_4}{\partial y} & \frac{\partial N_4}{\partial x} & 0 \\ 0 & \frac{\partial N_1}{\partial z} & \frac{\partial N_1}{\partial y} & 0 & \frac{\partial N_2}{\partial z} & \frac{\partial N_2}{\partial y} & 0 & \frac{\partial N_3}{\partial z} & \frac{\partial N_3}{\partial y} & 0 & \frac{\partial N_4}{\partial z} & \frac{\partial N_4}{\partial y} \\ \frac{\partial N_1}{\partial z} & 0 & \frac{\partial N_1}{\partial x} & \frac{\partial N_2}{\partial z} & 0 & \frac{\partial N_2}{\partial x} & \frac{\partial N_3}{\partial z} & 0 & \frac{\partial N_3}{\partial y} & \frac{\partial N_4}{\partial z} & 0 & \frac{\partial N_4}{\partial x} \end{bmatrix} \tag{3.66}$$

Note that **B** is constant over the entire four noded tetrahedral volume and thus the strain field, as well as the stress field, are constant throughout the element. It is for this reason the four noded tetrahedron is referred to as a constraint-strain element. Writing Eq. (3.64) in terms of the elemental expressions derived in Eqs. (3.64) and (3.65):

$$G\left(\mathbf{u}_e, \bar{\mathbf{u}}_e\right) = \bar{\mathbf{u}}_e{}^{\mathrm{T}} \int_V \mathbf{B}^{\mathrm{T}}\mathbf{D}\mathbf{B}\, dV\mathbf{u}_e - \bar{\mathbf{u}}_e{}^{\mathrm{T}} \int_A \mathbf{N}^{\mathrm{T}}\mathbf{t}_e\, dA = 0$$
$$G\left(\mathbf{u}_e, \bar{\mathbf{u}}_e\right) = \bar{\mathbf{u}}_e{}^{\mathrm{T}} \left[\int_V \mathbf{B}^{\mathrm{T}}\mathbf{D}\mathbf{B}\, dV\mathbf{u}_e - \int_A \mathbf{N}^{\mathrm{T}}\mathbf{t}_e\, dA \right] = 0 \tag{3.67}$$

an expression for the elemental residual function is defined, neglecting body forces as they are negligible in the slipper and swashplate. If the bracketed term of Eq. (3.67) evaluates to zero, then the whole residual must be zero, thus:

$$\int_V \mathbf{B}^{\mathrm{T}}\mathbf{D}\mathbf{B}\, dV\mathbf{u}_e - \int_A \mathbf{N}^{\mathrm{T}}\mathbf{t}_e\, dA = 0$$
$$\int_V \mathbf{B}^{\mathrm{T}}\mathbf{D}\mathbf{B}\, dV\mathbf{u}_e = \int_A \mathbf{N}^{\mathrm{T}}\mathbf{t}_e\, dA \tag{3.68}$$

Since the **B** and **D** matrices are constant over the element:

$$\mathbf{B}^{\mathrm{T}}\mathbf{D}\mathbf{B} \int_V dV\, \mathbf{u}_e = \int_A \mathbf{N}^{\mathrm{T}}\mathbf{t}_e\, dA$$
$$\mathbf{B}^{\mathrm{T}}\mathbf{D}\mathbf{B} V\, \mathbf{u}_e = \int_A \mathbf{N}^{\mathrm{T}}\mathbf{t}_e\, dA \tag{3.69}$$

where V is the elemental volume which is easily expressed as a function of the nodal Cartesian coordinates:

$$V = \frac{1}{6}\det\left(\begin{bmatrix} 1 & 1 & 1 & 1 \\ x_1 & x_2 & x_3 & x_4 \\ y_1 & y_2 & y_3 & y_4 \\ z_1 & z_2 & z_3 & z_4 \end{bmatrix}\right) \tag{3.70}$$

The right hand side load vector of Eq. (3.69) will need to be evaluated numerically which can be simplified if the surface traction, $\mathbf{t_e}$, is assumed constant over the individual element face. Note that even though the face traction may be assumed constant for integration simplification over a single element, it need not be over the whole domain of elements. Writing Eq. (3.69) in a matrix formulation:

$$\begin{aligned} &\mathbf{K}_e\mathbf{u}_e = \mathbf{b}_e \\ &\text{where:} \\ &\mathbf{K}_e = \mathbf{B}^{\mathrm{T}}\mathbf{D}\mathbf{B}V \\ &\mathbf{b}_e = \int_A \mathbf{N}^{\mathrm{T}}\mathbf{t}\, dA \end{aligned} \tag{3.71}$$

the elemental stiffness matrix, $\mathbf{K_e}$, nodal displacement vector, $\mathbf{u_e}$, and load vector, $\mathbf{b_e}$, form a linear system of equations. If the formulation necessary to achieve Eq. (3.71) is repeated for every element in the solid body, and the common degrees of freedom between elements are summed, a global system of linear equations results:

$$\begin{aligned} \mathbf{K} &= \sum_e \mathbf{K}_e \\ \mathbf{b} &= \sum_e \mathbf{b}_e \\ \mathbf{K}\mathbf{u} &= \mathbf{b} \end{aligned} \tag{3.72}$$

whereby $\mathbf{u}$ represents the global deformation vector and the answer to the elasticity problem in question. Note that without imposing essential (displacement) boundary conditions on Eq. (3.72), the system of equations is singular due to the existence of rigid body motions as permissible solutions. The final system of equations with imposed constraints is solved using an incomplete Cholesky preconditioned iterative conjugant gradient solver as implemented in the GMM++ library (Renard, 2011). To increase computational efficiency, instead of solving the full system of equations given by Eq. (3.72) during every loop of the fluid structure interaction, the influence matrix method is used. In this approach, the pressure deformation of the lubricating gap is stored for the pressurization of each face with a reference pressure load. These reference deformations are appropriately scaled and summed online using the principal of linear superposition to determine the deformation of the slipper or swashplate (Schenk and Ivantysynova, 2011).

The typical pressure loading and fixed constraints for both the slipper and swashplate are illustrated in Figure 3.12.

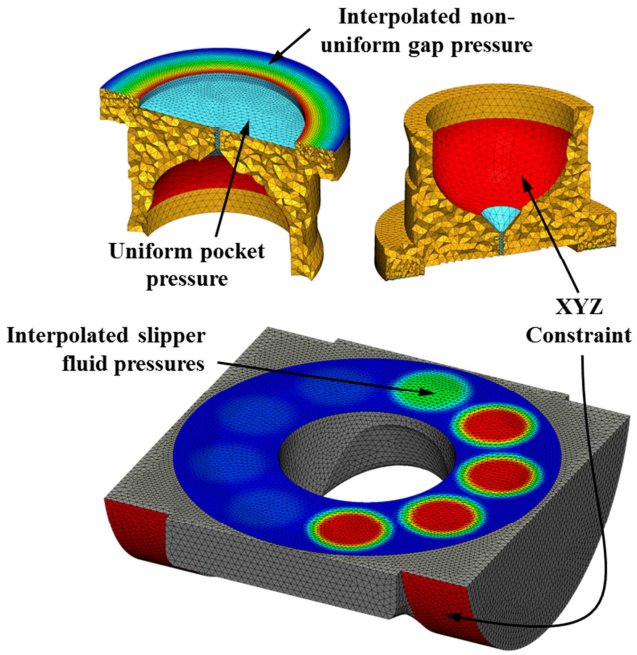

Figure 3.12. Typical boundary conditions used for calculation of the solid body pressure deformation.

An alternative option to imposing displacement boundary conditions directly at element nodes is to implement an inertia relief technique (ANSYS, 2004). In the inertia relief technique, any net forces acting on the solid body are assumed to cause a uniform acceleration. The resulting inertial reaction load due to the linear and rotational accelerations are calculated and applied to each nodal degree of freedom. This action now satisfies Newton's second law and brings the net force on the solid to be computationally zero. In spite of this imposed inertial reaction load, the body still exhibits unconstrained rigid body motion. A distributed constraint option is imposed (Gockel, 1999) which constrains the sum of mass-weighted nodal displacements to equal zero for each principal

degree of freedom. In this implementation, six Lagrange multipliers are added to the linear system:

$$\begin{bmatrix} \mathbf{K} & \mathbf{m}_x\frac{\overline{|\mathbf{K}|}}{\overline{\mathbf{m}}} & \mathbf{m}_y\frac{\overline{|\mathbf{K}|}}{\overline{\mathbf{m}}} & \mathbf{m}_z\frac{\overline{|\mathbf{K}|}}{\overline{\mathbf{m}}} & \mathbf{I}_x\frac{\overline{|\mathbf{K}|}}{\overline{\mathbf{I}}} & \mathbf{I}_y\frac{\overline{|\mathbf{K}|}}{\overline{\mathbf{I}}} & \mathbf{I}_z\frac{\overline{|\mathbf{K}|}}{\overline{\mathbf{I}}} \\ \mathbf{m}_x^T\frac{\overline{|\mathbf{K}|}}{\overline{\mathbf{m}}} & 0 & 0 & 0 & 0 & 0 & 0 \\ \mathbf{m}_y^T\frac{\overline{|\mathbf{K}|}}{\overline{\mathbf{m}}} & 0 & 0 & 0 & 0 & 0 & 0 \\ \mathbf{m}_z^T\frac{\overline{|\mathbf{K}|}}{\overline{\mathbf{m}}} & 0 & 0 & 0 & 0 & 0 & 0 \\ \mathbf{I}_x^T\frac{\overline{|\mathbf{K}|}}{\overline{\mathbf{I}}} & 0 & 0 & 0 & 0 & 0 & 0 \\ \mathbf{I}_y^T\frac{\overline{|\mathbf{K}|}}{\overline{\mathbf{I}}} & 0 & 0 & 0 & 0 & 0 & 0 \\ \mathbf{I}_z^T\frac{\overline{|\mathbf{K}|}}{\overline{\mathbf{I}}} & 0 & 0 & 0 & 0 & 0 & 0 \end{bmatrix} \begin{Bmatrix} \mathbf{u} \\ \lambda_{tx} \\ \lambda_{ty} \\ \lambda_{tz} \\ \lambda_{rx} \\ \lambda_{ry} \\ \lambda_{rz} \end{Bmatrix} = \begin{Bmatrix} \mathbf{b} \\ 0 \\ 0 \\ 0 \\ 0 \\ 0 \\ 0 \end{Bmatrix} \quad (3.73)$$

The consistent nodal mass and inertia vectors are scaled by the absolute average of the stiffness matrix divided by the average nodal mass or inertia to better condition the linear system. Although the global stiffness matrix now has zeros on the main diagonal which increases the condition matrix, because the final value of the Lagrange multipliers should be computationally zero, the performance of the iterative solver does not decrease when the initial value of λ is set to zero. Care should be taken when imposing force loads on the solid body to ensure the resulting net force is physically consistent. Specifically, in the case of the slipper, the socket which transfers the pocket and fluid film pressure force to the piston is normally constrained with a zero displacement boundary condition. If the inertia relief technique is used, a socket pressure needs to be applied to the same region to maintain the physical consistency. In this work, the inertia relief constraint methodology

is typically only used during the thermal deformation elastic analysis. Because of the nature of thermal loads, the applied solid body net force is already computationally zero, and thus the resulting inertia loads are nearly negligible. Nevertheless, the centroid constraint imposed in this inertia relief methodology is useful to not introduce constraint reaction forces on the thermal elastic deformation.

3.7 Solid Body Thermal Model

The fluid lubricating film between the slipper and swashplate is by definition thin. Due to this, a strong conduction of heat between the bounding slipper and swashplate bodies into the fluid is possible. A significant portion of the viscous heat generated within the fluid film transfers into the slipper and swashplate through conduction as illustrated in Figure 3.13. Because the fluid film thermal model developed in section 3.5 considered these solid boundaries as fixed temperatures for numerical efficiency, but the value of the surface temperature affects the thin film viscosity so strongly, it is important to iteratively update the solid body temperatures.

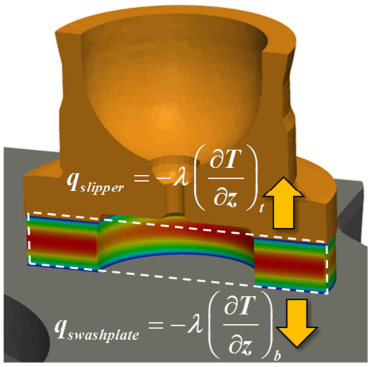

Figure 3.13. Illustration of viscous heat generation within the thin film and resulting heat conduction into the bounding slipper and swashplate solids.

It is not only the solid body temperature which can affect the thin film pressure, but due to non-uniform heating or bi-metal slipper construction, a non-uniform thermal deflection

of the slipper is the final physical phenomena which can alter the fluid film thickness and thus pressure. Because the thermal mass of the slipper and swashplate bodies is large compared to the inter-revolution variation of heat flux from the fluid film as calculated by Eq. (3.48), the solid body temperature distribution of the slipper and swashplate is solved for only once per shaft revolution using a finite element discretization approach (Liu and Quek, 2003).

3.7.1 Galerkin Method of Weighted Residuals

The governing equation for conductive heat transfer is:

$$\begin{aligned} \nabla \cdot (\mathbf{q}) &= 0 \\ \mathbf{q} &= -\lambda \nabla T \end{aligned} \tag{3.74}$$

where q is heat flux and λ is the thermal conductivity of the solid material. Similar to the elasticity equation of section 3.6, the strong form of the Eq. (3.74) will be converted into a weak varational formulation. The Galerkin method of weighted residuals will then be used in conjunction with a finite element approximation to solve for the scalar temperature field. The weak form of the conductive heat transfer equation is:

$$G\left(T,\bar{T}\right) = \int_{\Omega} \bar{T}\left(-\lambda \nabla T\right) d\Omega = 0 \tag{3.75}$$

Again using the vector product rule and divergence theorem of Eq. (3.53), Eq. (3.75) can be rewritten as:

$$\begin{aligned} G\left(T,\bar{T}\right) &= \int_{\Omega} \nabla \bar{T} \lambda \nabla T \, d\Omega - \int_{\Omega} \nabla \cdot \left(\mathbf{q}\bar{T}\right) d\Omega = 0 \\ G\left(T,\bar{T}\right) &= \int_{\Omega} \nabla \bar{T} \lambda \nabla T \, d\Omega - \int_{\Gamma} \bar{T}\mathbf{q} \cdot \mathbf{n} \, d\Gamma = 0 \end{aligned} \tag{3.76}$$

Exactly the same Galerkin method of weighted residuals described in Section 3.6.2 is made to approximate the functions T and $\bar{T}$.

3.7.2 Finite Element Discretization of the Conductive Heat Transfer Equation

The same linear tetrahedral element described in Section 3.6.3 will be used to discretize the solid body for the thermal conductive analysis, thus same Cartesian to natural coordinate transformations apply. Similar to the elastic linear tetrahedron of Section 3.6.3, the temperature field is assumed to be a weighted linear combination of the four nodal temperatures. However, unlike Eq. (3.63), for the thermal tetrahedron the temperature of a point with natural coordinates (*L1, L2, L3, L4*) is interpolated as:

$$T_p = \begin{bmatrix} T_1 & T_2 & T_3 & T_3 \end{bmatrix} \begin{Bmatrix} L1 \\ L2 \\ L3 \\ L4 \end{Bmatrix} \tag{3.77}$$

Thus, the temperate field within the tetrahedron is expressed as:

$$T(x,y,z) = \begin{bmatrix} N_1 & N_2 & N_3 & N_3 \end{bmatrix} \begin{Bmatrix} T_1 \\ T_2 \\ T_3 \\ T_4 \end{Bmatrix} \tag{3.78}$$

$$T(x,y,z) = \mathbf{N}\mathbf{T}_\mathbf{e}$$

where N_1-N_4 are the same shape functions defined in Eq. (3.62). Because of the linear element formulation, the temperature gradient will be constant within the element and can be expressed using a derivative of shape functions as:

$$\nabla T = \mathbf{B}\mathbf{T}_\mathbf{e} \tag{3.79}$$

where **B** is defined for the thermal tetrahedron as:

$$\mathbf{B}=\begin{bmatrix} \dfrac{\partial N_1}{\partial x} & \dfrac{\partial N_2}{\partial x} & \dfrac{\partial N_3}{\partial x} & \dfrac{\partial N_4}{\partial x} \\ \dfrac{\partial N_1}{\partial y} & \dfrac{\partial N_2}{\partial y} & \dfrac{\partial N_3}{\partial y} & \dfrac{\partial N_4}{\partial y} \\ \dfrac{\partial N_1}{\partial z} & \dfrac{\partial N_2}{\partial z} & \dfrac{\partial N_3}{\partial z} & \dfrac{\partial N_4}{\partial z} \end{bmatrix} \tag{3.80}$$

If a conductivity matrix is defined as:

$$\mathbf{D}=\begin{bmatrix} \lambda & 0 & 0 \\ 0 & \lambda & 0 \\ 0 & 0 & \lambda \end{bmatrix} \tag{3.81}$$

then the varational formulation of the conductivity equation, Eq. (3.76), can be written using Eqs. (3.78) and (3.79) as:

$$\begin{aligned} G\left(\mathbf{T}_e,\overline{\mathbf{T}}_e\right) &= \overline{\mathbf{T}}_e^{\mathrm{T}}\int_V \mathbf{B}^{\mathrm{T}}\mathbf{D}\mathbf{B}\,dV\mathbf{T}_e-\overline{\mathbf{T}}_e\int_A \mathbf{N}^{\mathrm{T}}\mathbf{q}\cdot\mathbf{n}\,dA=0 \\ G\left(\mathbf{T}_e,\overline{\mathbf{T}}_e\right) &= \overline{\mathbf{T}}_e^{\mathrm{T}}\left[\int_V \mathbf{B}^{\mathrm{T}}\mathbf{D}\mathbf{B}\,dV\mathbf{T}_e-\int_A \mathbf{N}^{\mathrm{T}}\mathbf{q}\cdot\mathbf{n}\,dA\right]=0 \end{aligned} \tag{3.82}$$

Since the **B** and **D** matrices are constant over the whole element domain, and since if the bracketed term of Eq. (3.82) evaluates to zero, then the whole residual must be zero Eq. (3.82) can be simplified as:

$$\begin{aligned} &\mathbf{B}^{\mathrm{T}}\mathbf{D}\mathbf{B}V\mathbf{T}_e=\int_A \mathbf{N}^{\mathrm{T}}\mathbf{q}\cdot\mathbf{n}\,dA \\ &\mathbf{K}_e\mathbf{T}_e=\mathbf{b}_e \\ &\text{where:} \\ &\mathbf{K}_e=\mathbf{B}^{\mathrm{T}}\mathbf{D}\mathbf{B}V \\ &\mathbf{b}_e=\int_A \mathbf{N}^{\mathrm{T}}\mathbf{q}\cdot\mathbf{n}\,dA \end{aligned} \tag{3.83}$$

where V is the elemental volume expressed in Eq. (3.70). After formulating the thermal stiffness matrix of each individual element, they are combined with common degrees of

freedom between each separate element being added together to form a global system of equations:

$$\begin{aligned} \mathbf{K} &= \sum_e \mathbf{K}_e \\ \mathbf{b} &= \sum_e \mathbf{b}_e \\ \mathbf{KT} &= \mathbf{b} \end{aligned} \tag{3.84}$$

In a typical conductive heat transfer analysis, three different types of wall boundary conditions can be applied: Dirichlet, Neumann, or mixed. The simplest type of boundary condition, termed Dirichlet, is an essential boundary which specifies a fixed wall temperature. This particular boundary condition removes a degree of freedom from the final thermal stiffness matrix as the temperature value is prescribed. The Neumann boundary condition is a natural boundary which specifies a wall heat flux. If the specified heat flux is constant over the element face, the evaluation of the area integral of Eq. (3.83) is simplified and the appropriate equivalent nodal flux terms are assigned. The last boundary type, mixed, specifies a wall heat flux which varies with the surface temperature. The magnitude of heat flux is directly proportional to the difference between the surface temperature and some reference temperature, and may be found from the convective heat transfer equation:

$$q = \eta \left(T_w - T_{ref} \right) \tag{3.85}$$

where η is the heat transfer convection coefficient. Although this convective heat flux q appears on the right side of Eq. (3.83), because of the appearance of the wall temperature in Eq. (3.85), the relevant portion of the integral which contains T_e terms will need to be moved into the thermal stiffness matrix. Fortunately, because Eq. (3.85) is linear, the final system of thermal equations remains linear as well. On a final note, because the

mixed boundary condition is dependent on nodal temperature, this boundary condition (as well as the Dirichlet) is sufficient to remove the singularity from the global thermal stiffness matrix and determine a unique temperature solution. Similar to Section 3.6, the final system of constrained equations is solved using an incomplete Cholesky preconditioned iterative conjugant gradient solver as implemented in the GMM++ library (Renard, 2011). Typical thermal boundary conditions applied to the slipper and swashplate are indicated in Figure 3.14.

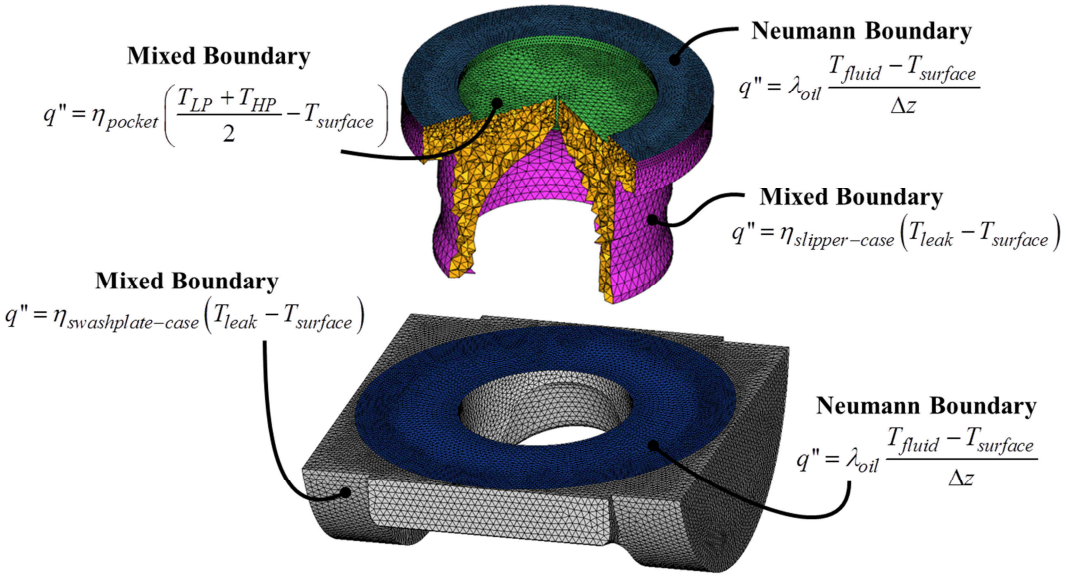

Figure 3.14. Thermal boundary conditions for both the slipper and swashplate.

3.7.3 Determination of Case Convection Coefficients

Due to the dependence of the solid body temperature distribution on the convective heat transfer coefficient, a short study was undertaken to determine reasonable values for the slipper and swashplate case surfaces which would be difficult to simplify to a standard convective geometry. A commercial CFD software package, AcuSolve, was used to estimate proper convection coefficients for different surfaces on the slipper and

swashplate bodies. A rotating coordinate system was used to impose a boundary velocity on the slippers, shaft, and cylinder block to avoid a transient moving mesh problem. The full Navier-Stokes equations were solved using a Spalart-Allmaras turbulence model. The convection coefficient is estimated internally by the software using the non-dimensionalized velocity field and the theory of self-similarity. A constant property fluid model was use with values typical of mineral oil and listed in Table 3.1. Figure 3.15 illustrates the fluid velocity vector field and surface convection coefficient distribution.

Table 3.1. Oil fluid properties used in the CFD case convection coefficient analysis.

Density (kg/m^3)	871
Specific Heat (J/kg·K)	1880
Dynamic viscosity (Pa·s)	0.03
Thermal conductivity (W/m·K)	0.13

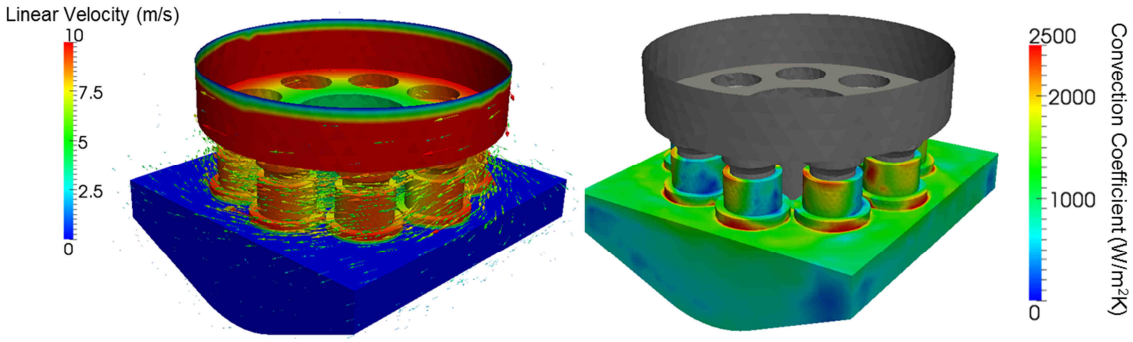

Figure 3.15. Convection coefficients for the external surfaces of the slipper and swashplate bodies at a pump speed of 1500 rpm.

A mean value of the convection coefficient was taken over the slipper and swashplate bodies individually. This process was repeated for a number of pump shaft speeds on a 130 cc/rev sized piston unit. Further studies on smaller sized units with higher rotating speeds have shown similar magnitudes of convection coefficients for similar values of

linear (tangential) velocities. Thus the average convection coefficient values reported in Table 3.2 are listed in terms of the tangential velocity of the outer block surface.

Table 3.2. Approximate slipper / swashplate case convection coefficients.

Outer block tangential velocity (m/s)	Average slipper case surface convection coefficient (W/m^2K)	Average swashplate case surface convection coefficient (W/m^2K)
3.3	600	500
6.7	1000	750
10	1400	1000
13.3	1700	1200
16.7	2000	1400
20	2200	1600

3.7.4 Calculation of Thermal Forces from Thermal Strain

Once the temperature distribution of the solid is found, the thermal strain can be found on an elemental basis. Since an isotropic material model is assumed, and the four noded tetrahedron is a constant strain element, the elemental thermal strain can be found:

$$\boldsymbol{\varepsilon}_T = \begin{Bmatrix} \alpha_T \Delta T \\ \alpha_T \Delta T \\ \alpha_T \Delta T \\ 0 \\ 0 \\ 0 \end{Bmatrix} \tag{3.86}$$

where ΔT is the temperature change to a reference temperature. In this application, the reference temperature is commonly take to be 20°C; a temperature at which the components are nominally sized. Given this thermal strain, the elemental thermal deformation forces, can be calculated as follows:

$$\mathbf{f}_T = \int_V \mathbf{B}^{\mathrm{T}} \mathbf{D} \boldsymbol{\varepsilon}_T \, dV = \mathbf{B}^{\mathrm{T}} \mathbf{D} \boldsymbol{\varepsilon}_T V \tag{3.87}$$

with the simplification possible because **B**, **D**, and $\boldsymbol{\varepsilon_T}$ are constant over the four noded tetrahedron element volume. These elemental nodal forces are summed over all the nodes, and the resulting load vector is used with the elasticity equation of section 3.6 to find the thermal deformation of the solid body. The resulting thermal deflection can actually be quite large due to growth of the entire body. However, this uniform component of thermal deformation does not alter the shape of the gap and simply causes the solid body to move uniformly away to achieve the same film thickness. Although this is what happens physically, it is difficult to numerically handle such large uniform deformations. To remedy this problem, the minimum point of deflection on the sealing land surface is considered as a reference (or point of zero thermal deformation) and the relative thermal deformation to that minimum point is only considered.

The slipper is a small part with large outer convection coefficients due to the churning of the slippers within the fluid filled pump case volume. Because of this, and considering the geometric symmetry (or near symmetry in the case of a vented slipper design), there is often little non-uniform thermal deflection of the slipper. Although the swashplate does have regions of localized heating, the thermal deformation over the running face does not significantly vary. Moreover, because an individual slipper sealing land only is affected by a small region of the swashplate at an instant in time, the thermal swashplate deformation is neglected.

3.8 Interpolation Between the Solid and Fluid

The physical phenomena affecting the fluid film thickness and thus slipper fluid pressure have now been fully described and mathematically modeled. However, because a non-unified scheme has been used to segregate the fluid and solid domains and common

information must be passed between them, from an implementation standpoint, a challenge remains.

An interpolation method which can transfer necessary variables between the non-coincident fluid and solid mesh (Figure 3.16) is the solution to this problem. Specifically, fluid pressure and heat flux need to be transferred to the solid mesh cell faces while solid body deformation and temperature are transferred from the solid mesh cell nodes to the fluid.

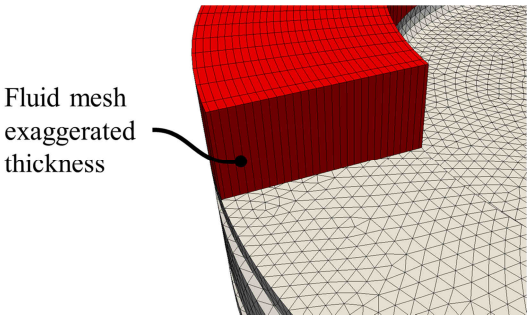

Figure 3.16. Mismatch between fluid and solid meshes.

To interpolate from the solid mesh to the fluid, the value at the fluid volume centroid is determined based on the bounding element nodes as illustrated for a representative fluid volume in Figure 3.17. Because the shape function for the four noded tetrahedron is based on Barycentric coordinates, Barycentric interpolation will be used in a two-dimensional formulation. The value at the cell centroid location is calculated as:

$$\phi_f = \lambda_1\phi_1 + \lambda_2\phi_2 + \lambda_3\phi_3 \tag{3.88}$$

where λ_1, λ_2, λ_3 are the Barycentric coordinates of the fluid centroid for the triangle formed by the three bounding tetrahedron faces nodes and ϕ_1, ϕ_2, ϕ_3 are either values of deformation or temperature at the three nodes.

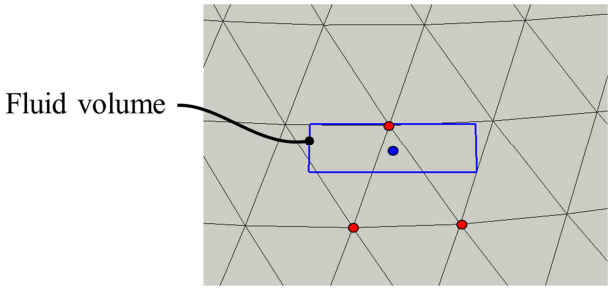

Figure 3.17. Solid to fluid interpolation scheme.

A similar scheme is used to transfer fluid pressure or heat flux to the solid. An assumption is made that for a single tetrahedron face, the applied load will be constant over the face. Thus the query point for interpolation on the solid is the face centroid. Three fluid volumes are found such that when the fluid centroids are connected, the resulting triangle bounds the solid mesh face centroid as illustrated in Figure 3.18. Again, Barycentric interpolation is used to find the face centroid value on constructed “fluid triangle”.

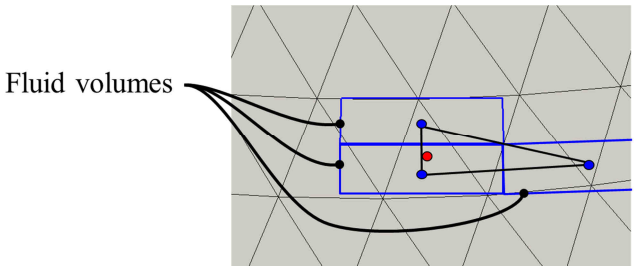

Figure 3.18. Fluid to solid interpolation scheme.

This Barycentric interpolation method is robust and accurate provided the two meshes are of similar magnitudes of size, which is the case for this work. Figure 3.19 provides an example of fluid solid mesh pressure interpolation on the left, and solid to fluid mesh deformation interpolation on the right.

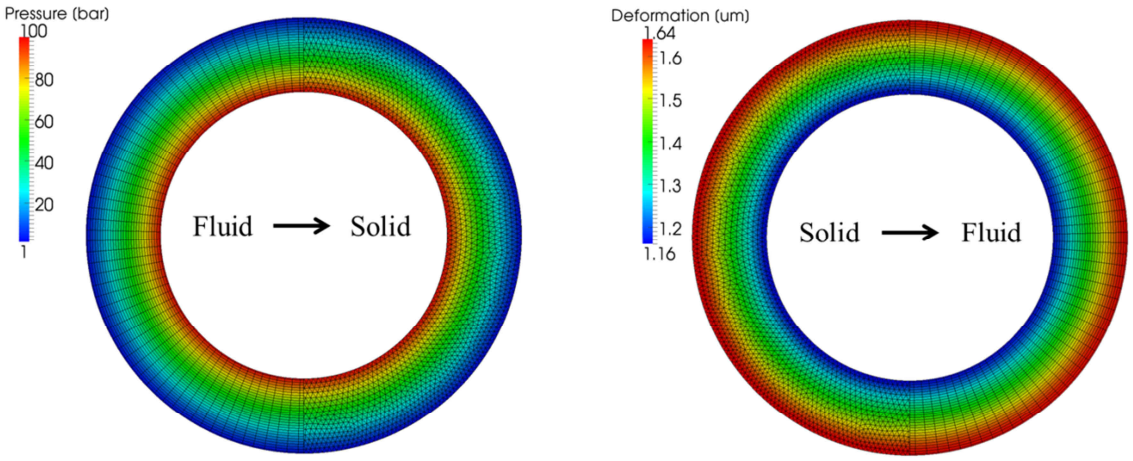

Figure 3.19. Example of Barycentric interpolation between the fluid and solid.

3.9 Coupling of the Fluid-Structure-Thermal Slipper-Swashplate Lubrication Model

The multiple partitioned numerical models which have been presented must now be numerically coupled to provide a meaningful prediction of slipper lubrication performance. The fluid film pressure is the heart of the developed model; all of the other segmented analysis updates variables which will impact pressure generation in the lubricating regime. In order to attain the highest level of computational efficiency while simultaneously maintaining physical accuracy, the model interactions are partitioned into three numerical convergence loops.

The first loop is termed the fluid-structure-interaction loop; within this loop the thin film / pocket pressure, temperature, and solid body pressure deformation are iteratively updated until convergence is reached. At that point, the solid body deformation and fluid temperature are held fixed and a solid body micro-dynamics loop calculates the net force acting on the slipper body and adjusts its micro velocity as necessary to achieve a force balance. In this process, the fluid film / pocket pressure as well as an integration of

slipper micro-velocity are continuously calculated until the force balance within a specified tolerance is found. Following the convergence the simulation time and shaft angle are advanced and the fluid structure interaction loop resumes. The third and final loop updates only at the beginning of each shaft revolution. In this thermal fluid-structure interaction loop, the viscous heat generation from the slipper is summed over the shaft revolution and a solid body heat transfer simulation is performed to calculate the surface temperature of the slipper and swashplate. Using the calculated change in solid body temperature of the slipper, a thermal deformation is calculated. Both the new slipper thermal deformation as well as the slipper/swashplate boundary temperature distribution are updated and held constant for the next shaft revolution. Final model convergence occurs when sufficiently small thermal changes occur between shaft revolutions. A high level overview of these three loops and their coupling are illustrated in Figure 3.20.

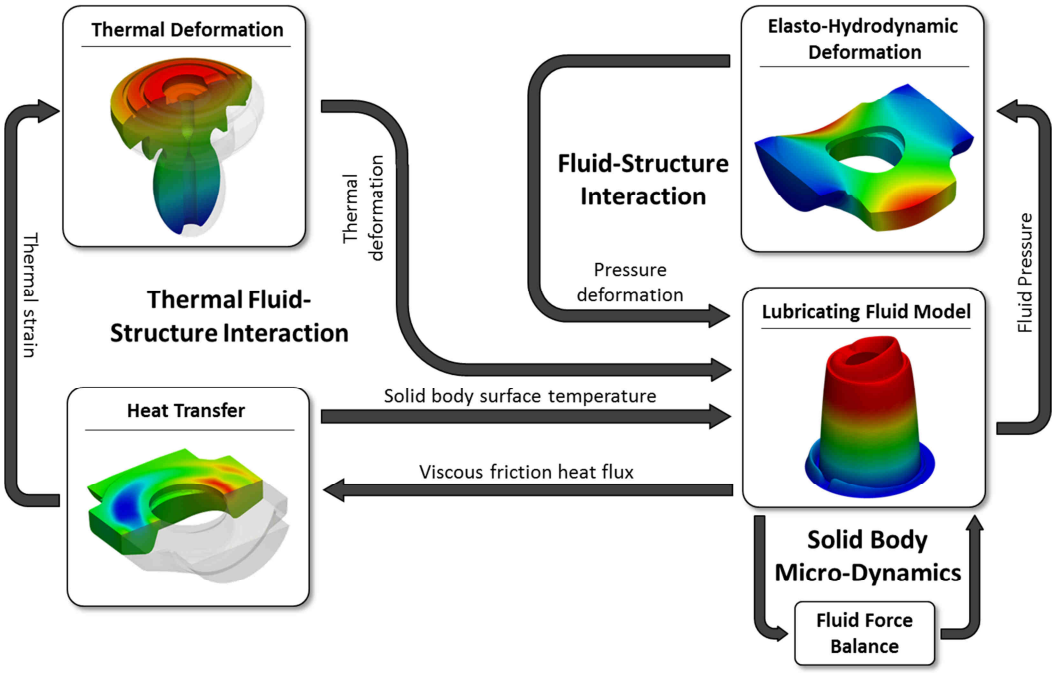

Figure 3.20. Slipper swashplate lubrication model overview.

From an implementation standpoint, the solution scheme begins by assuming initial states of many variables: a guessed initial rigid body separation of 10-15 micrometers between the slipper and swashplate is assumed. Initial pressure deformations are found by assuming pocket pressure equal to displacement chamber pressure and a linear approximation of the pressure field in the lubricating domain. An adiabatic wall boundary is assumed over the gap region during the solution for an initial solid body temperature distribution and the slipper thermal deformation. With initial variable states set, the iterative scheme begins. A detailed flowchart diagram of this iterative scheme is presented in Figure 3.21 and will be described in remaining sections of this chapter.

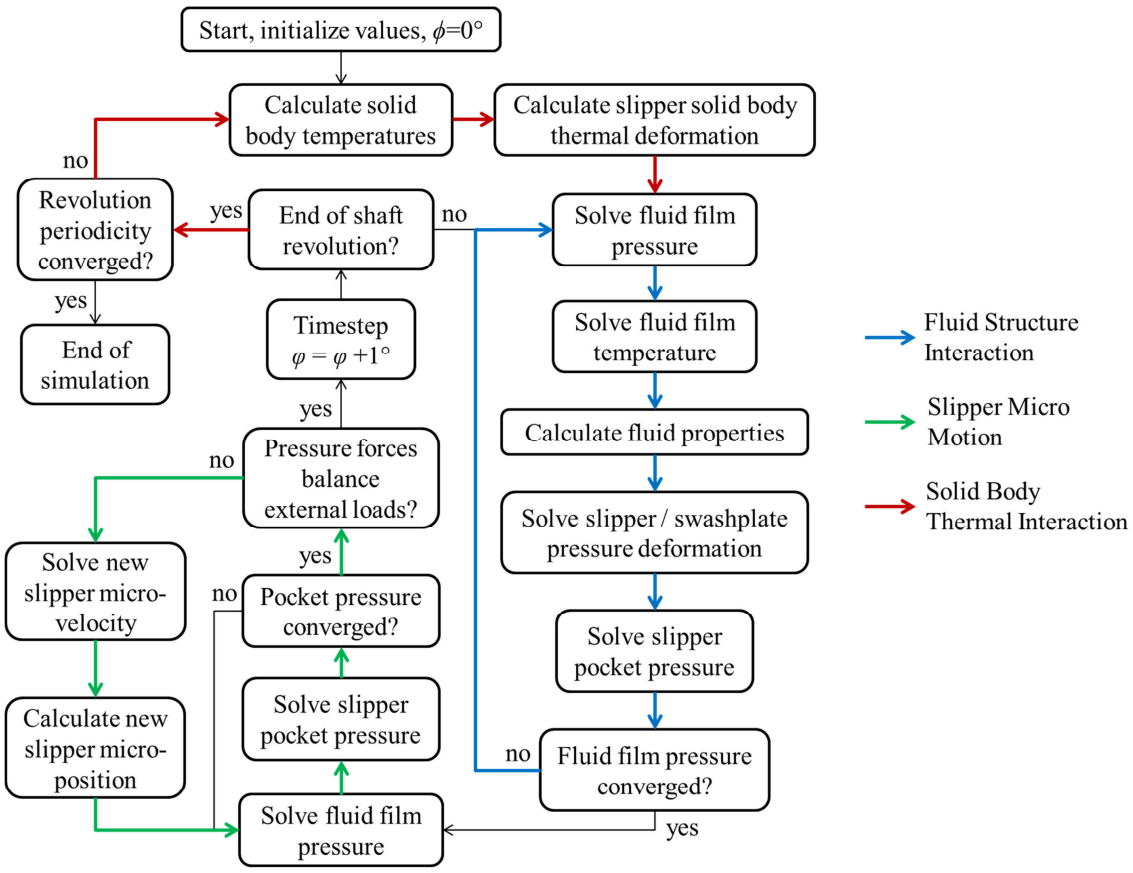

Figure 3.21. Slipper swashplate lubrication model flow chart.

3.9.1 Fluid Structure Interaction

The thin film pressure model begins by solving for the lubricating pressure distribution. Initially the pressure solution is under-relaxed with a factor of 0.8 using the standard expression:

$$p_{new} = p_{old} + \alpha\left(p - p_{old}\right) \tag{3.89}$$

Progress of the pressure residual is monitored over the fluid-structure interaction process and the under-relaxation factor is increased or decreased as necessary with a lower limit of 0.005 encountered at minimum fluid film thicknesses. Using the calculated thin film pressure distribution, Eq. (3.34) calculates the leakage into the pump housing through the slipper gap. The pocket pressure model updates the value of pressure within the slipper pocket using the calculated value of slipper leakage. The pocket pressure is typically under-relaxed by 0.5 which becomes more necessary during slipper lift off as small changes in fluid film thickness can significantly impact leakage and therefore pocket pressure. Also using the Reynolds pressure distribution, fluid velocities within the film are calculated. Using the fluid velocities, the energy equation solves for an updated thin film temperature distribution and heat flux into the solid bodies. The fluid viscosity is recalculated using this new fluid temperature distribution. With the new pocket and thin film pressures, the pressure deformations of the slipper and swashplate are recalculated. Because significant changes in pressure deformation from hydrostatic contributions are possible from one time step to the next, at the beginning of each time step changes in pressure deformations are under-relaxed into the fluid film thickness over 25-50 iterations. Following these updates to fluid viscosity, film thickness, and pocket pressure the thin film pressure residual is recalculated. Naturally, the residual calculation does not

incorporate pressure under-relaxation. The value of this residual determines the overall fluid-structure-interaction solution progress and when a normalized pressure residual value of 1e-4 has been reached, the solution is considered converged. If the pressure residual is above convergence criteria, another iteration of this fluid structure interaction loop is performed being with an updated solution of the thin film pressure. Due to the slow fixed relaxation of updated slipper and swashplate pressure deformations, a minimum of 25-50 iterations are required. However, once the minimum iterations have been reached and the pressure residual is below the specified tolerance, the solid body micro motion loop begins.

3.9.2 Solid Body Micro-motion

The solid body micro motion loop considers the pressure deformation of the slipper and swashplate as well as the fluid temperature, and thus viscosity, to remain constant. Although this is an approximation, without it the computational expense to continually update the fluid structure interaction loop would be too great for practical usage. Moreover, because the underlying fluid structure interaction loop cannot employ significant parallel computation, further advances in parallel computing techniques are not expected to change the situation. Nevertheless, at the initial force balance between the calculated pocket and thin film fluid force and the external forces is calculated for each of the three degrees of slipper micro-motion freedom. Each of the three slipper micro-motion control point velocities (Figure 3.8) are perturbed slightly with a central difference method to calculate the force-velocity Jacobean matrix. Every time a control point velocity is changed, the new micro position of the slipper is found through integration and then the thin film pressure and the slipper pocket pressure model iterate to

convergence. A new guess at the slipper micro velocity is found using Newton's method as described in section 3.4. If the new slipper micro velocity results in a fluid pressure which satisfies the force balance tolerance, the simulation time and shaft angle are advanced. Elsewise, the process repeats with an updated iteration of Newton's method. The finite difference Jacobean matrix is updated every other iteration of Newton's method.

3.9.3 Solid Body Thermal Fluid Structure Interaction

Once the simulation shaft angle advances, a check is performed to determine if a full shaft revolution has occurred since the last solid body thermal solution. If not, the simulation proceeds to being the fluid structure interaction loop again (section 3.9.1). However, if a full shaft revolution has been completed, the summed net heat flux from the slipper fluid film interface is properly applied through interpolation to both the slipper and swashplate bodies. The applied heat flux is typically under relaxed by 0.5-0.6. The solid body temperature is calculated as well as the resulting thermal deformation of the slipper. All of these temperature / deformation distributions are under relaxed by the same 0.5-0.6 factor and then interpolated back to the slipper fluid film. In the case of the swashplate temperate, the interpolation must repeat with every shaft angle change, but the underlying swashplate field remains the same. A check is then performed to determine if the specified number of shaft revolutions have been calculated as requested and if so the simulation ends. Else, the model proceeds to update the fluid structure interaction loop for the shaft angle now with updated values of solid body temperatures and slipper thermal deformation. Following the end of the simulation, a manual check is performed

to determine if the change between shaft revolutions of thermal effects stabilized, which typically happens in 6-10 revolutions.

An illustrative diagram depicts the governing equations and solution sequence of each sub-model and the higher level nonlinear interactions in Figure 3.22.

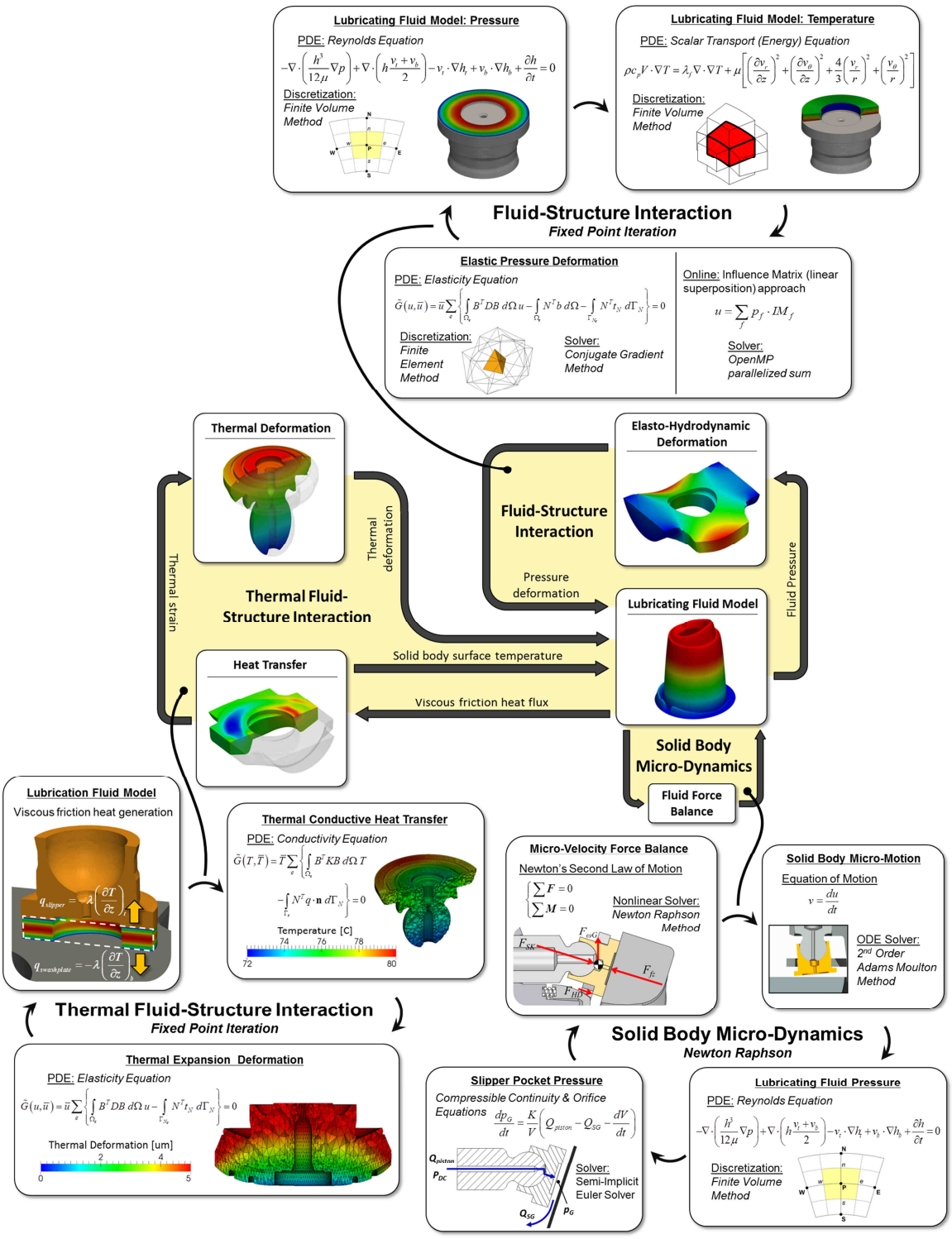

Figure 3.22. Detailed slipper swashplate lubrication sub-model interactions.

3.10 Original contributions

Highlighted contributions from this work which are original, considering the literature as a reference, to the numerical model of lubrication between the slipper and swashplate include:

- Use of a polar-coordinate based Reynolds equation containing complete source terms to account for surface inclinations of both the slipper and swashplate and rectilinear boundary velocities imposed on a cylinder grid.
- Consideration of the compressibility of fluid within the slipper pocket and the resulting transient pressure changes.
- Incorporation of structural deformation of the slipper due to both pressure and thermal loads, accomplished using a finite element discretization technique and open source linear solvers.
- Inertial relief elasticity constraint technique implemented using lambda multipliers to constraint rigid body translations and rotations.
- Development of a finite element based conductive heat transfer solver for the solid body heat transfer within the slipper and swashplate bodies.
- Implementation of an implicit ODE integrator to solve for updated slipper micro-positions within the solid-body micro motion iterative loop.
- Full coupling and convergence of the fluid-structure interaction problem at every timestep.
- Discovery of the importance of transient deformation impact on hydrodynamic squeeze pressure generation.

CHAPTER 4. SLIPPER FLUID FILM THICKNESS TEST RIG

4.1 Test Rig Design

A commercially manufactured 130 cc/rev variable displacement swashplate type axial piston pump was modified to directly measure the distance between the swashplate surface and the slipper at six locations on the swashplate, thus measuring the lubricating fluid film thickness. Environmental conditions under which the sensor must operate, combined with performance requirements, complicate the design modifications and limit possible sensor technologies. Ideally, installation of the sensor would not modify the swashplate surface; any direct modification of the swashplate surface has potential to alter the fluid film itself. Unfortunately, this is presently unfeasible using commercially available sensor technologies. Alternatively, the three most common sensor technologies requiring modification of the swashplate surface are optical, capacitive, and eddy current. Optical sensors are unsuitable due to the high pressure acting on the sensor face and the variability of the optical characteristics of the working hydraulic oil. Minimal changes to the overall pump packaging were desired to reduce custom manufacturing, significantly constraining the packaging space available to insert sensors. Additionally, sufficient clearance for wire routing is necessary to consider with sensor selection.

Capacitive sensors have an advantage with respect to smallest sensing diameter; eddy current sensors require a coil winding which has a limited minimum diameter. However

the capacitive sensors often incorporate an active “guard shield” to minimize the effect of electric field fringing, complicating sensor design. Due to the physical principal, capacitive sensors are sensitive to the dielectric constant of the material between the sensor and the target. Therefore the sensor face and guard need to be directly exposed to high pressure fluid. In contrast, an eddy current sensor is unaffected by non-metallic separating media, enabling the entire sensor to be surrounded by ceramic. This outer shell enables significantly larger fluid pressures at the sensor face. Based on the need to withstand high sensor face pressures as well as a compact design, an eddy current sensor manufactured by the Micro-Epsilon corporation was selected. The model type EU05(93) sensor was used with integrated o-ring as shown in Figure 4.1, with custom manufacture modifications made for a longer cable length. Further details regarding sensor type selection can be found in Spencer (2014). The resolution of the sensor rated by the manufacturer is based on noise peak-to-peak values and at 100 kHz is 0.2% FSO or 1 micrometer.

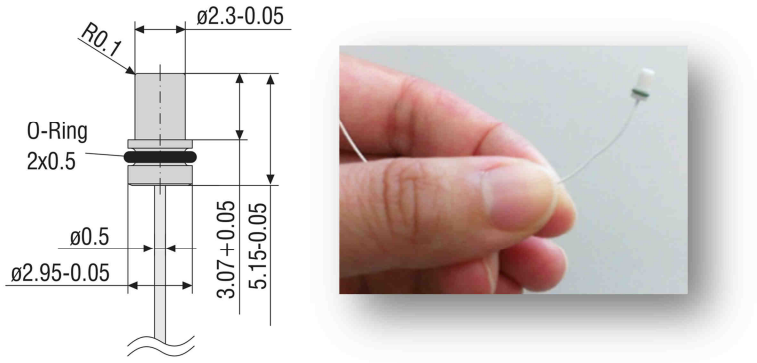

Figure 4.1. Micro epsilon eddy current sensor EU05(93). (Image credit: Micro-epsilon and Spencer, 2014).

To insert the sensors into the swashplate with the least amount of modification, a two-piece swashplate design was proposed as illustrated in Figure 4.2. In this modified design,

the sensors were sandwiched between an upper and lower swashplate half, with the small sensor cables exiting the swashplate sides. This is necessary since only a small portion of the swashplate underside is not covered by roller bearings or the shaft preventing a thru exit of the sensor wire. Notice the eddy current sensor is actually recessed below the swashplate surface by 50-150 μm. This is necessary because the sensor design itself limits the minimum measured distance to 50 μm and additionally to provide a manufacturing tolerance. The magnitude of this recess will need to be quantified and subtracted from the measured sensor distance to determine the fluid film thickness.

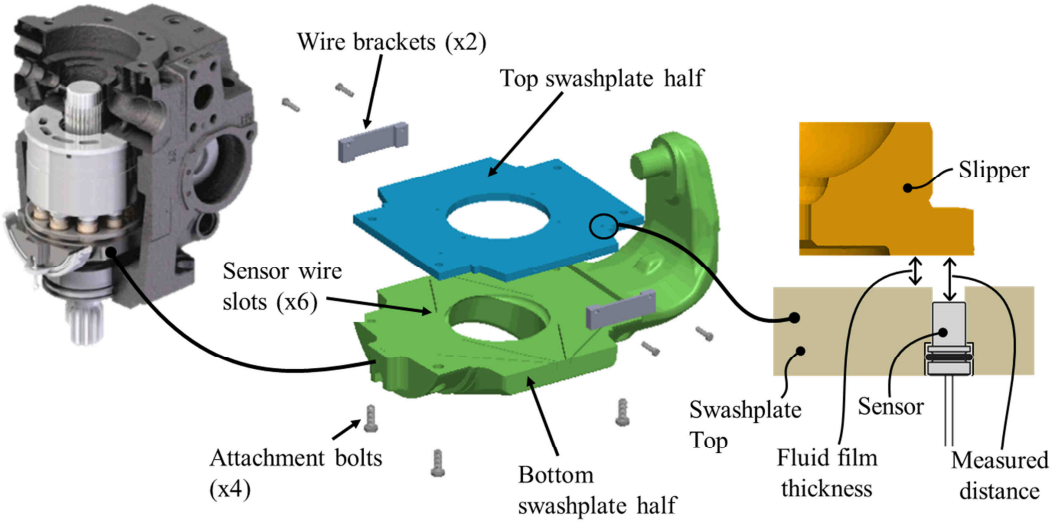

Figure 4.2. Illustration of slipper test rig assembly. (Image credit: Vonniederhausern, 2012 and Spencer, 2014).

The general location of the six sensors stemmed from a desire to measure the slipper position in all four quadrants of the swashplate face. Within the general areas, specific sensor locations were determined using an algorithm developed by Spencer (2014). The algorithm found sensor locations which maximized the degrees of shaft rotation the sensor is totally covered by the slipper. Figure 4.3 illustrates the sensor path as the slipper passes over a sensor located at three different radial locations. Interestingly, a sensor

located on the main pitch diameter will only be fully occluded by the slipper for a total of 10° of shaft rotation. Instead by locating the sensor to trace over the radially inner and outer land portions, larger magnitudes of total occlusion of 23° and 17° can be respectively obtained. Due to this property, four of the sensors are located on the inner slipper radius while the remaining two sensors are located at the outer radius as dimensioned in Figure 4.4.

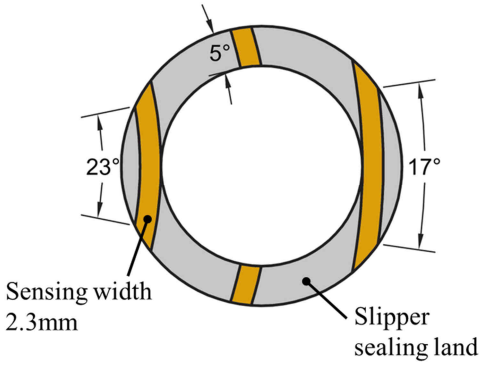

Figure 4.3. Illustration of the eddy current sensor path traced over a slipper at different radii.

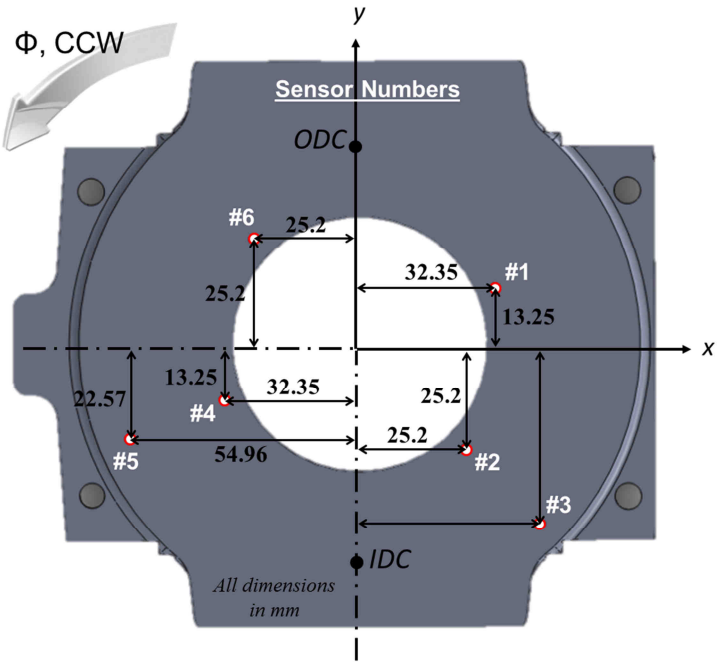

Figure 4.4. Eddy current sensor locations on swashplate.

The initial design called for two originally manufactured swashplates to be used as base stock for machining both the upper and lower swashplate halves. In this approach, the swashplate surface finish would remain exactly as the original equipment manufacturer intended; unfortunately the swashplate is hardened in the manufacturing process. Small machining features needed in the top swashplate half were unable to be manufactured by local machinists in this hardened steel. A comprise was made to manufacture the top swashplate half from plain 4140 steel with a post surface grinding operation. The bottom swashplate half was machined from an original equipment manufacturer swashplate. Figure 4.5 shows the final result of the bottom swashplate half with the eddy current sensors resting in their appropriate locations. During actual assembly, the sensors are first inserted into the swashplate top half due to the o-ring, and then the swashplate top with installed sensors is lowered onto the swashplate bottom half.

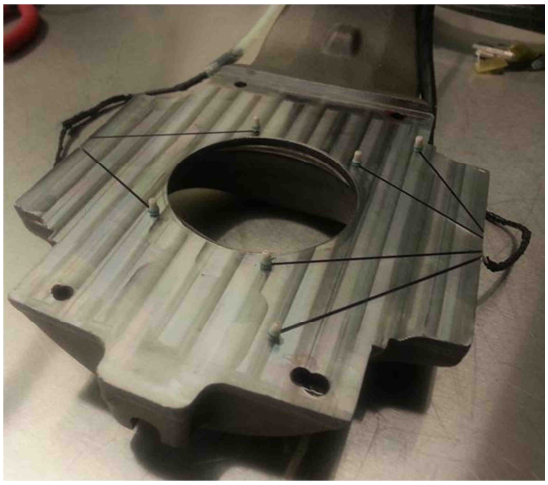

Figure 4.5. Sensors installed on the bottom half of the swashplate (top swashplate not shown).

Following mating of the swashplate halves, the sensor wires are threaded through openings in the pump case which will be sealed with a rubber stopper during operation as shown in Figure 4.6.

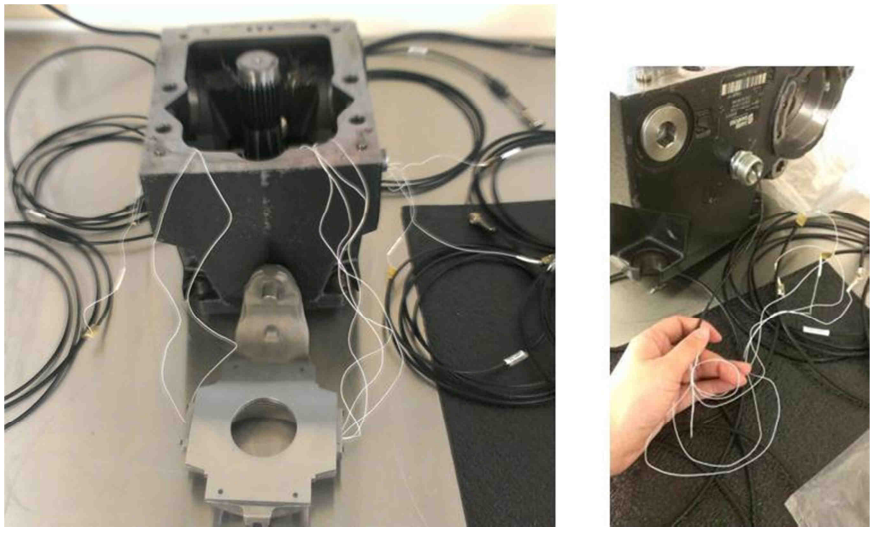

Figure 4.6. Assembled swashplate before being inserted into the pump housing.

Following final assembly of the pump, it was mounted onto a steady state test bench as illustrated in Figure 4.7. Although driven primarily by an electric motor, due to the large torques needed to drive the pump at full displacement and high pressure, a variable

displacement hydraulic motor is installed to reduce electric motor load. To reduce the cost of signal conditioning (Micro-Epsilon DT3301) and data acquisition equipment required, each of the six sensors was not measured simultaneously, but rather in a sequence. Additional sensors used during steady state measurements are diagramed in Figure 4.8. A full list of the sensor specifications used for these experimental measures is given in Table 4.1.

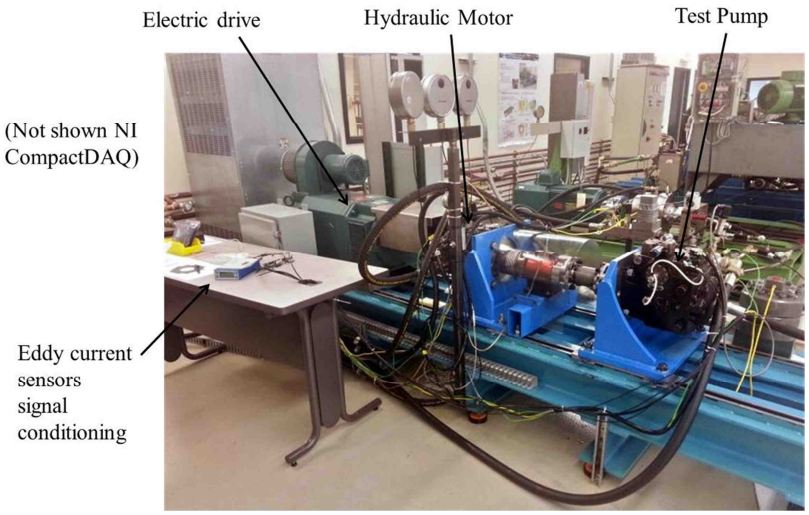

Figure 4.7. Steady state test bench with the special instrumented pump mounted.

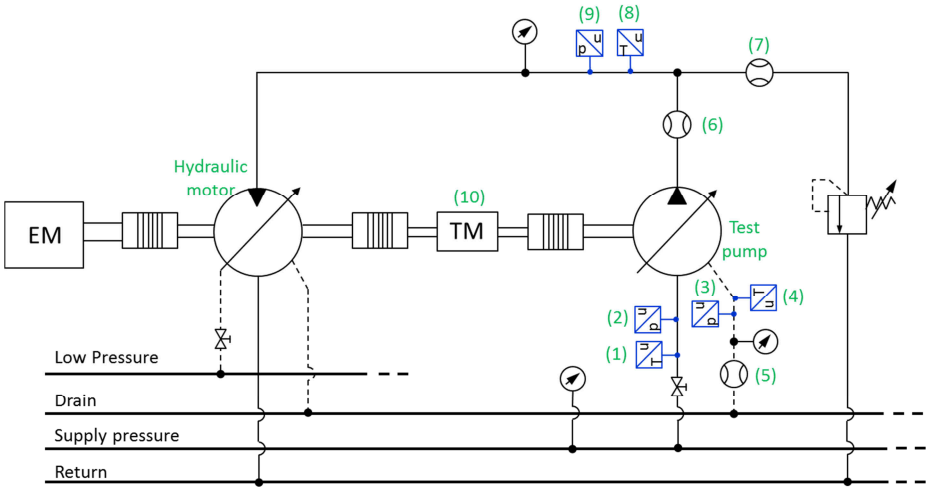

Figure 4.8. Steady state testing circuit.

Table 4.1. List of test rig sensors.

Sensor Number	Sensor description
1, 4, 8	Omega K Type Thermocouple (2.2° C Error limit)
2	WIKA S-10 Pressure transducer (0-100 bar, 0.125% BFSL)
3	WIKA S-10 Pressure transducer (0-25 bar, 0.125% BFSL)
5	VSE VS 0.2 Gear type flow meter (0.02 - 18 L/min flow range, 0.3% Accuracy)
6	VSE VS 10 Gear type flow meter (1.2 - 525 L/min flow range, 0.3% Accuracy)
7	KRACHT VC 5 Gear type flow meter (1-250 L/min flow range, 0.3% Accuracy)
9	HYDAC HDA 4445 Pressure transducer (0-600 bar, 0.5% BFSL)
10	Dr. Staiger Mohilo Torque / speed transducer (0 - 1000 Nm and 60 imp/rev, 0.1% FSO Accuracy)
	NI cDAQ 9178 with NI 9211, NI 9201, NI 9205 modules

4.2 Test Rig Measurement and Data Processing

The test pump was initially run with a constant inlet temperature of 52 ± 1°C until the outlet and drain port temperatures reached a steady state value to within ±1°C. At this point the unit reached a thermal steady state operation and 30 seconds of high speed data acquisition was preformed, recording the measured voltage of a single eddy current sensor. This process was repeated six times for each sensor, waiting a minimum of three minutes following each sensor switch to allow the electronics to reach thermal equilibrium.

Following testing, the raw voltage data obtained from the eddy current sensors was converted to a film thickness using a linear scale, calibrated with a multipoint fit. An example of this transient data is shown in Figure 4.9. Because the sensor is continuously acquiring data, film thickness information from all nine slippers is acquired sequentially. Although the test rig does not contain a trigger to associate each reading with a unique slipper, within each acquisition the measured traces can be grouped by slipper. This post-processing is done using the off-scale high measured values as a trigger. Figure 4.10 plots the grouped data for a single slipper using the same raw data. Approximately 500 traces of the same slipper taken during the 30 second sampling are displayed.

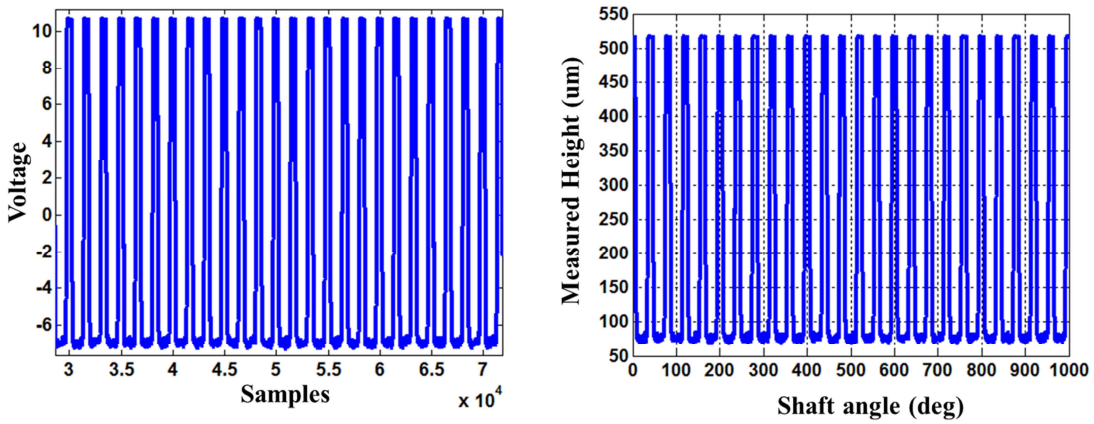

Figure 4.9. Raw data obtained from Sensor #1 at n = 1000 rpm, Δp = 100 bar, β = 18°.

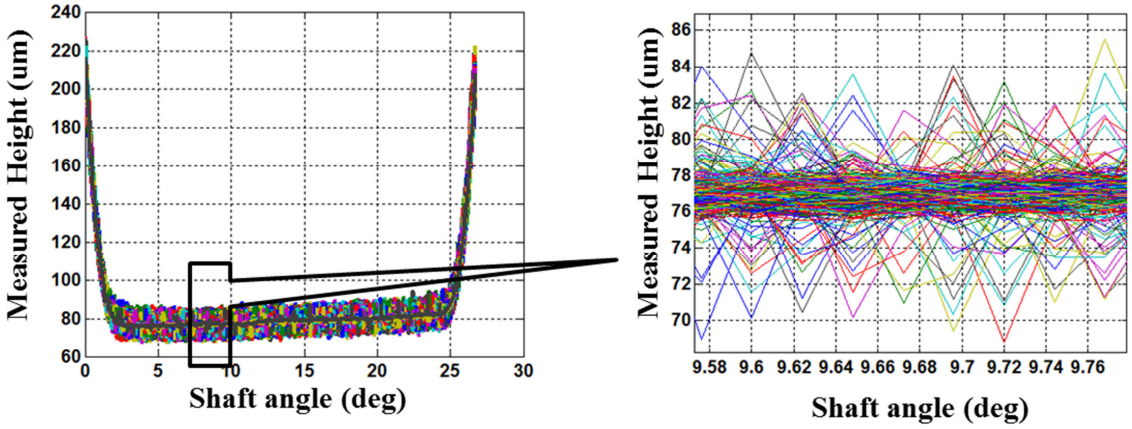

Figure 4.10. Grouping data from a single slipper obtained from Sensor #1 at n = 1000 rpm, Δp = 100 bar, β = 18°.

A mean line of the grouped measured data can be calculated as well as error lines representing plus and minus one standard deviation as plotted in Figure 4.11. The error bounds in this plot are typical of all the data acquired during the testing with a standard deviation of 1.3 micrometers measured distance. No other filtering is used in the data post processing aside from the data averaging described.

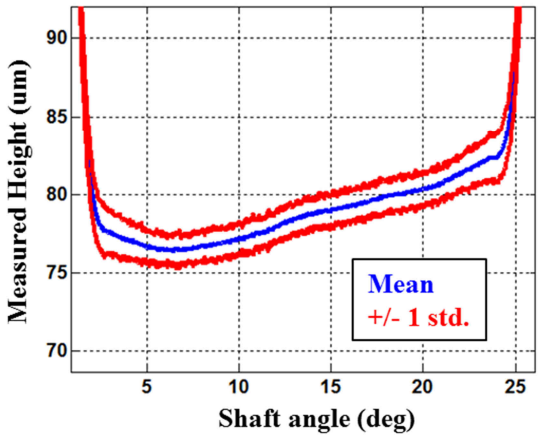

Figure 4.11. Averaged data of a single slipper from Sensor #1 at n = 1000 rpm, Δp = 100 bar, β = 18°.

4.3 Initial Slipper Test Rig Operation

Following a short period of test rig operation (2-3 hours), a flexible shaft coupling failed. Although failure of the coupling was believed to be unrelated to the pump modifications, the piston unit was unmounted and disassembled. A photograph of the swashplate surface after disassembly is shown in Figure 4.12. Regions of polishing due to surface wear are visible as well as a localized region of gouging at the outer radius.

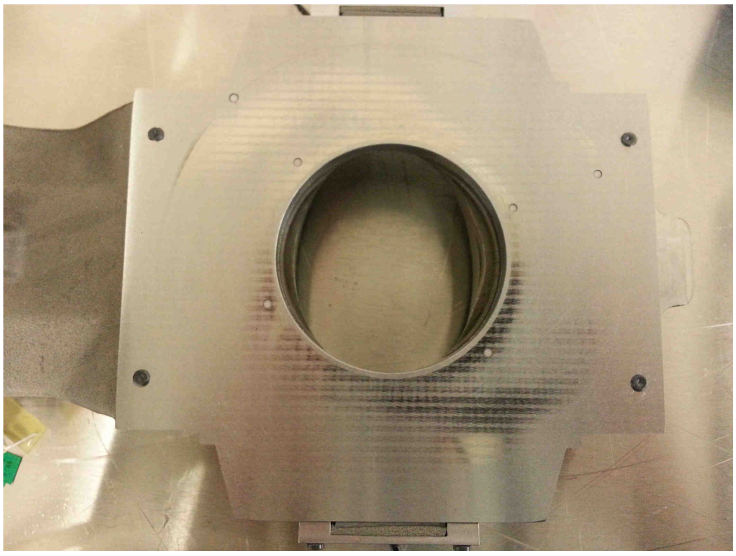

Figure 4.12. Swashplate surface following initial operation showing gouging and polishing.

The impact of swashplate gouging on the slipper is evident by comparing surface profile traces of the slipper surface from before and after this initial testing as plotted in Figure 4.13. Slipper surface profiles are measured using a stylus profilometer which measures the sealing land deflection over a single planer cross-section. A full cross section is taken and then aligned post measurement to correct for any rigid body tilting of the slipper in the measurement setup. An illustration of the profilometer measurement process is shown

in Figure 4.14. Note that because the slipper is tipped upside down for testing, low spots along the profile path will actually increase the fluid film thickness.

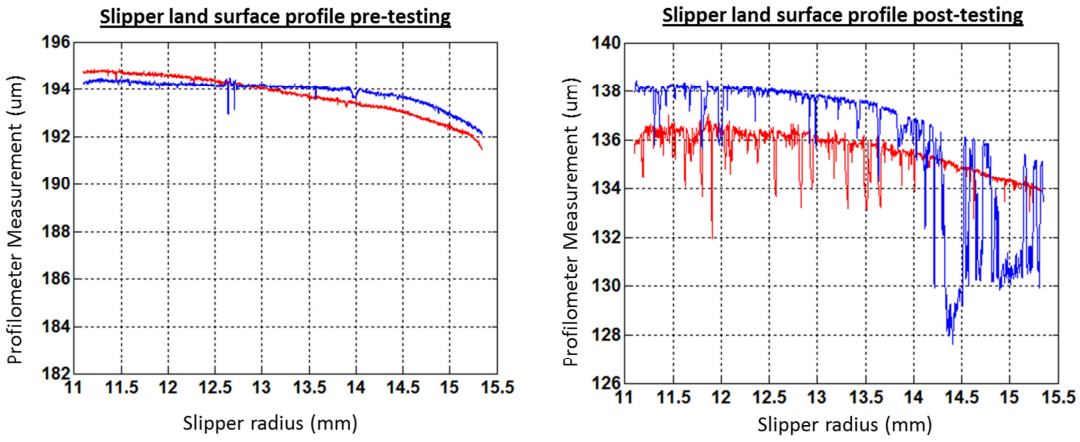

Figure 4.13. Pre-test and post-test of slipper sealing land surface measured with a stylus profilometer.

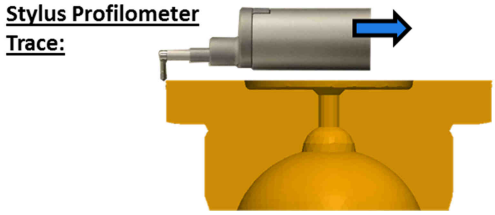

Figure 4.14. Illustration of stylus profilometer trace of the slipper sealing lands.

The cause of the swashplate gouging is believed to be due to the manufacturing of the swashplate running surface. Although the top swashplate was surface ground which achieves a specified surface finish, the grinding operation does not necessarily ensure flatness. Following this initial testing, to improve top surface flatness the swashplate was hand lapped. Unfortunately the limited surface finishing capabilities of the lapping machine shop actually increased the final surface roughness. Measured surface roughnesses of the commercially manufactured, ground, and hand lapped swashplate are given in Table 4.2.

Table 4.2. Test rig swashplate surface roughnesses.

	Surface roughness (Ra) [μm]
Commercially manufactured swashplate	0.1
Surface ground swashplate	0.4
Hand lapped swashplate	0.7

4.4 Lapped Swashplate Test Rig Operation

After the swashplate was lapped, the test rig was reassembled with a new set of piston / slipper pairs. These slippers were run under four steady state operating conditions as given in Table 4.3.

Table 4.3. Lapped swashplate initial run in operating conditions.

Shaft speed (rpm)	HP port pressure (bar)	Displacement (%)
1000	125	20
1000	125	50
1000	125	100
1000	225	50

Following this initial run-in, the pump was disassembled and the surface profile of the slipper running surface was measured using a Mitutoyo SJ-500 stylus profilometer (x-axis accuracy 0.05 μm, z-axis accuracy: 0.01 μm). The surface traces from this testing are compared to slippers which had been run on an unmodified swashplate by Zecchi (2013) in Figure 4.15. The magnitudes of wear over the slipper lands are very similar.

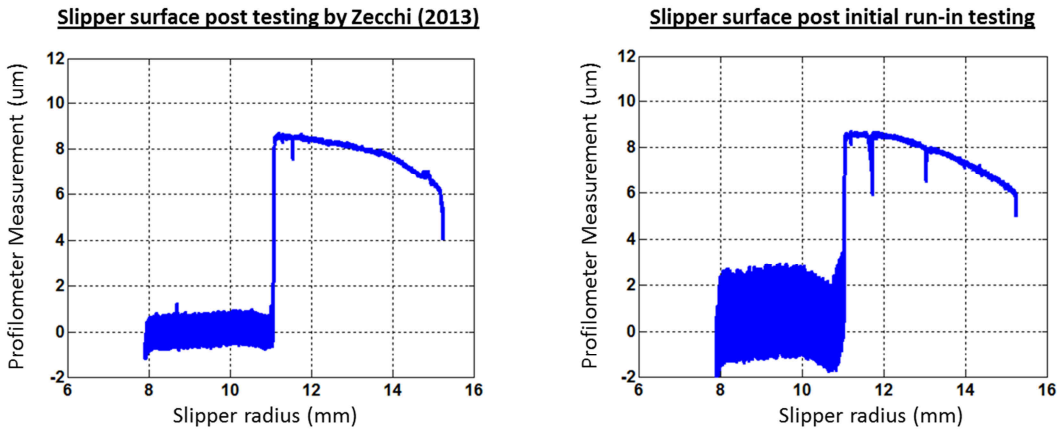

Figure 4.15. Comparison of slipper surface profile post testing by Zecchi (left), and post initial run-in operation.

The pump was reassembled using the piston slipper pairs that had just undergone run-in without any modifications and full testing began. Six operating conditions were measured continuously over one day. The pump was brought to steady state thermal operation before any eddy current sensor acquisition began. Averaged steady state data from these six operating conditions is presented in Table 4.4 with the testing order indicated.

Table 4.4. Averaged steady state pump data from testing after swashplate lapping.

Test Order	n [rpm]	β (approx.) [%]	Δp [bar]	QHP [l/min]	QLK [l/min]	pHP [bar]	pLP [bar]	THP [°C]	TLP [°C]	TLK [°C]	M [Nm]
1	998	50	100	57.7	1.52	126.3	25.6	55.3	52.6	60.3	121.5
2	998	100	100	126.3	1.02	125.7	25.7	55.0	52.9	61.4	236.0
3	998	20	100	19.5	1.87	124.9	25.1	56.9	52.3	61.7	58.4
4	998	20	200	14.7	3.96	225.2	25.3	62.3	52.3	68.9	101.0
5	998	50	200	54.0	2.55	225.5	25.4	57.9	52.7	66.4	227.6
6	998	100	200	122.4	1.77	226.6	26.1	57.1	53.0	74.7	464.1

Pump shaft torque measured during this testing was compared to that measured by Zecchi (2013) during testing of an identical unit, but without modifications directly affecting the sliding interfaces. However, since those measurements were taken at slightly different port pressures, the shaft torque measured by Zecchi was adjusted for direct comparison

using Eq. (4.1) where the prime variables were those measured by Zecchi. A comparison between measured torque values from Table 4.4 and the adjusted torque measured by Zecchi (2013) are given in Table 4.5. Notice that for all but the last operating condition the shaft torque measured for this special test rig is very similar to the adjusted torque measured by Zecchi. The increase in torque is attributed to solid to solid contact between the slipper and swashplate.

$$M_{adjusted} = M_{measured}{}' + \left(p_{HP} - p_{HP}{}' - p_{LP} + p_{LP}{}' \right) \frac{Q_{HP}}{2\pi n} \tag{4.1}$$

Table 4.5. Comparison between measured shaft torque to adjusted shaft torque measured by Zecchi (2013).

n [rpm]	β (approx.) [%]	Δp [bar]	M [Nm]	Zecchi Adjusted M [Nm]
998	50	100	121.5	121.0
998	100	100	236.0	237.8
998	20	100	58.4	57.9
998	20	200	101.0	102.8
998	50	200	227.6	226.7
998	100	200	464.1	455.4

At the conclusion of acquiring film thickness sensor data for these six operating conditions the pump was disassembled. Photographs of the slipper surface following run-in at four operating conditions (Table 4.3) and following full testing (Table 4.4) are included in Figure 4.16. Unfortunately significant wear caused the outer sealing land to wear away such that the nine micrometer step is no longer present. Data measured using the stylus surface profilometer confirms the visual change of the sealing land wear and is plotted in Figure 4.17. It is assumed this wear occurred during the final operating condition when an unexpected increase in shaft torque was measured.

Figure 4.16. Photograph of a slipper following run-in (left) and following full testing at six operating conditions (right).

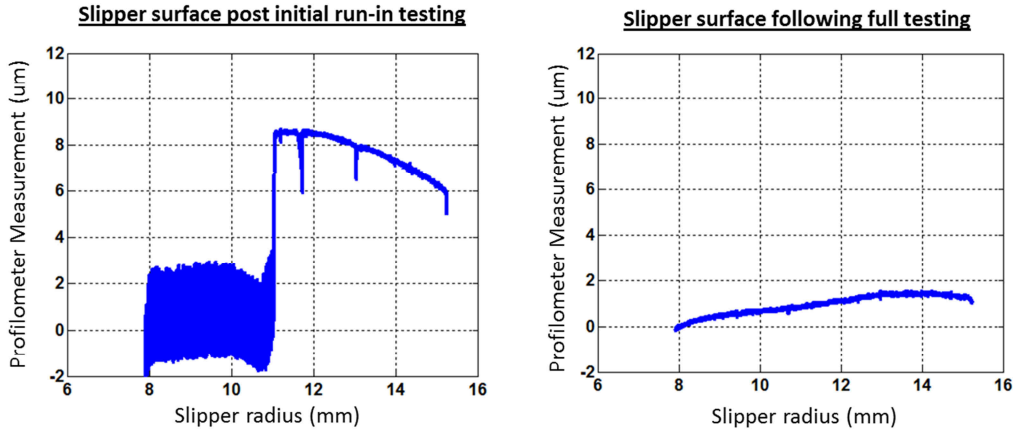

Figure 4.17. Surface profilometer traces of the slipper land following run-in (left) and following full testing at six operating conditions (right).

4.5 Conversion of Simulation Results to Measured Sensor Representation

The test rig measures the average film thickness above the sensor face with respect to time. Instead, the numerical model described in Chapter 3 simulates the entire lubricating fluid domain in a moving coordinate system. Moreover, the coordinate system and rotation direction used in the test rig (Figure 4.4) does not align with the default swashplate coordinate system used in the simulation model (Figure 2.6). To easily compare the simulation results to measured values, a post-processing scheme is utilized on the simulation results to convert them into a comparable format. A “virtual” sensor is created from 1024 discrete points spaced to represent equal areas over the sensor face as

illustrated in Figure 4.18. The simulated slipper film thickness is correctly orientated considering the measurement coordinate system and then interpolation of the fluid grid height onto individual sensor points is performed. Sensor points which are not occluded by the slipper are assumed an off-scale high value of 500 μm. An average of the sensor points is taken and the scalar value is recorded for each shaft angle. The result of this process are simulation results which can be directly compared to measured values.

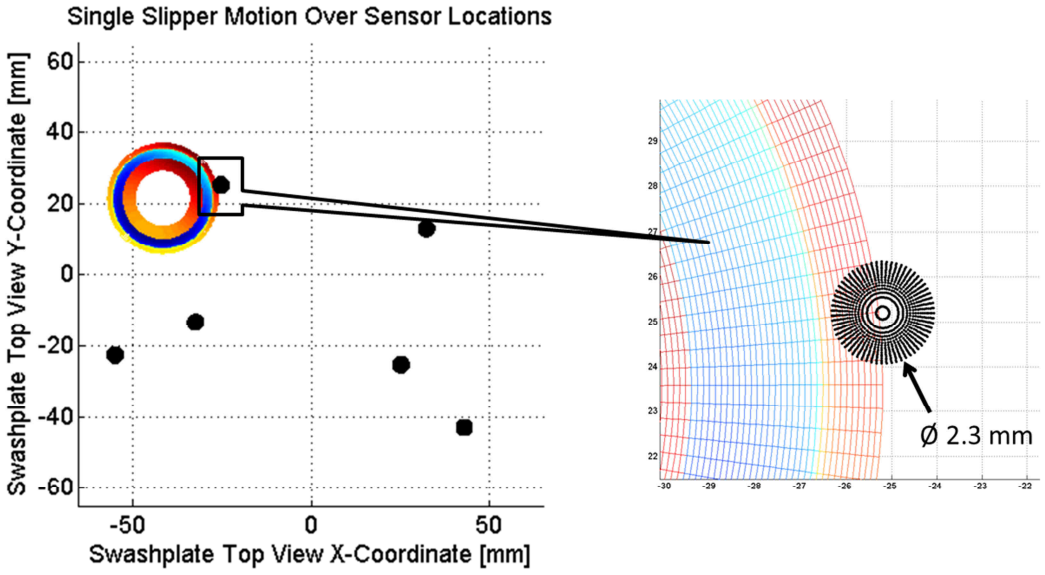

Figure 4.18. Graphic representation of simulation post-processing into sensor readings.

The distance measured by the sensor is comprised of multiple components, each of which combines to yield the final measured distance. The five components are illustrated in Figure 4.19. The slipper micro distance and inclination as well as deformation are calculated by the simulation model described in Chapter 3 while the partial sensor occlusion and sensor diameter height averaging are accounted for by the virtual sensor method described previously in this section. The slipper land wear was measured both pre and post testing using a stylus profilometer. The final significant contribution to

measured distance is the sensor recess depth which is attempted to quantify using a calibration scheme described in the next section.

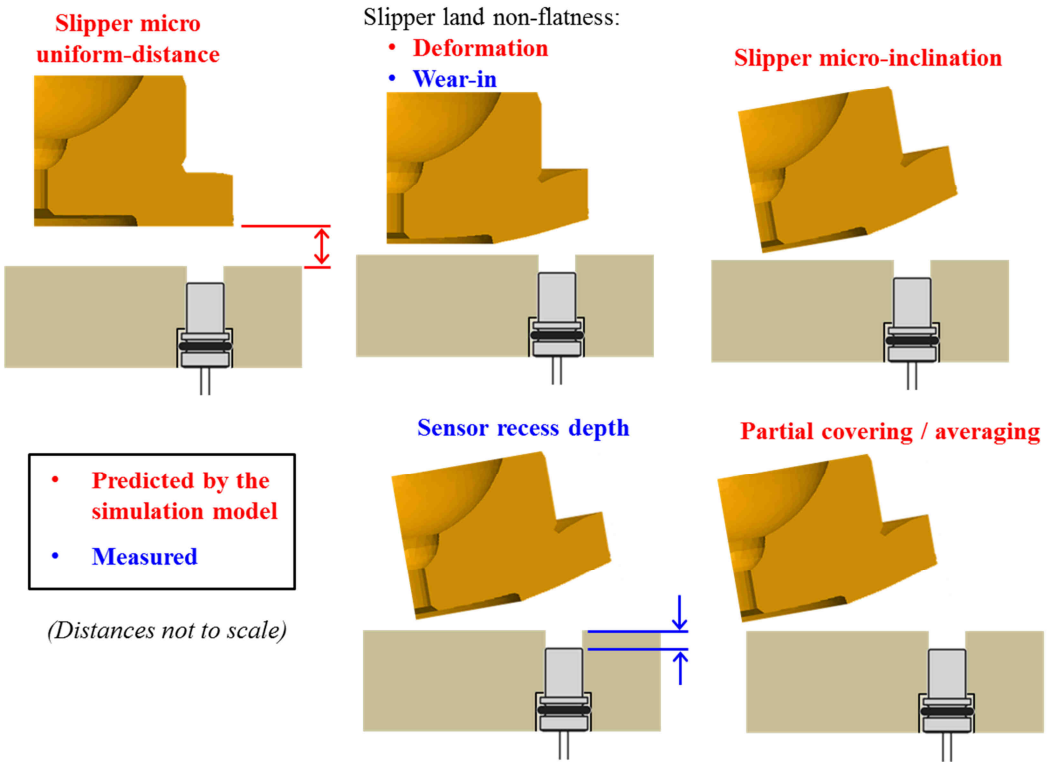

Figure 4.19. Subcomponents affecting the total sensor measured distance.

4.6 Calibration of Sensor Recess Depth

Quantification of the sensor recess depth is complicated due to the small length scale and limitations of surface flatness. Although both the swashplate top and bottom were machined flat, there are both surface roughness and larger non-flatness deviations present in the actual components. Additionally the sensor bottom itself is not flat as it is an epoxied surface with a dome shape. A hypothetical illustration of these additional affects is illustrated in Figure 4.20. When the swashplate assembly is in operation inside the pump, large pressure forces acting over the swashplate top will compress the two halves to reduce the localized separation. Additionally, as the slipper passes over a sensor, high

pressure will act on the sensor face which has the possibility to press the sensor further against the swashplate bottom. These two factors affect sensor recess depth in opposite magnitudes; as the swashplate top and bottom become compressed the recess depth will decrease whereas when the sensor is pressed into the swashplate bottom the recess depth will increase.

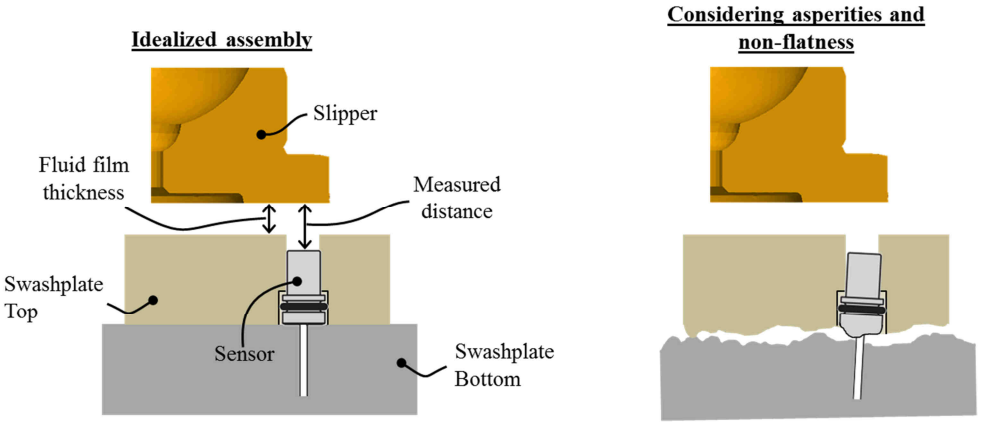

Figure 4.20. Illustration of geometric variations likely present in the swashplate assembly.

A set of slippers were specially modified to remove the nine micrometer step manufactured into the sealing land; the result was slippers with only the main pocket. Removing the step caused the slippers to be significantly underbalanced hydrostatically. The impact of this is when the displacement chamber is pressurized, the slipper must come into direct metal contact with the swashplate as the hydrostatic pressure field alone will be unable to support the piston force. These nine flat calibration slippers were placed into the pump and it was reassembled and mounted again on the test rig. The pump was operated at 1000 rpm with a minimum pressure differential until the inlet, outlet, and drain temperatures were above 52° C. The pump inlet and outlet ports were then externally pressurized to 125 bar. The pump shaft was slowly manually rotated until a slipper fully occluded each sensor and the minimum measured film thickness was

recorded. This procedure was repeated twice on consecutive days. The minimum measured values, interpreted as the sensor recess depth, are listed in Table 4.6. An average of these two measured values will be used for correct for the sensor recess depth illustrated in Figure 4.19.

Although the values reported here are close in magnitude, the results in the next section exhibit negative film thicknesses at some sensor locations. The root cause of this is the inability to rigidly fix the sensor into the base such the recess depth cannot change between assembly / disassembly of the unit or under changing operating conditions. Thus while the sensor error is on the order of 1.3 micrometers, the measured film thickness error is larger due to the inaccuracy in the sensor recess depth measurements. The effect of this is that the relative deflection of the film thickness over the sensor trace has an error of 1.3 micrometers, but the absolute magnitude of the film thickness error is larger.

Table 4.6. Minimum sensor measured distances using calibration slippers.

		Sensor Recess Depth (μm)	
		Trial #1	**Trial #2**
Sensor Number	1	81.5	81.5
	2	100	101
	3	60.5	59.5
	4	105	105
	5	22.5	23
	6	98	98

4.7 Comparison of Measured Sensor Data to Simulations for Multiple Operating Conditions

Simulations were run using the measured boundary conditions from Table 4.4 and a film thickness modification shown in Figure 4.21 to account for the run-in slipper wear and pocket depth measured in Figure 4.15 (right).

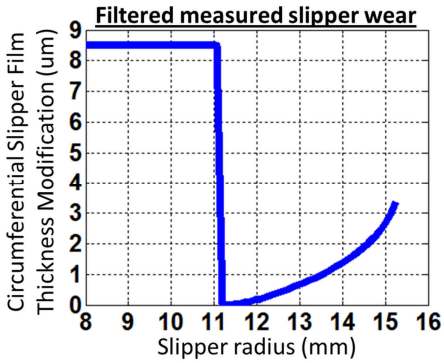

Figure 4.21. Filtered profilometer measured slipper profile included in comparison simulations.

The virtual sensor method described in the section 5.5 was used to convert simulation results to a format directly comparable with the measured sensor data. High speed measurements taken during pump operation at the conditions listed in Table 4.4 were corrected by the mean calibrated recess depths listed in Table 4.6. Graphs plotting both the measured and simulated film thicknesses at each sensor for the six operating conditions are presented in the following Figure 4.22 – Figure 4.27 with the mean measured line from each of the nine slippers plotted.

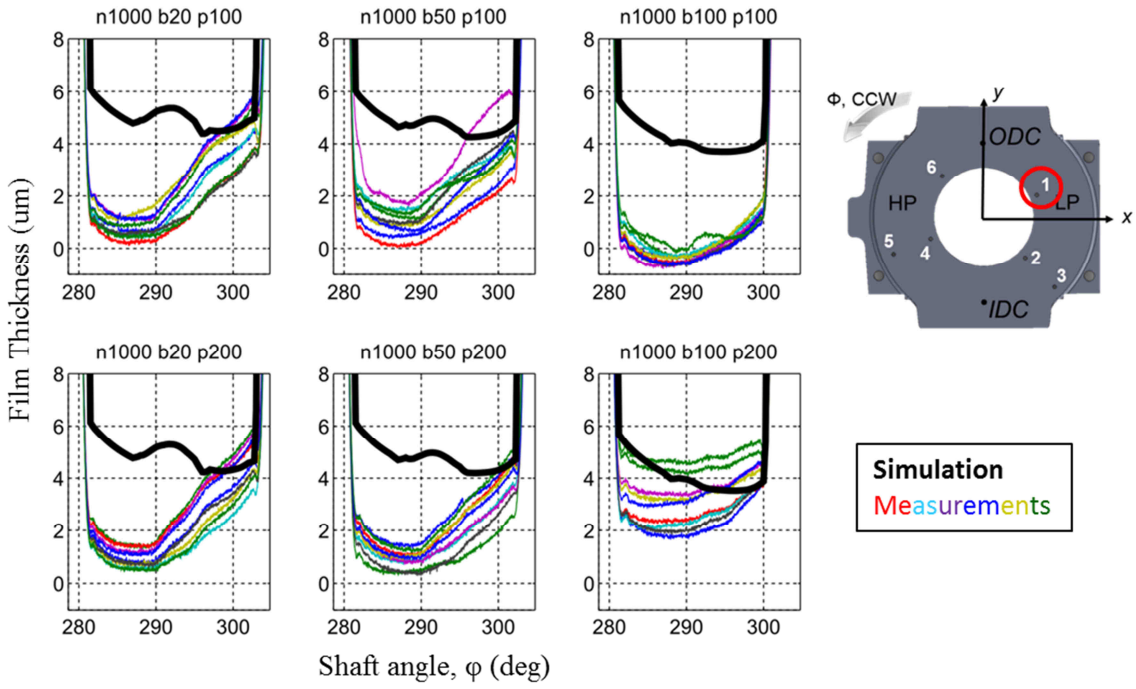

Figure 4.22. Fluid film thickness measurements and simulation results at sensor location 1.

The measured results at sensor location one are impressive. Small variations between slippers during the measurements can either be attributed to physical variation in the physical slippers, true variation during operation, or measurement error. Nevertheless, the variations remained within two micrometers. Unfortunately a portion of the measured data has a negative value which is unphysical. Negative measured film thickness values stem from the recessed sensor design; the sensor measures a total distance which includes a recess depth. Although the calibration procedure described in the previous section attempted to accurately quantify the recess depth, dis/re-assembly of the pump as well as uncontrolled variability with the multi-piece swashplate / sensor assembly evidently introduce errors, which although only on the order of micrometers, are sufficient to result in reported values of negative film thickness.

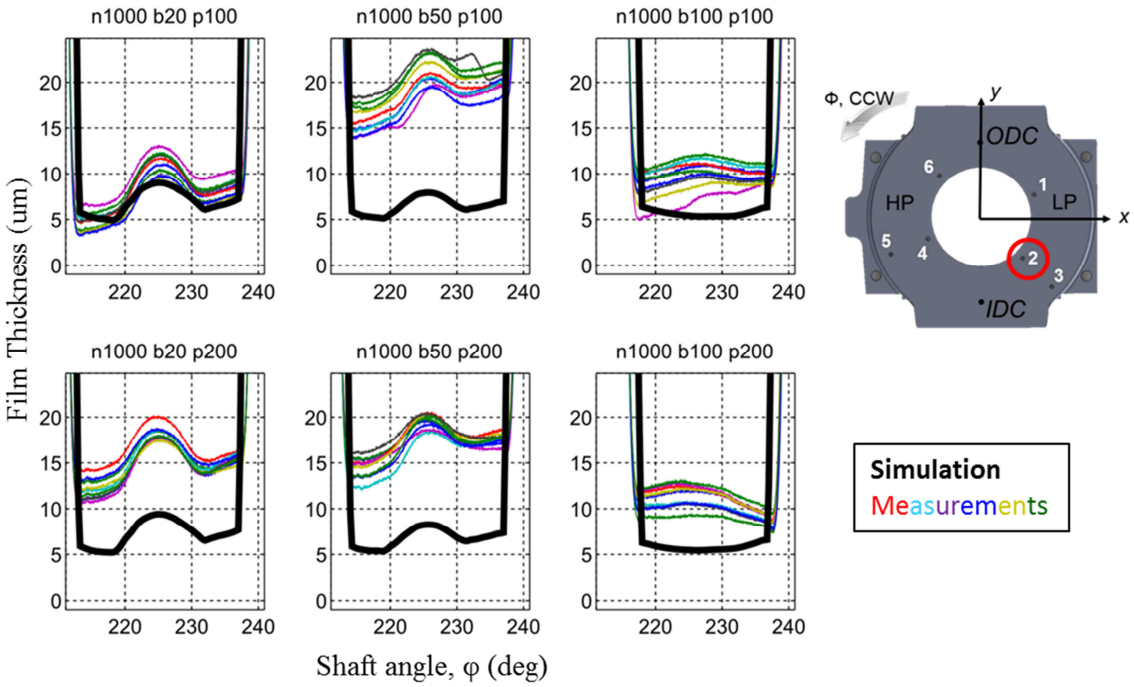

Figure 4.23. Fluid film thickness measurements and simulation results at sensor location 2.

The behavior of the slipper at sensor location two is significantly different from the measured values at sensor location one. Although both sensors are located on the inner swashplate radius within the suction stroke, at sensor one the slipper fluid film thickness rapidly increases after the slipper passes approximately half way over the sensor. Such a strong “bending” of the film thickness is difficult to be predicted by the simulation model and potentially indicates a type of contact or bending force not accounted for. The slipper behavior at sensor location two however is seemingly more stable. The forward tipping of the slipper is measured over nearly all operating conditions by approximately 5 micrometers. The same inclination is predicted by the simulation model, although the magnitude of tipping is only approximately 2-3 micrometers. It is believed that the measured average film thickness changes between operating conditions is due to fluctuations in the assembly of the swashplate and sensor.

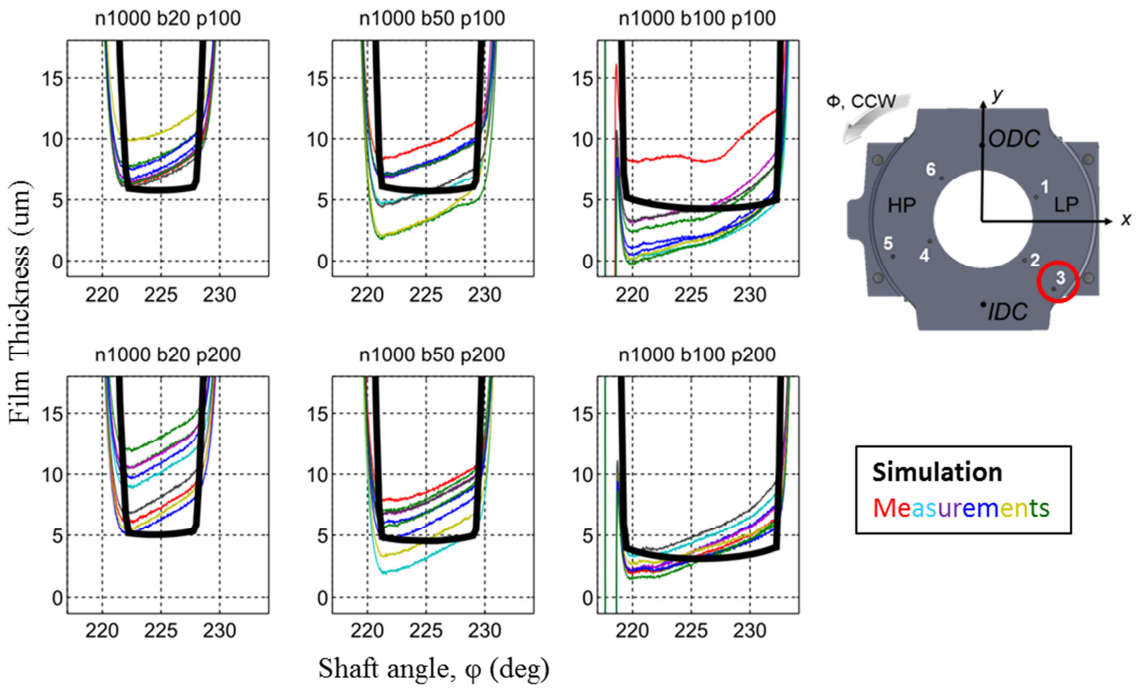

Figure 4.24. Fluid film thickness measurements and simulation results at sensor location 3.

Sensor number three is located at the outer radius of the suction stroke as opposed to the previous two sensors which were located at the inner radius. There is a larger variation in mean film thickness between the nine individual slippers passing over the sensor than at the previous sensor location. However the standard deviation of the raw acquired data for each individual slipper is near 1.5 micrometers, similar to the value reported previously in Section 4.2. The belief is that since the individual slipper standard deviation remains small, the mean film thickness differences measured are physically present. The film thickness at the outer radius is more sensitive to slipper tipping from centrifugal effects which could vary from slipper to slipper. Nevertheless, the inclination of the slipper on the leading / trailing portions of the sealing land is very repeatable between all nine slippers since the slopes of the measurements are extremely similar. The magnitude of tipping is extremely interesting as the simulation model predicts a nearly flat film

thickness at the outer edge. Because the sensor is at a fixed location in space with the slipper moving, the film thickness is acquired with a temporal variation. Thus another possible explanation to the inclined measured data is not that the slipper is more inclined but rather the outer radius of the slipper is moving away from the swashplate in time at a rate of approximately 0.5 micrometers per degree of shaft rotation. If this is true, this behavior is only possible for a portion of shaft rotation as the slipper must then transiently decrease the outer film thickness to achieve periodicity.

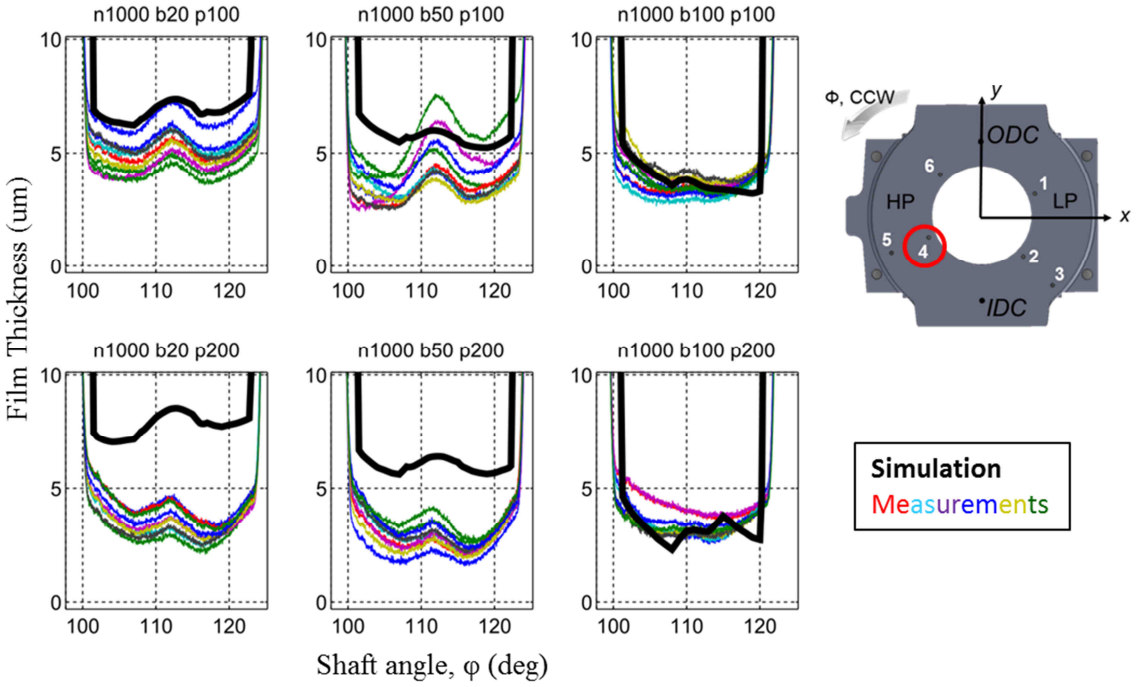

Figure 4.25. Fluid film thickness measurements and simulation results at sensor location 4.

Sensor number four is located within the high pressure pumping portion of operation. General measured behavior of the slipper in this high pressure stroke is similar to the suction stroke due to the load adaptivity of the slipper design. Larger convex deformation of the sealing lands is visible in the measurements when compared to the equivalent suction stroke sensor, number two. The simulated increase in mean film thickness as

pump displacement decreases is three to four micrometers whereas the measured slipper appears to be more stable with a change of only one to two micrometers.

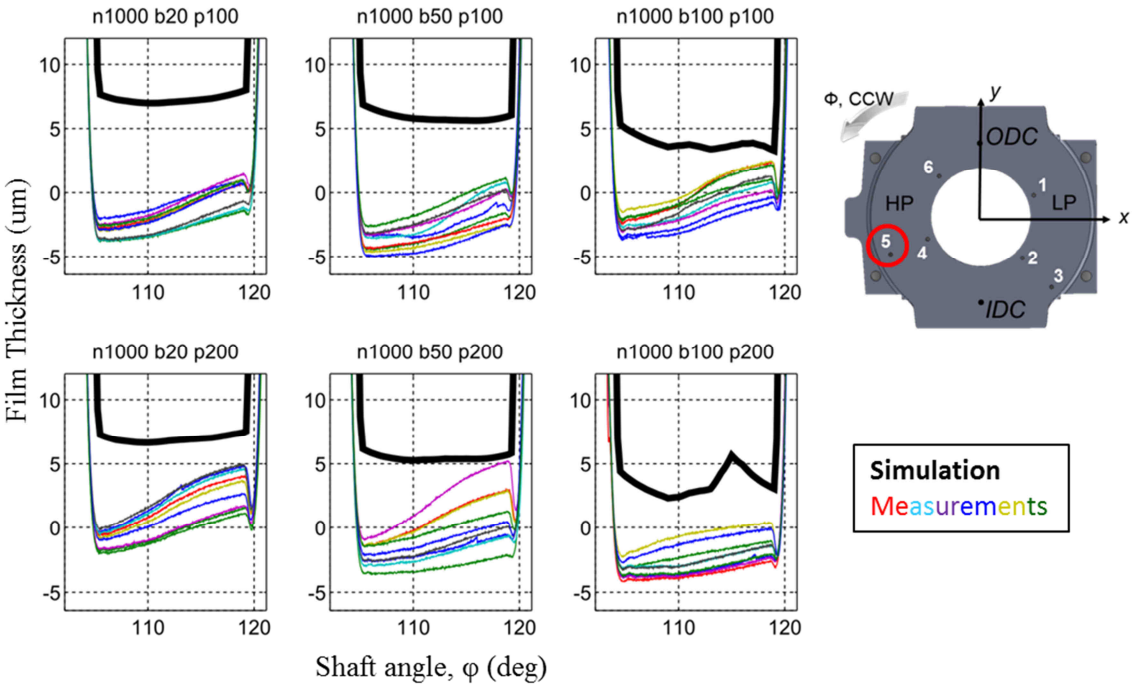

Figure 4.26. Fluid film thickness measurements and simulation results at sensor location 5.

The film thicknesses measured at sensor location number five are nearly exclusively negative in magnitude. Clearly for this location there are significant difficulties in obtaining an accurate recess depth value. Nevertheless, the measured data shows an inclination at the outer radius very similar to the profile measured at sensor number 3. Because the same film thickness slope behavior is observed at both sensor number three and five it seems less likely to be a transient increase in outer slipper thickness and rather an inclination of the slipper itself.

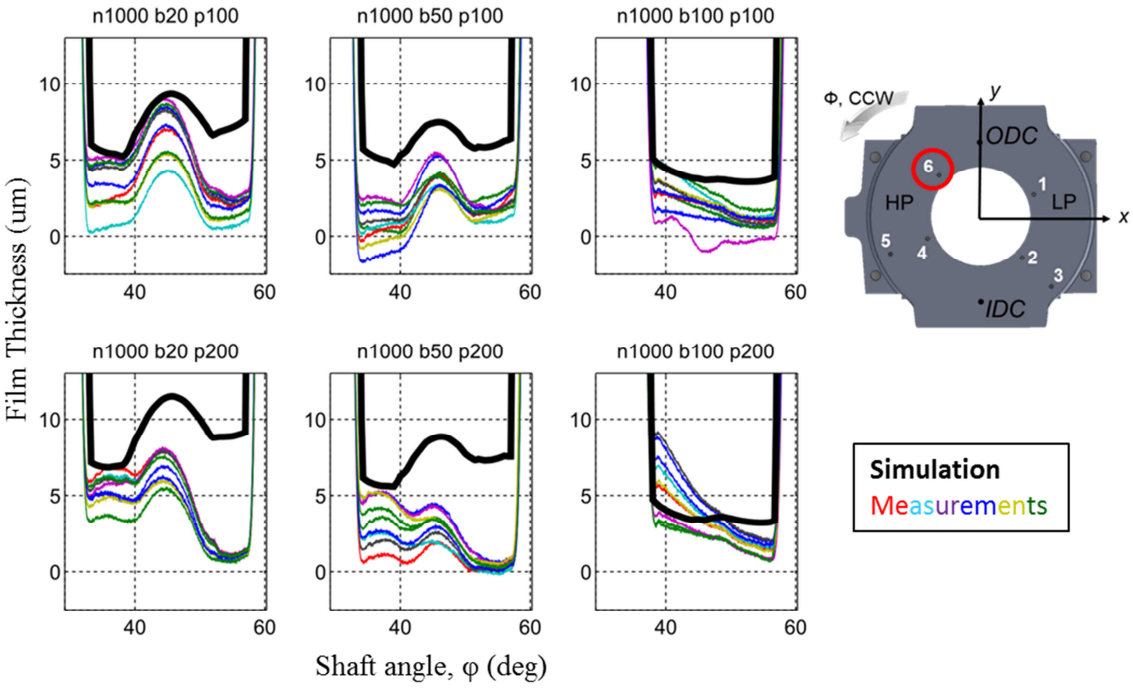

Figure 4.27. Fluid film thickness measurements and simulation results at sensor location 6.

The slipper behavior at sensor location six is similar in ways to sensor location four. What is specifically interesting is the behavior at the 200 bar operating conditions. The first part of the slipper to pass over the sensor at the 20% and 50% displacement operating conditions has a large variance between each of the nine slippers. However, the trailing land has a very tight grouping of low film thicknesses. Experimentally at the conclusion of testing, the slipper lands were worn flat without the nine micrometer pocket step. Although an increase in measured pump shaft torque compared to reference values was only measured at the 100% displacement operating condition (Table 4.5), it seems some contact was already occurring at the 200 bar, reduced displacement operating conditions to cause the measured film thickness profile to band so tightly over the trailing land.

4.8 Comparison of Measured Sensor Data to Simulations Pre and Post Wear-in

Following lapping of the swashplate surface, brand new manufactured slippers were run in the pump at four operating conditions give in Table 4.3. During this initial run in period, sensor measurements were acquired and measurement data from the very first operating condition during the run-in is compared to data acquired in the full set of steady state measurements presented in the previous section. Figure 4.28 plots the measured film thickness at 1000 rpm, 50% displacement, and a delta port pressure of 100 bar both during the initial slipper run-in and following the run-in process.

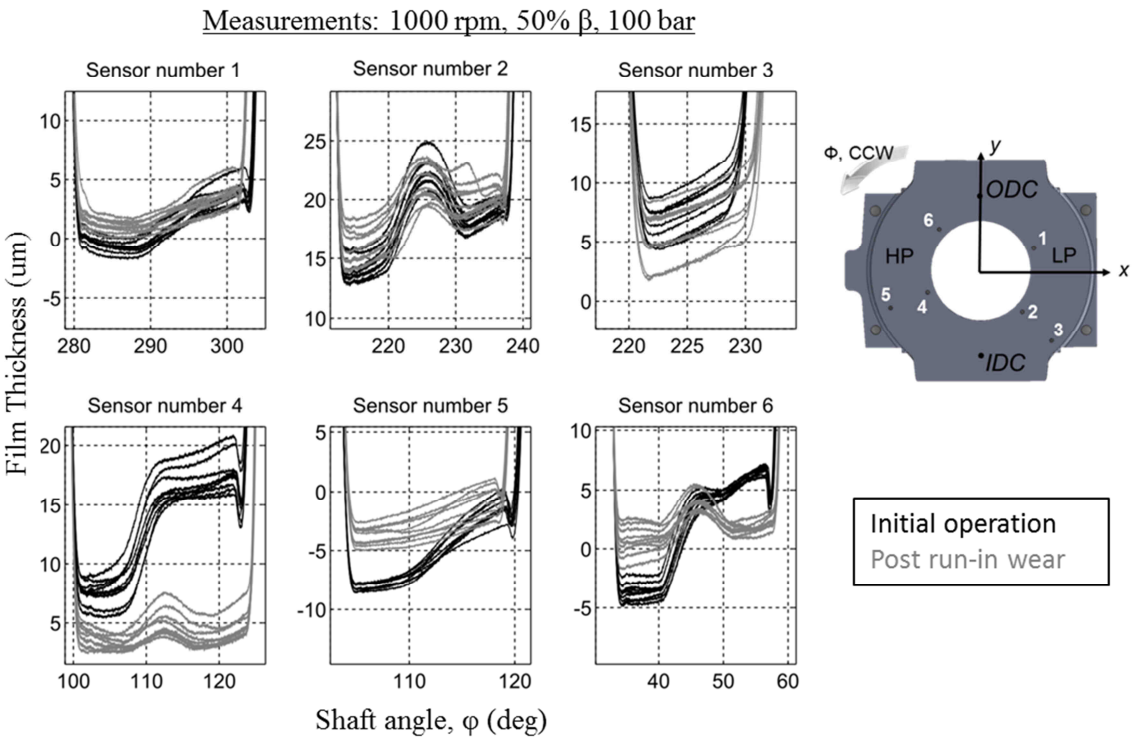

Figure 4.28. Measured film thicknesses for brand new slippers during initial operation and post run-in wear.

Following the initial slipper run-in, approximately three micrometers of wear was measured at the outer slipper radius (Figure 4.15). Inductively contact between the slipper and swashplate must occur during the initial slipper run-in operation to cause the

resulting measured wear. Only small differences in film thickness for the suction stroke sensors are measured. However, there is a clear film thickness profile change between initial operation and post run-in wear at sensor locations four and six. During the initial slipper operation, the slipper is tilted forward during the high pressure stroke which is not observed one a sloping wear is formed on the outer slipper land.

Simulations were run for the same operation condition (1000 rpm, 50% displacement, delta port pressure of 100 bar) but with a nominally flat sealing land without a wear profile and compared to simulations including the measured wear profile. The simulation results are converted to an equivalent sensor measurement format and plotted in Figure 4.29.

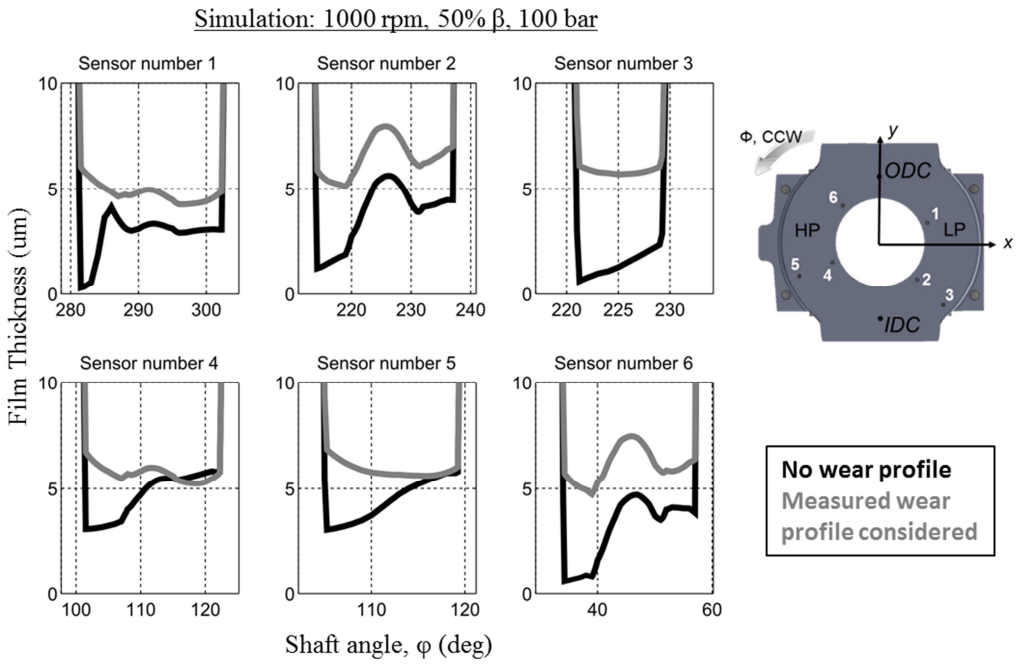

Figure 4.29. Simulation results neglecting and including the measured post run-in wear profile.

Simulation results for both sensors four and six show the change in film thickness behavior when wear is excluded and then considered as was observed in the experimental

measurement. The magnitude of the step predicted in simulation was only 3-4 micrometers whereas the measured step height was 8-10 micrometers. The main aim of the numerical lubrication model is to predict slipper performance during normal full film operation, not precisely predicting the slipper orientation when significant contact is occurring such as during initial wear-in. Thus the model is able to successfully predict the presence / absence of swashplate contact with good correlation to the measured behavior, although the absolute magnitude of slipper micro-position does not match during contact since it is not the models focus.

The simulation model offers additional insight into why the observed wear dependent behavior occurs. Figure 4.30 provides a generic illustrative example of the simulation results with the fluid film exaggerated to provide orientation for the following simulation results. The predicted fluid film thickness under the slipper both assuming a normally flat land and including measure wear is illustrated in Figure 4.31.

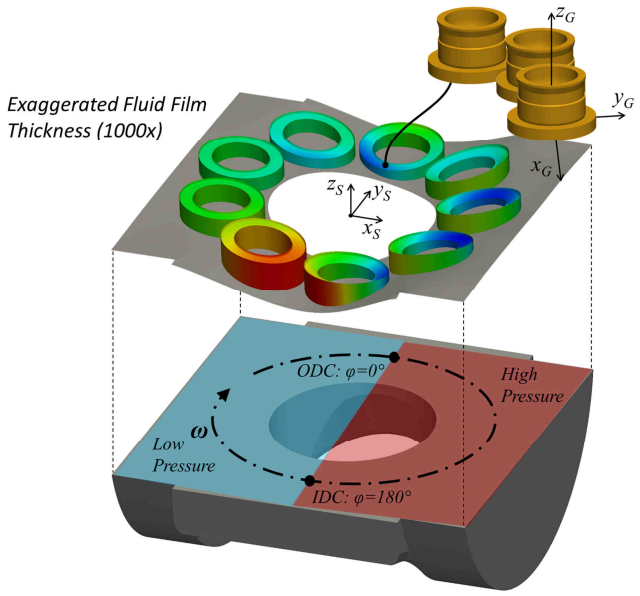

Figure 4.30. Graphical illustration of the exaggerated slipper lubricating fluid film simulation result with reference systems.

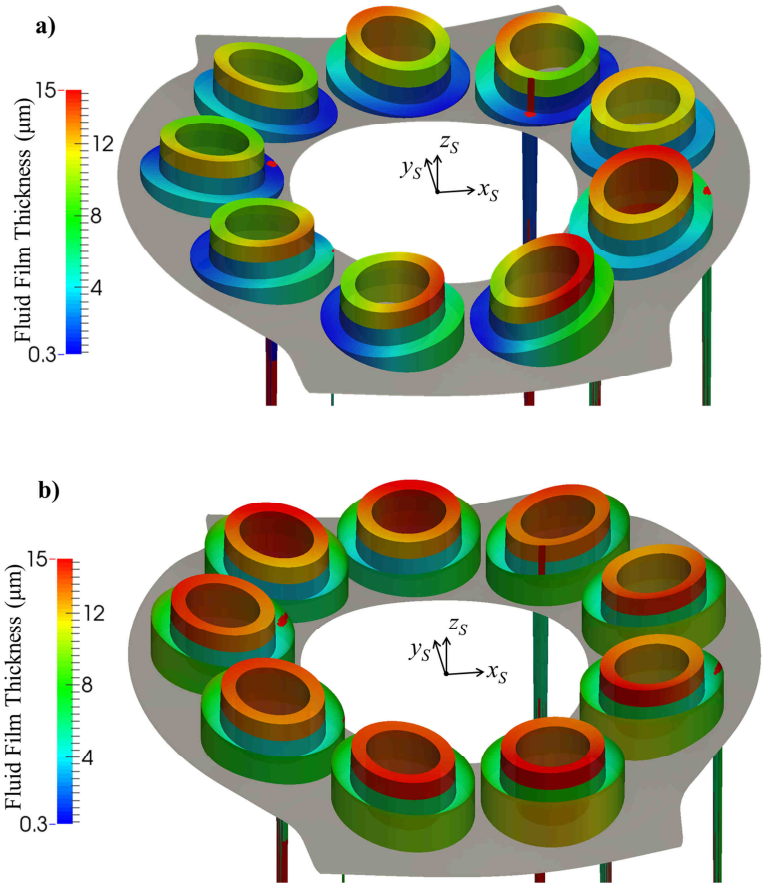

Figure 4.31. Simulation results of slipper fluid film thickness at n = 1000 rpm, β = 50%, Δp = 100 bar for a) nominally flat slipper sealing lands b) measured slipper land wear.

It is clear from these simulation results the slipper tips forward without wear on the outer radius of the sealing land. The reason for the tipping is easier to see in a cross section of the slipper film taken in the x-z plane of the slipper coordinate system as illustrated in Figure 4.32. In these cross sections, the slipper is on top of the fluid moving in the positive x-axis direction. The 9 micrometer step actually acts as a hydrodynamic step bearing causing a pressure generation on the trailing half of the slipper, tipping it forward. This in turn causes contact with the swashplate on the leading slipper edge and the resulting wear on the outer slipper radius. In the second simulation with the wear profile included, the wear on the leading land acts as a slider bearing generating hydrodynamic

pressure. This pressure generation on the leading half of the slipper counteracts the hydrodynamic pressure generation in the step on the trailing half of the slipper preventing tipping and enabling a full film operation.

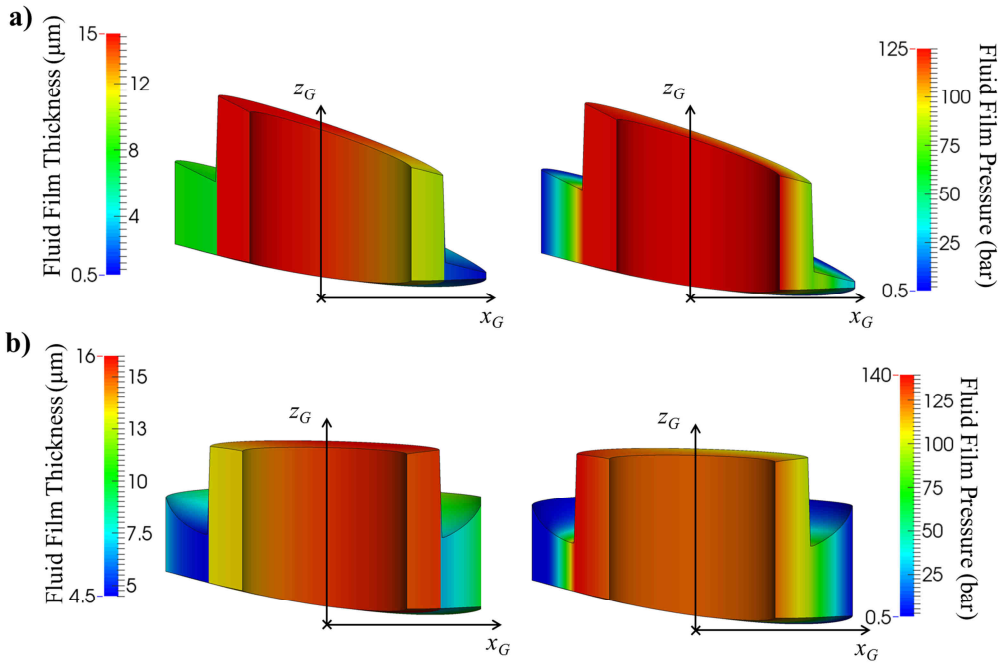

Figure 4.32. Simulation results of slipper fluid film cross section at n = 1000 rpm, β = 50%, Δp = 100 bar for a) nominally flat slipper sealing lands b) measured slipper land wear.

4.9 Original Contributions

Previous researchers used indirect measurements such as temperature, pressure, force, or strain sensors to measure the tribological conditions within operational axial piston hydraulic pumps. Frequently however the measurements were made for other sliding interfaces within a piston pump: either the cylinder block / valve plate or piston / bore interface. Direct measurements using fluid film thickness displacement transducers within axial piston machines have been used at the cylinder block / valve plate interface and slipper / swashplate interface. However the cylinder block / valve plate measurement

did not directly measure the fluid film and the slipper / swashplate test necessitated significant modifications to the pump design.

Pushing the boundaries of previous experimental testing, this research aspired to directly measure the fluid film height within the lubricating regime at high speed to capture fast moving slippers. This goal was achieved using state of the art miniaturized inductive sensors in an otherwise nearly unmodified axial piston machine. Lubrication behavior changes between operating conditions and during the component run-in process were experimentally measured.

Lubrication fluid film thickness represents the greatest unknown variable affecting slipper performance. Other physical quantities such as temperature and friction have an averaging quality either temporally or spatially. Therefore attempting to measure and correlate point film thickness poses the greatest challenge. In spite of this difficulty, correlation was achieved between measured and simulated slipper behavior. The numerical model was able to predict the hydrodynamic effects of micro design features within the sealing land and the contribution of this design feature wear.

CHAPTER 5. CASE STUDIES: VIRTUAL SLIPPER TESTING AND DESIGN MODIFICATIONS

5.1 Impact of Pump Operating Conditions

The same slipper design used in the experimental testing from the previous section was simulated at four different pumping-mode operating conditions by varying pump shaft speed and working port pressures, selected for the following reasons: a low pressure, high shaft speed operating condition will promote slipper lift away from the swashplate. Conversely, a low speed, high pressure operating condition will often exhibit the lowest film thicknesses in underbalanced slipper designs due to the reduced hydrodynamic pressure generation ability. A high speed, high pressure operating condition represents the peak power of an axial piston unit, and a medium speed, medium port pressure serves as a good comparison point.

Hydrostatically due to the unique stepped sealing land design, the slipper is significantly overbalanced if it is resting on the swashplate surface. This is due to the sealing land step which would become pressurized to nearly the same pocket pressure. However, as the film thickness between the swashplate and the true sealing land increases, the pressure in the step region will transition to more of the logarithmic hydrostatic distribution. This transition between constant and logarithmic hydrostatic pressure enables a load adaptive design without using a traditional orifice restrictor.

However, the addition of a small step in the sealing land introduces a source for hydrodynamic pressure generation / reduction on the trailing and leading lands respectively which cannot realistically be evaluated analytically. Therefore, using the developed model, the thin film pressure distributions for the previously described four different operating conditions are presented in Figure 5.1. The fluid film thicknesses and deformations are exaggerated 1000 times to enable appropriate visualization with the hidden slippers bodies moving in a clockwise direction.

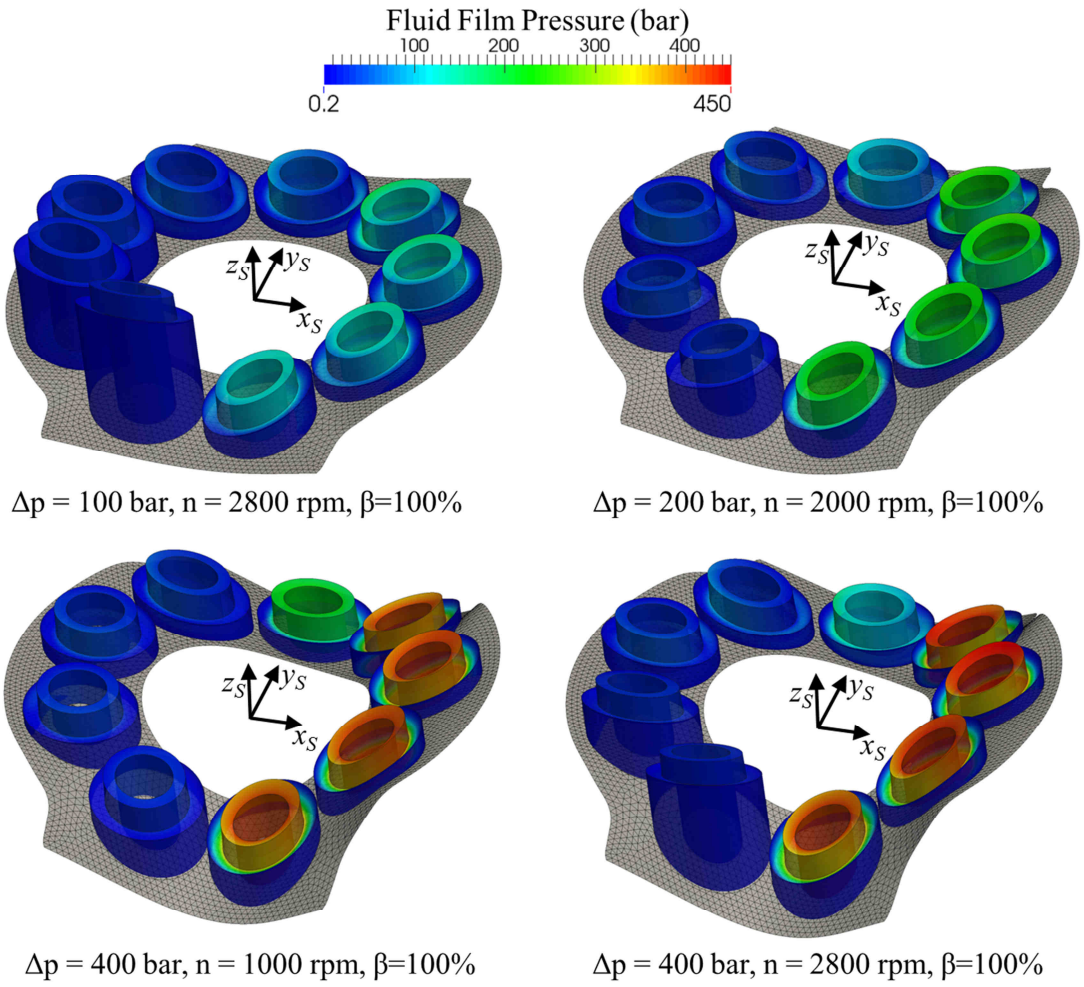

Figure 5.1. Thin film slipper pressure distributions at four operating conditions.

As defined earlier, the high pressure discharge stroke occurs in the positive x_S axis. Because a common pressure scale is used in comparing the different operation conditions, the boundary pressure distribution changes from the pocket are the most evident. Using a low pressure, high speed operating to best highlight the hydrodynamics effects, a cross section an individual slipper fluid film is illustrated in Figure 5.2.

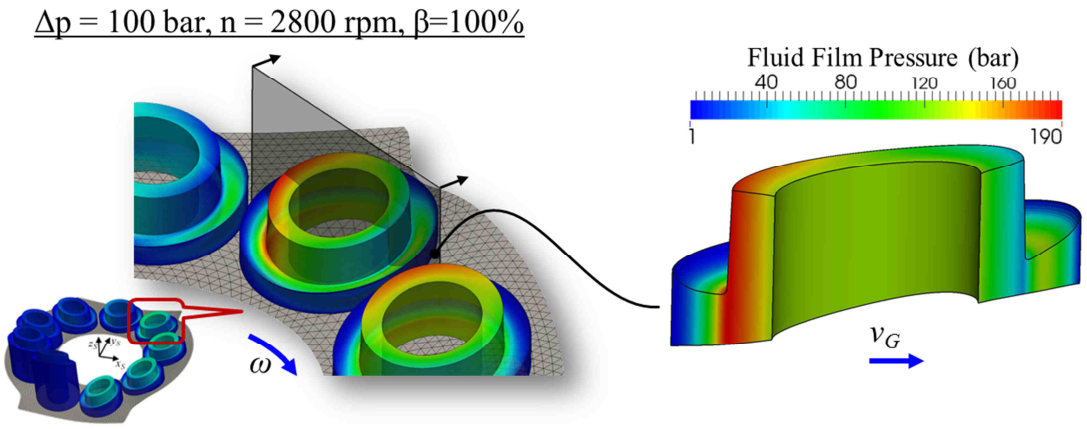

Figure 5.2. Detailed view of slipper pressure distribution at φ = 40°.

In this cross section view, the top slipper surface is moving towards the right. There is nearly 70 bar of hydrodynamic pressure generation on the trailing land due to the step. The pressure moment on the trailing edge must be balanced by the leading land that is accomplished due to both the convex elastohydrodynamic pressure deformation of the slipper lands as well initial run in wear.

The fluid film thickness between the slipper and swashplate for the four same operating conditions is illustrated in Figure 5.3. Interesting differences in slipper operation between the different operation conditions can be observed.

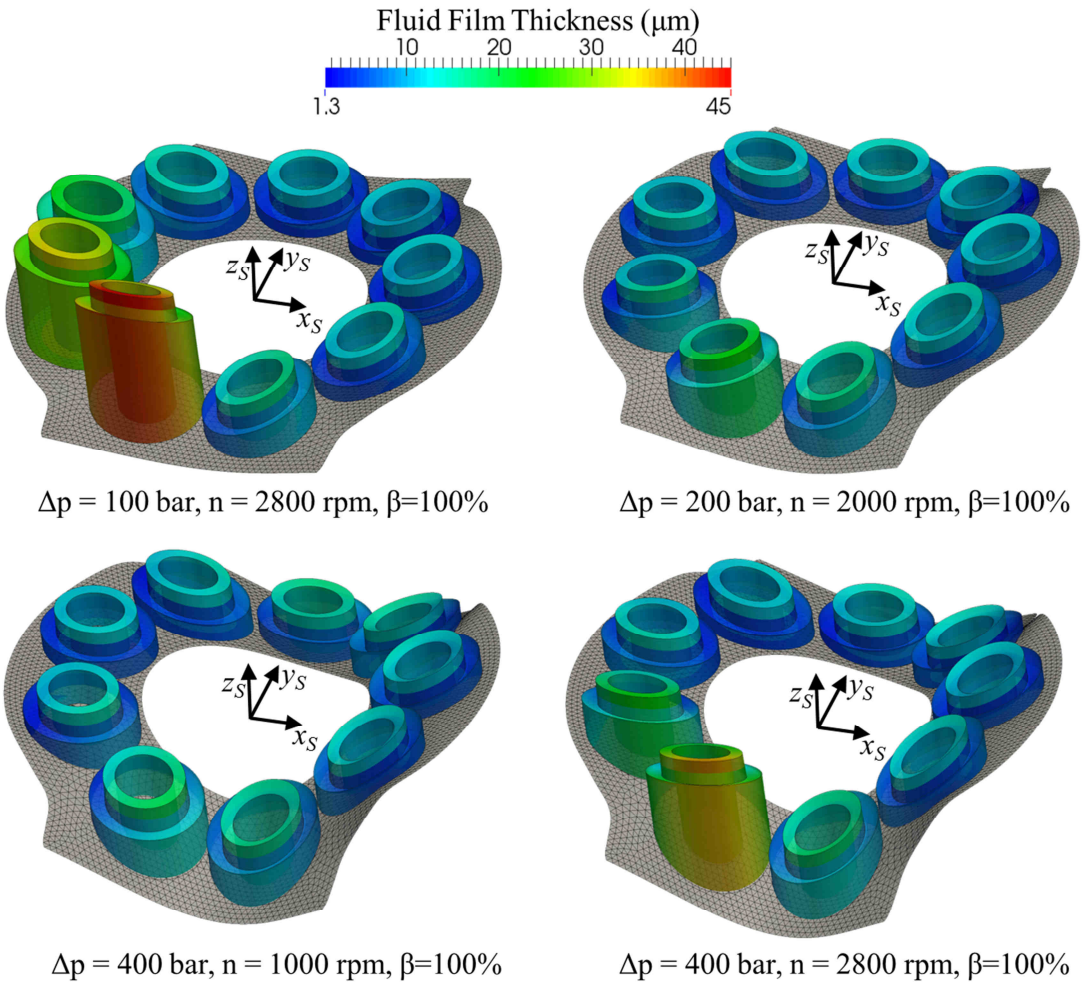

Figure 5.3. Slipper thin film thickness for a 130 cc/rev axial piston unit.

The pressure force from the displacement chamber pressing on the piston and the slipper pocket / fluid film pressure are the two largest load variations over a single shaft revolution with changes occurring at y_S axis. However, the inertia force (F_{aK}) coming from the reciprocation of the piston and slipper pair varies sinusoidal with the greatest magnitude pulling the slipper away from the swashplate at φ = 180°. The magnitude of the inertia force increases with the square of pump shaft speed. During the high pressure stroke, a very small change in fluid film thickness can create the necessary change in the slipper fluid pressure to offset the inertia force. However, during the low pressure stroke,

a much larger film thickness change is required, and thus the impact of inertia force on slipper lift is best observed just after transition into the suction stroke. At 1000 rpm there is little slipper lift, or increase in fluid film thickness. Slightly more slipper lift occurs at 2000 rpm. However, as the pump shaft speed increases to 2800 rpm, a significant slipper liftoff is observed. What prevents the slipper from lifting any further is a combination of a decreasing impact of the slipper step and even a pocket pressure reduction due to the piston and slipper orifice. The slipper pressure distribution at φ = 200° and a comparison between pocket and displacement chamber pressure is plotted in Figure 5.4. At this large mean film thickness, the pressure distribution in the sealing land is not significantly altered by the micrometer step because the overall film thickness is much larger. Thus, a nearly symmetric hydrostatic pressure distribution is observed over the entire sealing land. Moreover, because of the large film thickness, a single slipper is instantaneously leaking over 0.5 l/min at φ = 200°. Even though the piston and slipper restrictions are larger in this stepped slipper design, with such a large flow rate a slipper pocket pressure loss is encountered as illustrated on the right of Figure 5.4. This reduction in slipper pocket pressure finally allows the net clamping force from the piston head (F_{SK}) to balance the slipper pocket / land pressure force.

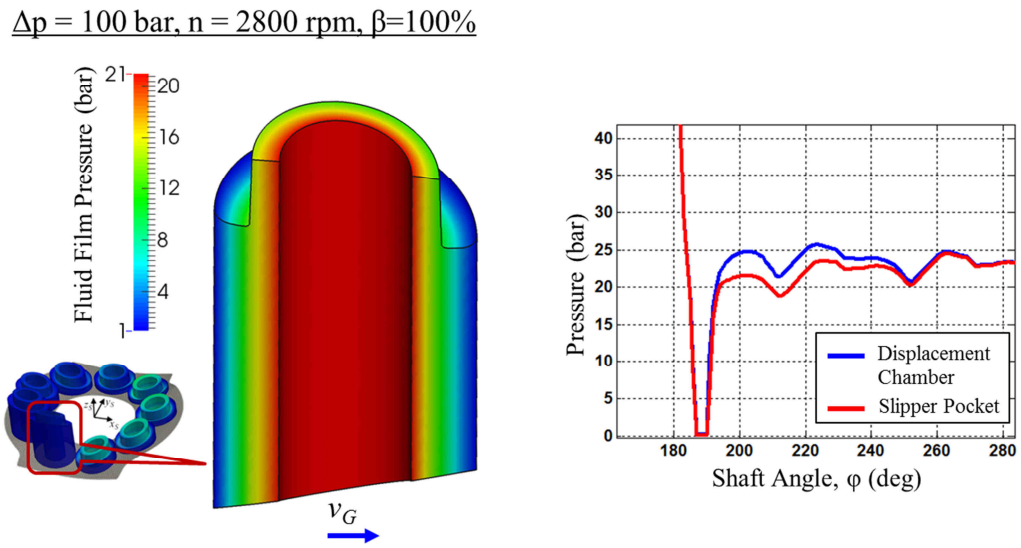

Figure 5.4. Slipper load adaptive elements limiting slipper lift off.

Referring back to Figure 5.3, the micro-motion of the slipper generally is such that a larger film thickness results radially outwards with respect to the pump shaft. This effect is pronounced at higher shaft speeds and during the suction stroke. This radial tipping comes from the moment $M_{\omega G}$ which is created by the centrifugal force acting on the slipper center of mass. The slipper tilts radially such that a larger hydrodynamic pressure force can be generated on the inner radial edge of the sealing land to oppose the moment. For the same reason as the changing inertia force, this effect is most pronounced during the suction stroke. However, unlike the inertia force, the tipping moment remains constant over a shaft revolution.

The model is not only able to generate three dimensional results, but also quantitative results of slipper lubrication performance. For these same four operation conditions, quantitative results of total slipper case leakage, the torque generation from viscous friction, and the resulting summation of power loss are presented in Table 5.1.

Table 5.1. Quantitative summary of slipper lubrication performance for a 130 cc/rev axial piston pump.

	Slipper Leakage (L/min)	Slipper Torque Loss (Nm)	Total Slipper Power Loss (W)
Δp=100 bar, n=2800 rpm, β=100%	1.2	3.4	1113
Δp=200 bar, n=2000 rpm, β=100%	0.5	3.8	922
Δp=400 bar, n=1000 rpm, β=100%	0.6	2.1	611
Δp=400 bar, n=2800 rpm, β=100%	1.5	3.4	1657

The trends of increasing or decreasing leakage and torque loss are clearly explainable by comparing the predicted slipper film thicknesses in Figure 5.3 as well as the changing in pump port pressure and shaft speed.

5.2 Impact of a Bi-metal Slipper Design

Many slippers designs are constructed of a uniform isotropic material, commonly bronze. Because the slippers are rotating quickly in the pump housing full of oil with nearly axisymmetric heat generation from the lubricating film, there are not normally large magnitudes of non-uniform thermal deformation across the sealing lands. However, in this case study a male slipper design is not made of a uniform material, but instead a bimetal construction of primarily steel with a thin bronze coating as illustrated in Figure 5.5.

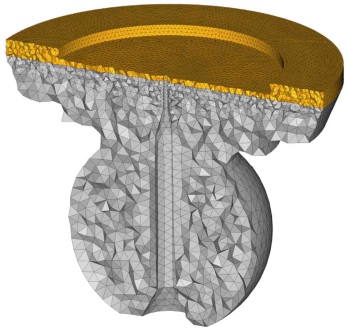

Figure 5.5. Slipper bi-metal construction.

The necessity for a predominately steel construction comes mainly from the male slipper design. The male design results in a smaller neck region between the ball-socket interface and the sealing land reducing the overall bending stiffness. The reduction in bending stiffness results in especially large convex slipper pressure deformation leading to a weakening of the pressure film and significant wear. To mitigate this larger pressure deformation, the slipper is constructed primarily of steel, which with a greater elastic modulus will reduce the pressure deformation compared to an all bronze design. Although the desire is to use exclusively steel for the slipper construction, the swashplate is also a steel construction. Steel on steel tribological pairing is not desirable during instances of mixed or boundary lubrication such as machine startup or at low speeds. To achieve a stiff slipper design while simultaneously maintaining a bronze-steel paring between the slipper and swashplate, the solution is to apply an approximately 1 mm thick bronze coating to the bottom of the steel slipper construction. Although this design reduces pressure deformation, because of the mismatch in thermal expansion coefficients between steel and bronze, a significantly greater thermal deformation is introduced. The same thermal loads taken from a full lubrication simulation are applied to the bronze coated slipper, and an identically meshed slipper, but with steel material properties applied uniformly to all solid elements. The comparison of thermal deformations between these two slippers designs is illustrated in Figure 5.6. The bronze coated slipper exhibits nearly 2 micrometers of thermal deflection across the slipper fluid film lands, while the same slipper under the same thermal loads but with exclusively steel material properties exhibits nearly no relative thermal deflection. The difference is exclusively because of

the greater thermal deflection of bronze compared to steel. The fluid thickness simulation results for the actual bi-metal slipper design are presented in Figure 5.7.

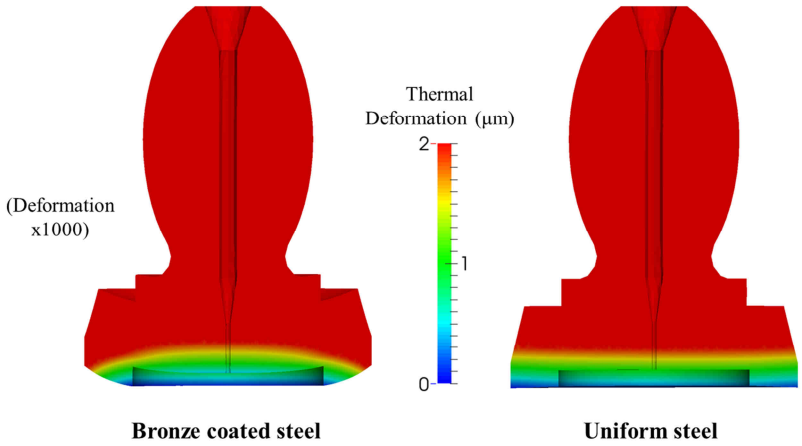

Figure 5.6. Comparison of a steel and a bronze-coated steel slipper under the same thermal loading.

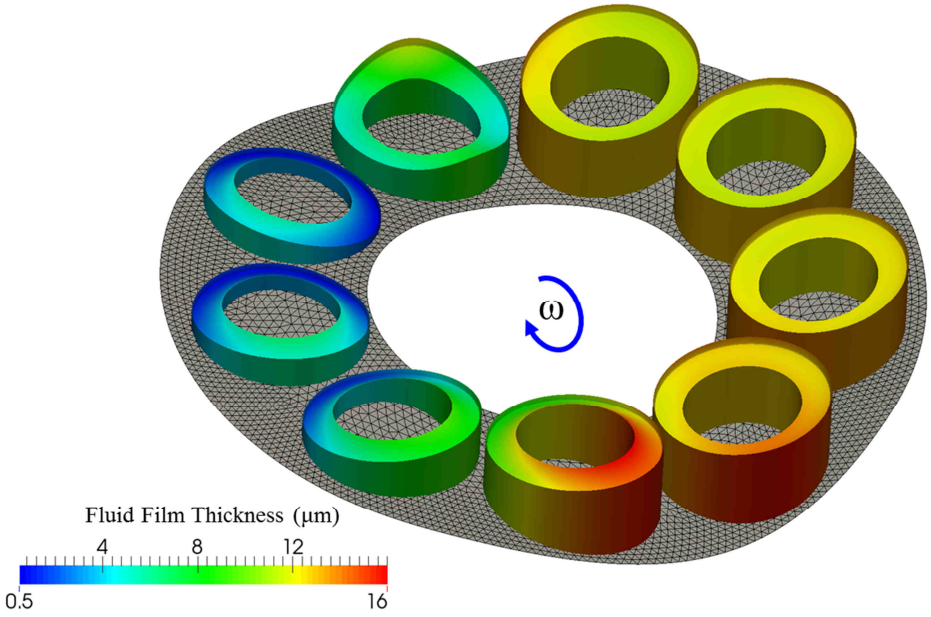

Figure 5.7. Fluid film thickness for an axial piston hydraulic unit at Δp = 200 bar, n = 1000 rpm, β = 100%.

5.3 Multi-land Slipper Design

Although the most common slipper design features a single slipper land, a vented multi land design is also popular. This case study will examine the impact of varying the multi-land design parameters on slipper operation. Figure 5.8 illustrates the primary design parameters of a multi land slipper. Because the outer slipper diameter is typically fixed by maximizing the diameter which prevents contact between neighboring slippers, the outer slipper diameter is held constant. With the outer diameter constant, if five parameters are used to describe the three lands and two grooves, the slipper inner diameter (d_{inG}) is constrained by:

$$d_{inG} = d_{outG} - land1 - groove1 - land2 - groove2 - land3 \tag{5.1}$$

Therefore, a total of six slipper design parameters remain for this design study example. This particular design is a vented slipper with grooves connecting groove 1 to the pocket and groove 2 to the case as illustrated in Figure 5.9.

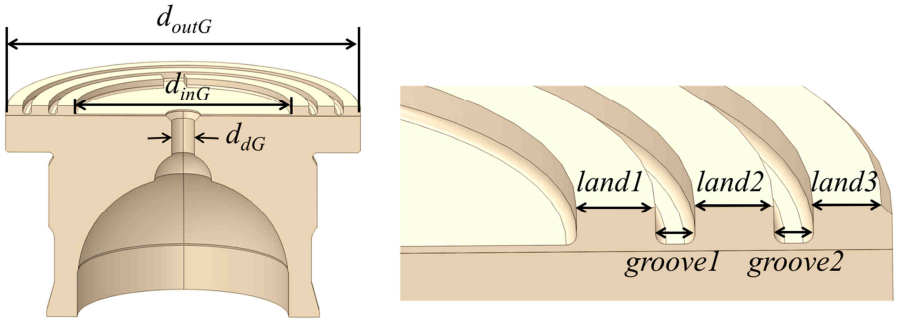

Figure 5.8. Primary design parameters for a typical multi land slipper.

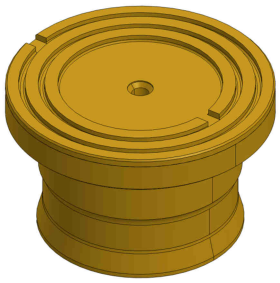

Figure 5.9. Illustration of slipper radial grooves.

With six variables the design space becomes quite large for any reasonable number of interval discretization. For example, Table 5.2 lists the desired full factorial combinations for a total of 38400 designs. Assuming an average simulation time of 18 hours there is simply too much computational effort required to complete such a full factorial design.

Table 5.2. Example full factorial multi-land slipper design variations.

Full Factorial Variations	
d_{dG}	0.5 to 1.0mm by 0.25mm
land1	1.0 to 1.7mm by 0.1mm
groove1	0.5 to 0.9mm by 0.1mm
land2	1.0 to 1.7mm by 0.1mm
groove2	0.5 to 0.9mm by 0.1mm
land3	1.0 to 1.7mm by 0.1mm

An alternative to full factorial design of experiment (DOE) studies are techniques including:

- Fractional factorial designs
- Central composite design
- Latin Hypercube sampling

For this case study, the popular Latin Hypercube Sampling (LHS) method is utilized because the sample population is able to be independent of domain size as well as the

methods inherent space filling properties (Tang, 1993). A sample size of 75 was selected to limit the total computational effort with the same variable ranges as given in Table 5.2. The scatter distribution of each design variable is plotted for the population of 75 designs in Figure 5.10. This illustration highlights the space-filling feature of the LHS methodology.

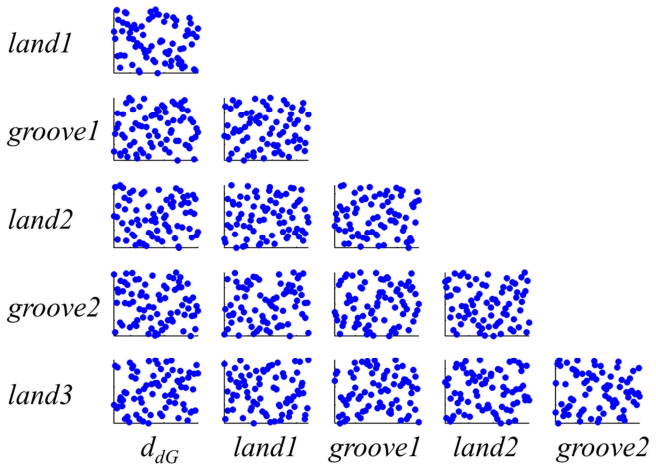

Figure 5.10. The Latin Hypercube population for the multi-land slipper design study.

Simulations were run for each of the slipper designs at one moderate operating condition of n = 2000 rpm, β = 50%, Δp = 200 bar. A simplification was made by inter/extrapolating a single set of influence matrices used for deformation calculation instead of recalculating a new influence matrix set for each design. Additionally, for a more complete design study, other operating conditions should also be simulated and included.

The total simulated slipper power loss for each of the slipper designs is plotted against each of the design variables in Figure 5.11. It is nearly impossible to extract any useful trends from this data due to the nature of the LHS sample set. Although the designs are

space filling, all parameters are being change simultaneously making it difficult to extract single variable trends.

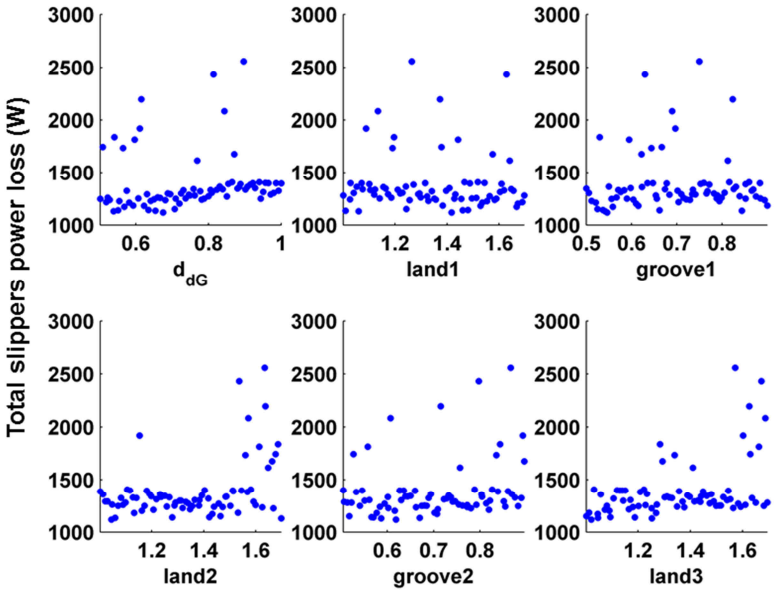

Figure 5.11. Total multi-land slipper power loss variation as a function of design variable.

To extract trend information from the data, a technique termed surrogate modeling will be employed. The premise of surrogate, or black box, modeling is to train a simple generic mathematical model using a set of known data. The surrogate model is computationally cheap to evaluate and can be used to subsequently evaluate the impact of a single variable on slipper performance while holding other parameters constant. A number of surrogate modeling techniques exist, but this case study will utilize the Ordinary Kriging method. Kriging is a type of linear least squares estimator algorithm (Sakata, 2003; Emery, 2005). The Kriging estimator predicts the function value, $f(x^*)$, at an unknown location, x^*, based on the value of the function at known locations, x_i with the linear combination:

$$f\left(x^*\right)=\sum w_i f\left(x_i\right) \quad \text{where } \sum w_i = 1 \tag{5.2}$$

To solve for the Kriging weights, *w*, in Eq. (5.2) the following system must be solved:

$$\begin{bmatrix} \gamma(x_0,x_0) & \gamma(x_0,x_1) & \cdots & \gamma(x_0,x_n) & 1 \\ \gamma(x_1,x_0) & \gamma(x_1,x_1) & \cdots & \gamma(x_1,x_n) & 1 \\ \vdots & \vdots & \ddots & \vdots & \vdots \\ \gamma(x_n,x_0) & \gamma(x_n,x_1) & \cdots & \gamma(x_n,x_n) & 1 \\ 1 & 1 & \cdots & 1 & 0 \end{bmatrix} \begin{bmatrix} w_0 \\ w_1 \\ \vdots \\ w_n \\ \lambda \end{bmatrix} = \begin{bmatrix} \gamma(x_0,x^*) \\ \gamma(x_1,x^*) \\ \vdots \\ \gamma(x_n,x^*) \\ 1 \end{bmatrix} \tag{5.3}$$

where x is the design vector, γ is the variogram function, and λ is a slack variable used to enforce the constraint on w. A variogram function is used to describe the spatial dependence of the approximated function. In this work, the Gaussian variogram model was used where:

$$\gamma(x_a,x_b)=s_v\cdot\left(1-\exp\left(\frac{-\|x_a-x_b\|^2}{r_v^{\,2}}\right)\right) \tag{5.4}$$

The parameters, s_v and r_v used in Eq. (5.4) are determined using a least squares curve fit of the model Gaussian variogram to the experimental variogram data (Cressie, 1985). It is important to note that the design variables were linearly normalized before the Kriging model was built. This is important because of the l^2 vector norm used by the variogram model in Eq. (5.4). Further details regarding the implementation of a Kriging surrogate model using an underlying physical model can be found in Schenk and Ivantysynova (2011b).

While each design variable is varied, the other variables will be held fixed at a reference design with values given in Table 5.3.

Table 5.3. Reference multi-land slipper design variables.

d_{dG}	0.7	mm
land1	1.4	mm
groove1	0.8	mm
land2	1.4	mm
groove2	0.8	mm
land3	1.4	mm

Because the slipper outer diameter is held constant, as some design variables are changed the analytical slipper hydrostatic balance factor will change. Both the total slipper power loss prediction from the Kriging model as well as the change in hydrostatic balance factor are plotted in Figure 5.12. Changes in the slipper orifice as well as land1 and groove1 do not change the hydrostatic balance factor as the inner and outer radiuses of the sealing land remain constant. However as the width of land2, groove2, and land3 change the radiuses of the sealing land change as well. Interestingly, due to the outer slipper diameter constraint, as the width of land2, groove2, and land3 increase the main slipper pocket becomes smaller reducing the effective hydrostatic balance.

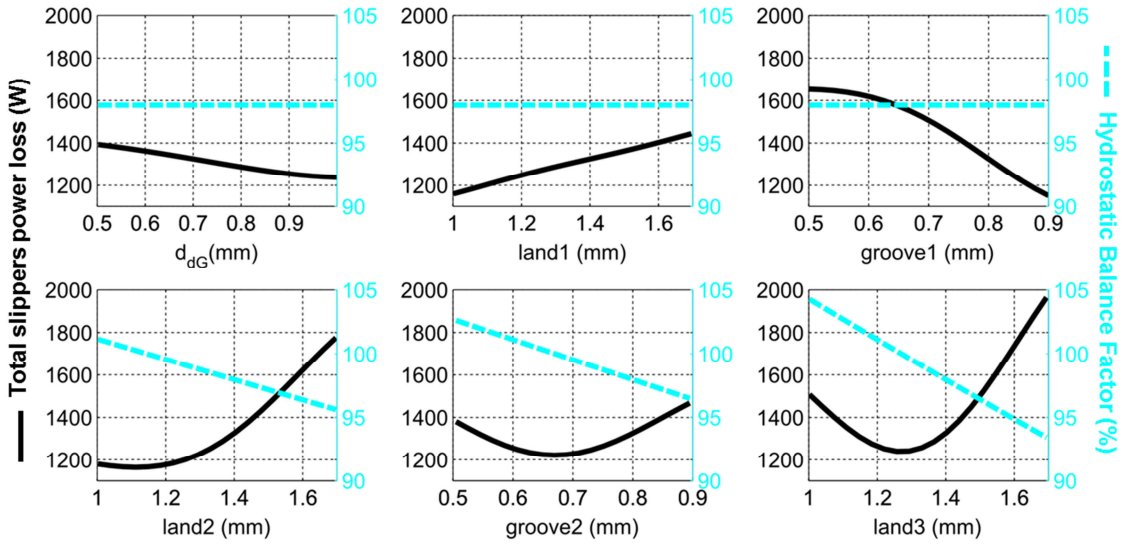

Figure 5.12. Total slippers power loss as a function of individual multi-land design parameter changes using a surrogate model.

To better understand the reason for the power loss trends observed in Figure 5.12, it is helpful to look at the primary sources individually: total slippers leakage in Figure 5.13 and shaft torque loss in Figure 5.14. There is little change in predicted leakage as the width of land1 and groove1 increase. This intuitively makes sense as the balance factor is not changing and the sealing land is remaining at the same width. However as the width of land1 increases, the shaft torque coming from viscous friction increases due to an increase in total slipper land area. As the width of groove1 increases, the center radius of land1 decreases to maintain the same outer slipper diameter. Although the width of land1 remains the constant, since the center radius decreases the total slipper land area decreases in turn reducing the shaft torque loss.

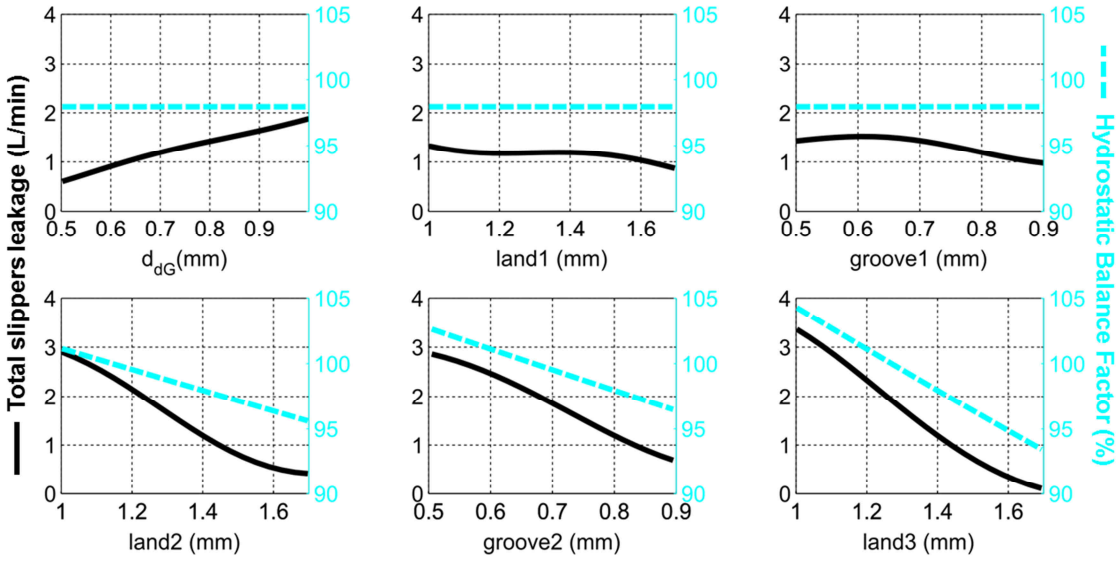

Figure 5.13. Total slippers leakage as a function of individual multi-land design parameter changes using a surrogate model.

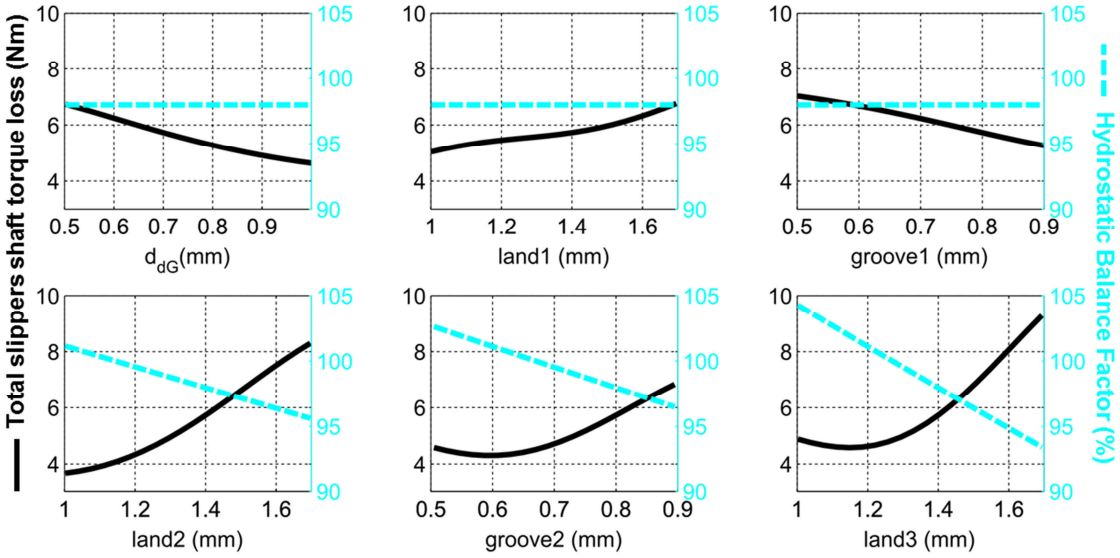

Figure 5.14. Total slippers shaft torque loss as a function of individual multi-land design parameter changes using a surrogate model.

The sealing land (land2), groove2, and outer stabilizing land (land3) dimensions all alter the hydrostatic balance factor as their dimension is changed. In all cases as the balance factor decreases the leakage decreases while the torque loss increases. A balance between

these two inversely proportional losses is needed to minimize power loss. This case study only focuses on one operating condition, but if the working pressure and shaft speed can vary significantly, achieving a balance between leakage and torque loss becomes problematic. As working pressure increases flow losses become dominate, whereas at high speeds and low pressures friction losses dominate instead.

The slipper orifice diameter will never affect the balance factor, but becomes important in limiting slipper lift, especially at higher speeds and larger hydrostatic balance design ratios. As the slipper orifice diameter increases, there is less flow restriction between the displacement chamber and the slipper pocket. Reduced flow restriction allows for a slightly higher pocket pressure, lifting the slipper further away from the swashplate. In Figure 5.13, as the slipper lifts away from the swashplate, the leakage increases while the shaft torque decrease.

At higher initial leakage flow rates, decreasing orifice diameter will have a larger impact on total leakage reduction. This is shown in Figure 5.15 which varies the orifice diameter at five different land3 diameters. As the outer land width increases, the hydrostatic balance ratio decreases reducing the leakage flow. When the total leakage magnitude is reduced, further reductions in slipper orifice diameter have little impact on leakage. Upon inspection of Figure 5.15 the surrogate model predicts a negative leakage for the 1.7mm land3 design with a small orifice. This highlights a limit of surrogate modeling a complex physical problem with a sparse data set; although the trends displayed in Figure 5.15 are representative of results from the full physics-based numerical model, especially near domain boundaries, the surrogate model miss-predicts absolute magnitudes.

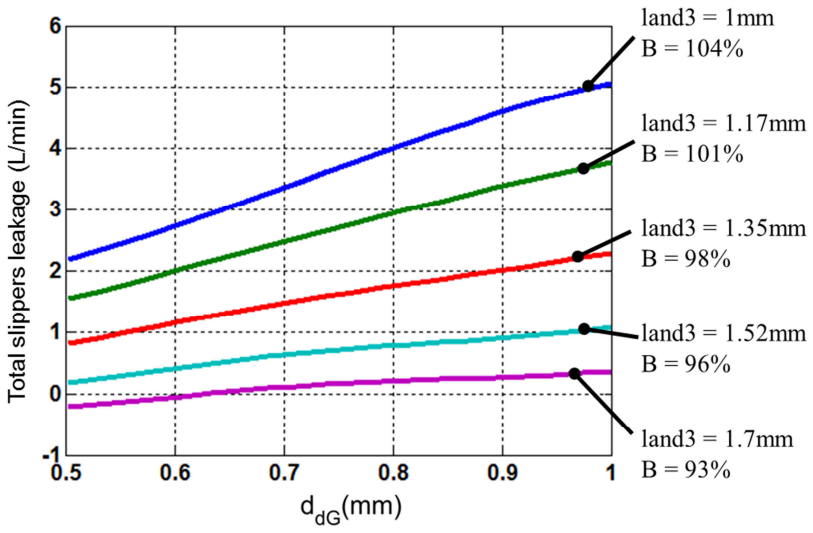

Figure 5.15. Impact of slipper orifice diameter on total slippers leakage for different outer stabilizing land widths.

It is interesting to investigate how the slipper performance behavior will change as the slipper land widths are changed, but while holding the hydrostatic balance factor constant. To achieve this while simultaneously maintaining the same slipper outer diameter the width of land1 and land3 will vary, with land2 set to achieve the same balance factor of 98%. The other slipper dimensions are held constant with values given in Table 5.3. Figure 5.16 plots the total slippers power loss as a function of the width of land1 and land3 as well as the resulting width of land2 needed to maintain the 98% hydrostatic balance ratio. Notice that while land1 varies over the full domain, land3 is limited to approximately 1.25mm to 1.6mm. This range is limited to ensure the width of land2 needed to maintain the balance ratio stays within the 1.0mm to 1.7mm simulated range.

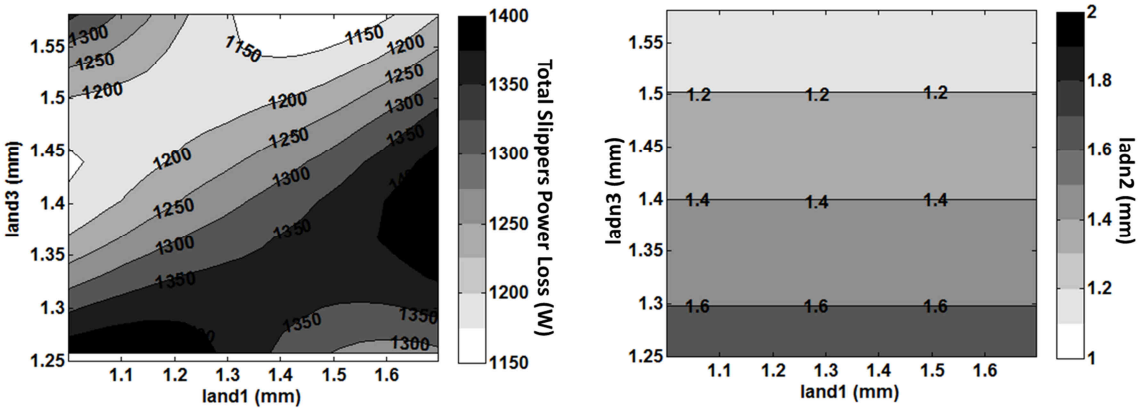

Figure 5.16. Total slippers power loss (left) and sealing land width (right) as a function of inner and outer slipper land variation while maintaining a 98% hydrostatic balance ratio.

Interestingly, the trend of Figure 5.16 indicates that power loss decreases as land3 increases in width. This is quite different than in Figure 5.12 where the power loss is at a minimum when the width of land3 is at 1.3mm, increasing either as the land width grows or shrinks. However, in Figure 5.12 the hydrostatic balance ratio is decreasing as the width of land3 increases which is not the case for Figure 5.16. To better understand this trend difference, Figure 5.17 plots slippers leakage and torque loss over the same land variations. As the width of land3 increases, the width of land2 is forced to decrease in order to maintain the same balance ratio as shown in Figure 5.16. A decrease in sealing land width leads to the higher leakages predicted. However the width of land2 is forced to decrease in size faster than the width of land3 increases. The net effect of this is the total slipper land area decreases as the width of land3 increases as shown in Figure 5.18. The reduction in total land area reduces the viscous friction and thus shaft torque loss.

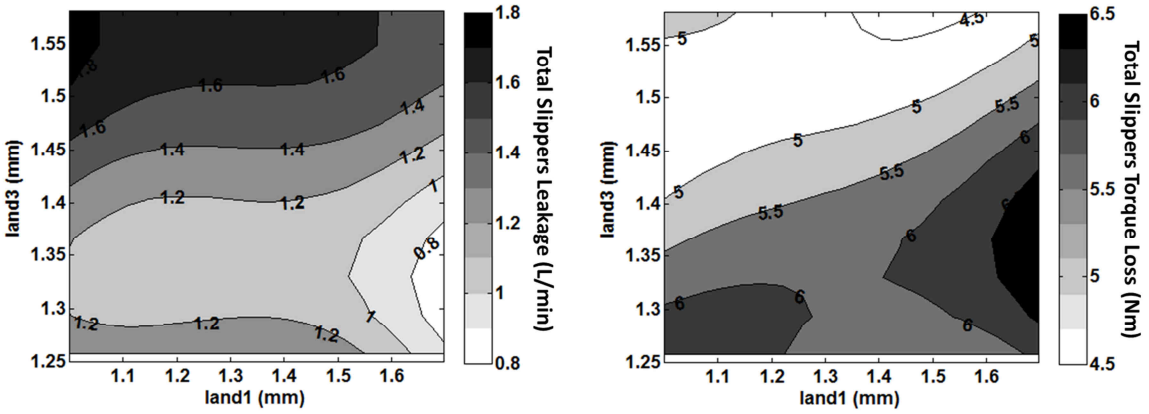

Figure 5.17. Total slippers leakage (left) and torque loss (right) as a function of inner and outer slipper land variation while maintaining a 98% hydrostatic balance ratio.

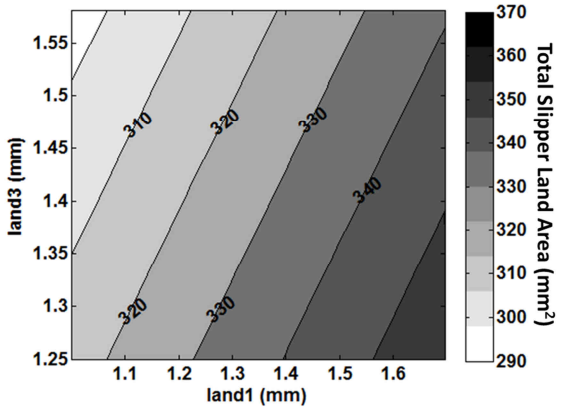

Figure 5.18. Total slipper land area as a function of inner and outer slipper land variation while maintaining a 98% hydrostatic balance ratio.

At this particular operating condition the decrease in torque loss has a larger impact on power loss than the increased losses from greater leakage flow rates, but the same is not true as the hydraulic working pressure increases. As the high pressure of hydraulic units continues to increase driven by the demand for higher power densities, the design advantage of the outer stabilizing land will decrease.

5.4 Original Contributions

These three case studies highlight the model based design potential enabled by computational power and the novel model developed in this work. Although experimental testing does not require modeling assumptions or approximations, it is notoriously expensive, measurements are limited, and reproducibility is not guaranteed. More frustrating is that when experimentally testing a pump, it is nearly impossible to observe the nature of the lubricating film and a designer is forced to intuitively reason why design changes caused different operation. With a numerical model, direct insight to design changes can be observed, allowing for a deeper understanding of the mechanisms impacting the operation.

Although the slipper lubrication numerical model is computationally expensive, a special purpose reduced order surrogate model was developed to allow for the rapid comparison of design changes, and the complex interactions between variables. This multi-modeling approach was integrated for the first time in lubrication analysis of the slipper – swashplate. Although the absolute value of surrogate modeling error increases near domain boundaries, overall trends are captured and promising subspaces can be refined with further simulations.

The multi-landed slipper case study utilized the blended modeling approach, with the physics based model driving a black-box surrogate modeling technique. Multi-parameter design variations were investigated using the reduced order model. In particular, it was discovered why from a design and efficiency standpoint slippers with an outer stabilizing land have a design advantage at lower working pressures and high speeds.

CHAPTER 6. CONCLUSIONS

For the first time, a numerical model of slipper-swashplate lubrication performance in axial piston machines has been developed which accounts for a wide range of physical phenomena including: slipper micro-motion, non-isothermal fluid film lubrication, the impact of slipper and swashplate deformation due to fluid pressures, and the impact of thermal effects from the slipper and swashplate solid bodies. The interactions between these non-linear problems have been solved using a novel coupling of numerical methods and computational algorithms.

The goal of the numerical model is to accurately predict lubrication performance between the slipper and swashplate. The desire to accomplish this was twofold: to discover the interaction of physical effects enabling lubrication and provide the foundation for model based design of new axial piston pumps. Yet no model is without limitations and boundaries. Numerically, tradeoffs between computational cost and convergence are necessary. Therefore, this model focused to:

- Predict fluid leakage from the slipper pocket.
- Predict viscous friction during full film lubrication.
- Predict areas and conditions under which mixed/boundary lubrication is likely to occur.

By concentrating on prediction of these three attributes, the lubrication performance of any slipper design under any set of environmental factors can be explored. In developing this model, numerous original contributions were necessary and in part include:

- In considering pressure deformation of both the slipper and swashplate, a fluid film pressure model capable of accounting for both top and bottom surface gradients in a cylindrical coordinate system was derived and implemented. Utilizing advancements in computational techniques and linear solvers, the fluid film spatial discretization increased resolution over 20 times compared to previous work.
- The dynamic pressure loading of the slipper and swashplate causes dynamic deformation effects. Modeling the resulting transient elastohydrodynamic deformation squeeze pressure and its impact was originally introduced in this work to significantly improve low film thickness lubrication performance predictions.
- Fixed clearance slipper hold down devices are common in commercially manufactured axial piston pumps, but were previously difficult to correctly model in part because of their high stiffness. Using an implicit micro-motion integration has overcome this obstacle as well as providing a more stabilized slipper micro motion prediction.
- Heating of the slipper and swashplate from numerous thermal sources was previously not considered, but this heating can have an impact on lubrication performance. A finite element thermal solver was implemented to consider temperature gradients inside the slipper and swashplate. The resulting surface

temperature and thermal deformation fields were coupled back into the lubrication model.

The principal unknown driving lubrication performance is the fluid film thickness between the slipper and swashplate. Experimentally this is difficult to observe due to high pressures, a fast moving lubrication domain, and the micro-scale height of lubricant. Nevertheless, an experimental test rig was built using miniature inductive sensors to directly measure the film thickness between the slipper and swashplate in a minimally modified axial piston pump. This experimental work validated the ability of the numerical model to predict the impact of design features on the wear and operation of a slipper design.

Three case studies were included to highlight the potential of the numerical model to drive investigations into the operational limits of a design, the impact of materials choices, and implementation of model based design. Interrogation of the complete fluid film and all corresponding physical attributes is possible using the model – something not possible even with the most sophisticated experimental techniques. Using a surrogate modeling technique a large design parameter perturbation was investigated to discover the limited advantageous use of a multi-landed slipper design.

This work has the potential to drive the development of tribological parings inside hydraulic machinery to a model based design approach. Hopefully with continued efforts both in academia and industry, this change can be realized and future hydraulic systems can become more clean, efficient, robust and inexpensive.

LIST OF REFERENCES

LIST OF REFERENCES

ANSYS. 2004. *ANSYS, Inc. Theory Reference*. ANSYS, Inc., Canonsburg, PA.

Bergada, J., Davies, D., Kumar, S., Watton, J. 2012. The effect of oil pressure and temperature on barrel film thickness and barrel dynamics of an axial piston pump. *Meccanica*, Vol. 47, pp. 639-654.

Bergada, J., **Kumar, S.**, **Davies, D.**, **Watton, J.** 2011. A complete analysis of axial piston pump leakage and output flow ripples. *Applied Mathematical Modeling*, doi:10.1016/j.apm.2011.09.016.

Bergada, J., **Watton, J.**, **Haynes, J.**, **Davies, D.** 2010. The hydrostatic/hydrodynamic behavior of an axial piston pump slipper with multiple lands. *Meccanica*, Vol. 45, pp. 585-602.

Beschorner, K., **Higgs, C.**, **Lovell, M.** 2009. Solution of Reynolds Equation in Polar Coordinates Applicable to Nonsymmetric Entrainment Velocities. *ASME J. Tribo.*, Vol. 131, No. 3.

Chang, L. 2000. A Simple and Accurate Method to Calculate Transient EHL Film Thickness in Machine Components Undergoing Operation Cycles. *Tribology Transactions,* Vol. 43, No. 1, pp. 116-122.

Canbulut, F., **Sinanoglu, C.**, **Koc, E.** 2009. Experimental analysis of frictional power loss of hydrostatic slipper bearings. *Industrial Lubrication and Tribology*, Vol. 61, No. 3, pp. 123-131.

Dahr, S. 2013. *A study of fluid structure and thermal interactions in the lubricating interface between gears and lateral bushes in external gear machines*. Ph.D. Thesis, Purdue University.

Dhar, S., Vacca, A., Lettini, A. 2013. A Novel Fluid-Structure-Thermal Interaction Model for the Analysis of the Lateral Lubricating Gap Flow in External Gear Machines. *Proc. ASME/Bath Symposium on Fluid Power and Motion Control, Sarasota, FL, Paper No. FPMC2013-4482.*

Deeken, M. and **Murrenhoff, H.** 2001. Advanced simulation of fluid power components using DSH*plus* and ADAMS. *Bath Workshop on Power transmission and Motion Control PTMC 2001*, Bath, UK, pp. 87-101.

Fang, Y., Shirakashi, M. 1995. Mixed lubrication characteristics between piston and cylinder in hydraulic piston pump-motor. ASME *J. Tribology,* Vol. 117, pp. 80-85.

Gockel, M. 1999. Technical application note: Inertia relief analysis using an automated support system. *MSC Software Support.*

Hamrock, B., Schmid, S., Jacobson, B.O. 2004. *Fundamentals of Fluid Film Lubrication.* Macmillan Publishing Company, New York.

Hooke, C. and **Kakoullis, Y.** 1979. On-line measurement of film thickness. *Proc. Conf. on Instruments and computers for cost effective fluid power testing*, C128/79, pp. 51-59.

Hooke, C. and **Kakoullis, Y.** 1981. The effects of centrifugal load and ball friction on the lubrication of slippers in axial piston pumps. *Proc. 6th Int. Fluid Power Symposium*, British Hydrodynamics Research Association, pp. 179-191.

Hooke, C. and **Kakoullis, Y.** 1983. The effects of non-flatness on the performance of slippers in axial piston pumps. *Proc. Instn. Mech. Engrs*, Vol. 197C, pp. 239-247.

Hooke, C. and **Li, K.** 1988. The lubrication of overclamped slippers in axial piston pumps-centrally loaded behavior. *Proc. Instn. Mech. Engrs*, Vol. 202, No. C4, pp. 287-293.

Hooke, C. and **Li, K.** 1989. The lubrication of slippers in axial piston pumps and motors-the effect of tilting couples. *Proc. Instn. Mech. Engrs*, Vol. 203, Part C, pp. 343-350.

Huang, C. and **Ivantysynova, M.** 2003. A new approach to predict the load carrying ability of the gap between valve plate and cylinder block. *Bath Workshop on Power transmission and Motion Control PTMC 2003*, Bath, UK, pp. 225 - 239.

Huang, C. 2006. An advanced gap flow model considering piston micro motion and elastohydrodynamic effect. *4th Fluid Power Net International PhD Symposium*, Sarasota, USA, pp.173-188.

Ivantysyn J. and **Ivantysynova M.** 2001. *Hydrostatic Pumps and Motors.* Academic Books International, New Delhi.

Ivantysynova M. and **Lasaar, R.** 2000. Ein Versuchsträger zur Messung der Reibkräfte zwischen Kolben und Zylinder in Axialkolbenmaschinen. *Konstruktion* Vol: 52 No: 6, pp. 57 - 65.

Kazama, T. 2005. Numerical simulation of a slipper model for water hydraulic pumps/motors in mixed lubrication. *Proc. 6th JFPS Int. Symp. on Fluid Power*, No. 2C4-5, pp. 509-514.

Kazama, T., **Yamaguchi, A.** 1993. Application of a mixed lubrication model for hydrostatic thrust bearings of hydraulic equipment. *ASME J. Tribology*, Vol. 115, pp. 686-691.

Kleist, A. 1997. Design of hydrostatic bearing and sealing gaps in hydraulic machines. *5th Scandinavian Int. Conf. on Fluid Power, Linkoping.*

Koc, E., **Hooke, C.**, **Li, K.** 1992. Slipper balance in axial piston pumps and motors. *ASME J. Tribology*, Vol. 114, pp. 766-772.

Koc, E., and **Hooke, C.** 1996. Investigation into the effects of orifice size, offset and overclamp ratio on the lubrication of slipper bearings. *Tribology International*, Vol. 29, No. 4, pp. 299-305.

Koc, E., and **Hooke, C.** 1997. Considerations in the design of partially hydrostatic slipper bearings. *Tribology International*, Vol. 30, No. 11, pp. 815-823.

Kumar, S., **Bergada, J.**, **Watton, J.** 2009. Axial piston pump grooved slipper analysis by CFD simulation of three-dimensional NVS equation in cylindrical coordinates. *Computers & Fluids*, Vol. 38, pp. 648-663.

Lasaar, R. 2003. *Eine Untersuchung zur mikro- und makrogeometrischen Gestaltung der Kolben-Zylinderbaugruppe von Schrägscheibenmaschinen*, VDI Fortschritt-Berichte. Reihe 1 No. 364. Düsseldorf: VDI. ISBN: 3-18-336401-8.

Li, S. and **Kahraman, A.** 2010. A Transient Mixed Elastohydrodynamic Lubrication Model for Spur Gear Pairs. *ASME J. Tribology*, Vol. 132, doi: 10.1115/1.4000270.

Liu, G. and **Quek, S.** 2003. *The Finite Element Method: A Practical Course*. Elsevier Butterworth-Heinemann, Burlington, MA..

Manring, N., **Johnson, R.**, **Cherukuri, H.** 2002. The impact of linear deformations on stationary hydrostatic thrust bearings. *ASME J. Tribology*, Vol. 124, pp. 874-877.

Manring, N., **Wray, C.**, **Dong, Z.** 2004. Experimental studies on the performance of slipper bearings within axial-piston pumps. *ASME J. Tribology*, Vol. 126, pp. 511-518.

Pang, Z., **Wenjie, Z.**, **Shun, J.** 1993. The study of hydrostatic lubrication of the slipper in a high-pressure plunger pump. *ASME J. Tribology*, Vol. 36, No. 2, pp. 316-320.

Patankar, S. 1980. *Numerical Heat Transfer and Fluid Flow.* Taylor & Francis. ISBN: 0-89116-522-3.

Pelosi, M. and **Ivantysynova, M.** 2008. A New Fluid-Structure Interaction Model for the Slipper-Swashplate Interface. *Proc. of the 5th FPNI PhD Symposium*, Cracow, Poland, pp. 219 - 236.

Pelosi, M. and **Ivantysynova, M.** 2009. A Novel Thermal Model for the Piston/Cylinder Interface of Piston Machines. *Bath ASME Symposium on Fluid Power and Motion Control (FPMC2009),* DSCC2009-2782.

Pelosi, M. and **Ivantysynova, M.** 2011a. The Influence of Pressure and Thermal Deformation on the Piston/Cylinder Interface Film Thickness. *Proc. 52nd Nat. Conf. on Fluid Power*, NCFP I11-9.3.

Pelosi, M. and **Ivantysynova, M.** 2011b. Surface Deformation Enables High Pressure Operation of Axial Piston Pumps. *ASME/Bath Symposium on Fluid Power and Motion Control*, Arlington, VI, USA.

Pelosi, M. 2012. *An Investigation on the Fluid-Structure Interaction of Piston/Cylinder Interface*. Ph.D. Thesis, Purdue University.

Pelosi, M. and **Ivantysynova, M.** 2012. Heat Transfer and Thermal Elastic Deformation Analysis on the Piston/Cylinder Interface of Axial Piston Machines. *Trans. ASME Journal of Tribology*, Vol. 134, October 2012, pp. 1-15.

Renard, Y. 2011. Gmm++ user documentation. *http://download.gna.org/getfem/html/homepage/gmm.html*, Release 4.1.1, April 2011.

Renius, K. 1974. *Investigations of the Friction Between Piston and Cylinder of Tilted Plate Axial Piston Machine,* VDI Forschungsheft 561. VDI Verlag Düsseldorf, Germany.

Reynolds, O. 1886. On the Theory of Lubrication and Its Application to Mr. Beauchamp Tower's Experiments, Including an Experimental Determination of the Viscosity of Olive Oil. *Philosophical Transactions of the Royal Society of London*, Vol. 177, pp. 157-234.

Roelands, C. 1966. *Correlational aspects of the Viscosity-Temperature-Pressure Relationship of Lubricating Oils*. Druk, V.R.B., Groningen, Netherlands.

Rokala, M., **Koskinen, K.**, **Calonius, O.**, **Pietola, M.** 2008. Tribological conditions between swashplate and slipper pad in variable displacement water hydraulic axial piston unit. *Proc. 6th Int. Fluid Power Conf.*, Dresden, Germany, Group E., pp. 301-312.

Schenk, A. and **Ivantysynova, M.** 2011. An investigation of the impact of elastohydrodynamic deformation on power loss in the slipper swashplate interface. *Proc. 8th JFPS Int. Symp. on Fluid Power*, No. 1C2-5.

Schenk, A., Ivantysynova, M. 2011b. Design an Optimization of the Slipper-Swashplate Interface Using an Advanced Fluid Structure Interaction Model. *Proc. 52nd National Conference on Fluid Power*, NCFP I11-4.2.

Spencer, N. 2014. *Design and development of a novel test method to measure the slipper / swashplate interface fluid film in a positive displacement machine.* Masters Thesis, Purdue University.

Shute, N. and **Turnbull, D.** 1962a. The minimum power loss of hydrostatic slipper bearings. *BHRA*, Report SP721, April.

Shute, N. and **Turnbull, D.** 1962b. The losses of hydrostatic slipper bearings under various operating conditions. *BHRA*, Report RR743, Oct.

Szeri, A. 2011. *Fluid Film Lubrication, Second Edition.* Cambridge University Press, New York.

Tang, B. 1993. Orthogonal Array-Based Latin Hypercubes. *Journal of the American Statistical Association*, Vol. 88, pp. 1392-1397.

Wieczorek, U. and **Ivantysynova, M.** 2002. Computer Aided Optimization of Bearing and Sealing Gaps in Hydrostatic Machines - The Simulation Tool CASPAR. *International Journal of Fluid Power*, Vol. 3, No.1, pp. 7-20.

Xiong, S., Lin, C., Wang, Y., Liu, W., Wang, Q.J. 2010. An Efficient Elastic Displacement Analysis Procedure for Simulating Transient Conformal-Contact Elastohydrodynamic Lubrication Systems. *ASME J. Tribology*, Vol. 132, doi: 10.1115/1.4001120.

Yabe, H., **Kubo, A.**, **Nakamura, T.**, **Togo, Y.** 1997. Fundamental characteristics of slipper bearings in swash plate type axial piston pumps and motors (2^{nd} report, performance of slipper bearing with Non-flat bearing surface). *Japan Society of Mech. Eng.*, pp. 319-324.

Zecchi, M. and **Ivantysynova, M.** 2011. A Novel Fluid Structure Interaction Model for the Cylinder Block/Valve Plate Interface of Axial Piston Machines. *Proc. 52nd Nat. Conf. on Fluid Power*, NCFP I11-9.2.

Zecchi, M. and **Ivantysynova, M.** 2012. A novel approach to predict the cylinder block / valve plate interface performance in swash plate type axial piston machines. *Proc. Bath/ASME Symposium on Fluid Power and Motion Control*, Bath, UK, pp. 505-517.

Zecchi, M. 2013. *A novel fluid structure interaction and thermal model to predict the cylinder block/valve plate interface performance in swash plate type axial piston machines.* Ph.D. Thesis, Purdue University.

Zienkiewica, O., **Taylor, R.**, **Zhu, J.** 2005. *The finite element method: Its basis and Fundamentals*. Elsevier Butterworth-Heinemann, Burlington, MA.

VITA

VITA

Andrew attended Kettering University in Flint, MI for his BSME and graduated in June, 2009. While enrolled at Kettering, he was employed as a co-op engineer at Cosma Engineering with a focus on CAE analysis of automotive body structures. His undergraduate thesis is entitled “Development of a surrogate model to rapidly create baseline automotive bumper designs based on simple input criteria.” In July 2009, Andrew began his graduate research at the Maha Fluid Power Research Center at Purdue University in the School of Mechanical Engineering under the advisement of Dr. Monika Ivantysynova. His research focused on the numerical modeling of lubrication and tribology within swashplate type axial piston hydraulic pumps and motors. During his tenure at Purdue he was a two year recipient of the Laura Winkelman Davidson Fellowship, won the 2011 International Japan Fluid Power Symposium best paper award, was awarded the prestigious Backe Medal during the 2012 FPNI Fluid Power PhD Symposium, and received the 2013 Outstanding SURF mentor of the Summer award from Purdue University. Andrew was a member of the NSF funded Center of Compact and Efficient Fluid Power Engineering Research Center, and served two years as president of the Student Leadership Council. In August 2012 Andrew received his MSME and then in December, 2014 his Ph.D. from Purdue University.